GEOMETRY DEPENDENCE OF TEM TURBULENCE IN THE HSX STELLARATOR AND COMPARISON TO NONLINEAR GYROKINETIC SIMULATION

by

Jason C. Smoniewski

A dissertation submitted in partial fulfillment of the requirements for the degree of

Doctor of Philosophy

(Electrical Engineering)

at the

UNIVERSITY OF WISCONSIN-MADISON

2021

Date of final oral examination: April 29, 2021

The dissertation is approved by the following members of the Final Oral Committee:

David T. Anderson, Professor, Electrical and Computer Engineering

Joseph N. Talmadge, Senior Scientist, Electrical and Computer Engineering

Chris C. Hegna, Professor, Engineering Physics

Paul W. Terry, Professor, Physics

Amy E. Wendt, Professor, Electrical and Computer Engineering

Moritz J. Pueschel, Group Leader, Eindhoven University of Technology

ABSTRACT

Turbulent transport is responsible for much of the energy and particle losses in present-day fusion plasma experiments, and optimization to reduce turbulence will be a major step towards realizing the benefits of fusion energy. Stellarators, with the flexibility afforded by external coils and three-dimensional geometry, may be able to reduce turbulence through careful shaping of the magnetic field. Such optimization relies on the ability of simulations to accurately predict turbulence in real devices, and validation studies are severely lacking for the stellarator.

In this dissertation, the magnetic flexibility of the Helically Symmetric eXperiment (HSX) stellarator is exploited to investigate Trapped Electron Mode (TEM) turbulence in quasi-helically symmetric and degraded-symmetry configurations through experimental measurements and gyrokinetic simulation. This work includes the first comparison of nonlinear simulations in the Quasi-Helically Symmetric (QHS) and Mirror configurations, as well as the first comparison of nonlinear simulations at experimental parameters to experimental measurements. A database of archived HSX plasma discharges has enabled the temperature and density profiles to be matched in QHS and Mirror, showing that thermal transport is larger in the Mirror configuration at the mid-radius. Simulations do not reproduce this difference between geometries, but transport is sensitive to whether turbulence is in a ∇n -driven or $\nabla T_{\rm e}$ -driven regime. More precise gradient measurements would be required for full validation of this geometry dependence.

While linear growth rates are not predictive of overall turbulence, general aspects of experimental transport are captured by nonlinear simulations. In both simulation and experiment, the heat flux and density fluctuation amplitude increase more strongly with the density gradient than the temperature gradient, and the simulated heat flux matches measurements within experimental uncertainties for both configurations. This confirms that ∇n -driven TEM turbulence is the dominant driver of anomalous transport in HSX.

Zonal flows can be important to TEM turbulence saturation, and are present in all non-linear simulations of HSX. This work includes the first calculation of the linear collisionless zonal flow damping in quasi-symmetric magnetic geometry. Flux-tube, flux-surface, and full-volume calculations of the zonal flow evolution and residual are compared in the QHS and Mirror configurations, as well as the quasi-axial symmetry of the National Compact Stellarator eXperiment (NCSX). Despite quasi-symmetry, the dynamics of the zonal flow in all three configurations are similar to those in a conventional stellarator. The zonal flow oscillation presents another opportunity for comparison between simulation and experiment, but measurement of the zonal flow is left to future work. This dissertation is only the starting point for a validation study on the HSX stellarator. Significant opportunities exist for updated experimental measurements and a deeper investigation into the nonlinear physics responsible for TEM dynamics.

For Konrad, who reminded me why I started this, and for Alice, who gave me the strength to finish it.

ACKNOWLEDGMENTS

I have relied on a great many people during my time at HSX, and I would not have finished this dissertation without them. I would like to thank David Anderson, Joe Talmadge, and M.J. Pueschel, who have served as my ever-patient advisors during this research. Their tenacious yet nonjudgmental questioning has made me grow as a scientist. In addition, I would like to thank Chris Hegna, Paul Terry, and Amy Wendt for serving on my committee.

I am indebted to those who have contributed directly to the research presented in this dissertation. Gavin Weir provided an incredible experience by inviting me to join experiments at Wendelstein 7-X, and has openly shared his hard work collecting HSX profiles, thus making experimental gradient scans possible. Ben Faber has provided this same support and openness on the simulation side of this work. I would especially like to thank Ben for helping me to find my feet after a particularly disheartening APS meeting, and starting my journey into gyrokinetic simulation. Konstantin Likin provided the reflectometry diagnostic and data for this work, and I appreciate our many discussions as I worked through the fluctuation analysis. I enjoyed collaborating with Edi Sáncez and Ivan Calvo on the zonal flow paper, and their contributions were fundamental to understanding the HSX zonal flow calculations.

I am grateful to all the scientists and students that have contributed to the history of HSX represented in the data archive. Operations would not be possible without the whole team, and I have had many valuable conversations with Simon Anderson, Chuanbao Deng, and Santhosh Kumar while in the control room. Special thanks go to Aaron Bader and Laurie Stephey for persistent attempts to keep me focused on graduating, and to Paul Willis for his quick resolution of many technical issues. I would also like to thank John Schmitt for particularly insightful discussions on the analysis of HSX data. As a new student, Alexis Briesemeister, Chris Clark, and Bob Wilcox provided advice that has guided me through multiple projects at HSX, even if I may not have listened to it at first. Jerahmie Radder

encouraged me to start using Linux, and I have never looked back. And thanks to Evan Schilling for his work with Guassian process regression, and to Ian Mckinney for executing additional nonlinear simulations.

The other graduate students and camaraderie at HSX have made the problems manageable and provided the daily motivation to keep working. I have never learned so much physics as quickly as I did in the HSX basement offices, and I remember many good nights at The Library or the Terrace where problems were dissected and pressure was released. This community has influenced my time at HSX more than any other, and always for the better. In particular, thank you to Enrico Chlechowitz and Fernando Castillo for keeping the HSX spirit alive and always attending to the needs of the group. Thank you to the newer students, who have rebuilt that camaraderie and mutual support, and have brought so much new energy to the lab.

I am especially grateful to Paul Terry for allowing me to join his research group meetings, even though I was more of an experimentalist than a theorist. Thanks to Adrian Fraser, Zach Williams, Garth Whelan, and Justin Walker, who enthusiastically welcomed me to the study of turbulence.

I have benefited from collaborations with a number of outside researchers. I would like to thank Shinsuke Satake and Matt Landreman for patiently guiding my first steps into high-performance computing with FORTEC-3D and SFINCS. I deeply appreciate the time spent by Thomas Windisch and Carsten Lechte to explain the interpretation of reflectometry measurements to me.

I would also like to thank my undergraduate advisor, Matt Stoneking. He introduced me to plasma physics, guided me through the first few years in the field, and has continued to provide counsel. I am incredibly lucky to have such an excellent mentor.

Thank you to all my family and friends, who never stopped cheering for me as "a few years" turned into "a few *more* years." Thank you to my parents, Stan and Cecilia, who

took every opportunity to encourage the little boy who wanted to grow up to be a scientist. Their support has been unwavering, whether it was trips to the museum, shooting off rockets, boiling chicken hearts, or hosting twenty plasma physicists at their house. Thank you to my sister, Clara, and her partner, Kleighton, for reminding me how much world exists outside the lab, and for their enthusiasm for discovery no matter how trivial and specialized. Thank you to my parents-in-law, Steve and Marti, who have helped me to relax and enjoy the present. Thank you to Melanie Kathan, Sam Punzel, and Natalia Zborka, who have listened to endless frustration, but are always available with an open ear and ready diversion. And thank you to my grandfather, who was primed with a question and hope for the future every time we talked. My friends and family make me believe that my work matters, and I will always wish for more time in their company.

Most of all, thank you to my wife, Alice, who has never let me quit, never let me stop talking, living, and growing. She reminded me to keep dreaming even while I made our lives more difficult, and carried more than her fair share of the burden while I studied. Completion of this work is a testament to her love and support, and the limits of her patience. Finally, thank you to my son, Konrad. I thought that a baby would make graduation more difficult. Instead, holding him makes the worry fade away, and he has restored to me a sense of wonder. If this dissertation suffered for lack of sleep, it was a most worthwhile exchange.

CONTENTS

Abstract						
Li	List of Tables ix					
List of Figures x						
1	Intr	oduction	1			
	1.1	Turbulent transport and validation	3			
	1.2	The Helically Symmetric eXperiment (HSX)				
	1.3	Dissertation Overview	16			
2	Exp	erimental measurements in HSX	26			
	2.1	An HSX profile database	27			
	2.2	Electron energy transport	34			
	2.3	Density fluctuation measurements from reflectometry	43			
	2.4	Chapter Summary	49			
3	Gyr	okinetic simulation of TEM turbulence in HSX	54			
	3.1	Gyrokinetic simulation with Gene	55			
	3.2	Comparison of the QHS and Mirror configurations	59			
	3.3	Temperature effects on TEM simulations in HSX				
	3.4	TEM simulations at experimental gradients	68			
	3.5	Comparison to experimental measurements	79			
	3.6	Chapter Summary	83			
4	Zon	al flow collisionless damping and the residual in HSX	87			
	4.1	Collisionless zonal flow damping	89			
	4.2	Comparison of local and global calculations				
	4.3	Zonal flow response in different flux tubes	105			
	4.4	Comparison of configurations: QHS, Mirror, and NCSX				
	4.5	Chapter Summary				
5	Con	clusions and Suggestions for Future Investigations	123			
	5.1	Suggestions for Future Investigations	126			

		viii
A	Proxy values for TEM transport in HSX	136
В	The HSX profile database	137

LIST OF TABLES

5.1	Summary of comparison between experiment and simulation	. 125
A.1	Proxy values for TEM configurations from J.H.E. Proll	. 136

LIST OF FIGURES

1.1	Toroidal coordinates	2
1.2	A flux surface and field line in the QHS configuration	11
1.3	Comparison of $ B $ and κ_n in QHS and Mirror	14
2.1	GPR and linear fit of QHS and Mirror profiles with the same ECRH absorbed	
	power	29
2.2	Distribution of gradients in HSX profile database	31
2.3	GPR and linear fits of matched QHS and Mirror profiles	32
2.4	ECRH deposition $P(\rho)$ and absorbed power $\int P(\rho)V'd\rho$	35
2.5	Comparison of a geometric estimate of $V'\langle \nabla \rho \rangle$ to field-line following $\ \ldots \ \ldots$	37
2.6	Heat flux for profiles in Figures 2.1 and 2.3, compared to neoclassical calculations	38
2.7	Thermal diffusivity for profiles in Figures 2.1 and 2.3, compared to neoclassical	
	calculations	39
2.8	Scaling of heat flux and diffusivity with a/L_n	41
2.9	Scaling of heat flux and diffusivity with a/L_{Te}	42
2.10	Schematic of the HSX reflectometer	43
2.11	Reflectometer measurement phase and amplitude distribution	46
2.12	Scaling of \tilde{n}/n with a/L_n and a/L_{Te}	48
2.13	Scaling of \tilde{n}/n with $n_{\rm e}$	49
3.1	Representation of a flux tube in QHS geometry	56
3.2	Comparison of $ B $ and κ_n at $r/a=0.5$ and $0.7\ldots\ldots\ldots\ldots$	57
3.3	Growth rates for $a/L_{Te}=0$, $T_{\rm i}/T_{\rm e}=1$, and changing a/L_n	60
3.4	Heat and particle fluxes for $a/L_{T\rm e}=0$, $T_{\rm i}/T_{\rm e}=1$, and changing a/L_n	61
3.5	Growth rates for changing $a/L_{T\mathrm{e}}$ and $T_{\mathrm{i}}/T_{\mathrm{e}}$	63
3.6	Heat and particle fluxes for $a/L_{T\rm e}=2$, $a/L_n=2$, and changing $T_{\rm i}/T_{\rm e}$	64
3.7	Eigenspectrum of modes with $a/L_n=2$, $a/L_{T\rm e}=2$, and changing $T_{\rm i}/T_{\rm e}$	65
3.8	Frequencies from nonlinear simulation with $a/L_n = 2$, $a/L_{Te} = 2$,	
	and changing $T_{ m i}/T_{ m e}$	66
3.9	Growth rates contours for $T_{\rm i}/T_{\rm e}=1$ and scanning a/L_n and $a/L_{T\rm e}$	67
3.10	Growth rates contours for $T_{ m i}/T_{ m e}=0.2$ and scanning a/L_n and $a/L_{T m e}$	68
3.11	Growth rates for $a/L_{Te}=2$, $T_{\rm i}/T_{\rm e}=0.2$, and changing a/L_n	69
3.12	Eigenspectrum of modes with $a/L_{Te}=2$, $T_{i}/T_{e}=0.2$, and changing a/L_{n}	70

3.13	Heat and particle fluxes for $a/L_{Te}=2$, $T_{\rm i}/T_{\rm e}=0.2$, and changing a/L_n 71
3.14	Growth rates for $a/L_n=2$, $T_{\rm i}/T_{\rm e}=0.2$, and changing $a/L_{T{\rm e}}$
3.15	Eigenspectrum of modes with $a/L_n=2$, $T_{\rm i}/T_{\rm e}=0.2$, and changing $a/L_{T{\rm e}}$ 72
3.16	Heat and particle fluxes for $a/L_n=2$, $T_{\rm i}/T_{\rm e}=0.2$, and changing $a/L_{\rm Te}$ 73
3.17	Heat flux spectra with $a/L_{Te}=2$, $T_{\rm i}/T_{\rm e}=0.2$, and changing a/L_n
3.18	Heat flux spectra with $a/L_n=2$, $T_{\rm i}/T_{\rm e}=0.2$, and changing $a/L_{T{\rm e}}$
3.19	Frequencies from nonlinear simulation with $a/L_{T\rm e}=2$, $T_{\rm i}/T_{\rm e}=0.2$,
	and changing a/L_n
3.20	Frequencies from nonlinear simulation with $a/L_n=2$, $T_{\rm i}/T_{\rm e}=0.2$,
	and changing $a/L_{T\mathrm{e}}$
3.21	Comparison of the heat flux from simulation to experimental measurements $$ 80
3.22	Comparison of density fluctuation amplitude scaling with a/L_n between
	reflectometry measurements and simulation
4.1	A flux surface and field line in NCSX
4.2	Comparison of $ B $ in different flux tubes in HSX and NCSX
4.3	Rotational transform profile in HSX and NCSX
4.4	Zonal flow residual in NCSX for local and global calculations
4.5	Zonal flow time evolution in NCSX for flux-surface and flux-tube calculations $$. 102
4.6	Zonal flow time evolution in NCSX for full-volume and flux-tube calculations $$. $$ 103
4.7	Zonal flow time evolution in Mirror for full-volume and flux-tube calculations . 104
4.8	Convergence of zonal flow with $n_{ m pol}$ in Mirror
4.9	Convergence of zonal flow with $n_{\rm pol}$ in NCSX at $s=0.54$
4.10	Non-convergence of zonal flow with n_{pol} in NCSX at $s=0.63$
4.11	Zonal flow evolution in two QHS flux tubes with $n_{\rm pol}=1$ and 4 108
4.12	Zonal flow residual for QHS in flux tubes with $n_{\rm pol}=1$ and $4\ldots\ldots\ldots$ 109
4.13	Zonal flow evolution in different NCSX flux tubes
4.14	Zonal flow residual from different flux tubes in NCSX
	Zonal flow evolution in the QHS and Mirror configurations
	Zonal flow residual in QHS and Mirror for local and global calculations 113
4.17	Short time zonal flow evolution in QHS and Mirror
5.1	Diagram of the validation process

Introduction

Nuclear fusion research strives to provide a clean and abundant source of energy. When light nuclei are confined at a very high temperature and density, the nuclei fuse and a small amount of mass is converted into energy according to the well-known equation $E=mc^2$. At the high temperatures required for fusion, matter is necessarily in the plasma state, where atoms are ionized and the resulting fluid of ions and electrons demonstrates collective behavior and reacts to electric and magnetic fields. Throughout human history, an exothermic fusion reaction has been demonstrated in our sky, producing the light of our sun. For better or worse, humans unlocked a fusion reaction on Earth to create the most destructive weapons ever seen. However, the peaceful applications of fusion have lagged behind due to the difficulty of sustaining a confined burning fusion plasma.

In order to produce more energy than is needed to create the plasma, energy must be confined for a long enough time to sustain the fusion reaction. The figure of merit for fusion energy is the triple product $nT\tau_E$, where n is the plasma density, T is the temperature, and τ_E is the energy confinement time. In the sun, confinement is provided by the self-gravitation of such a massive body. Inertial confinement depends on compressing a fuel to extremely high density and temperature, while the reaction products are allowed to escape and τ_E is small. In magnetic confinement, a magnetic bottle is used to confine the plasma and τ_E is typically large.

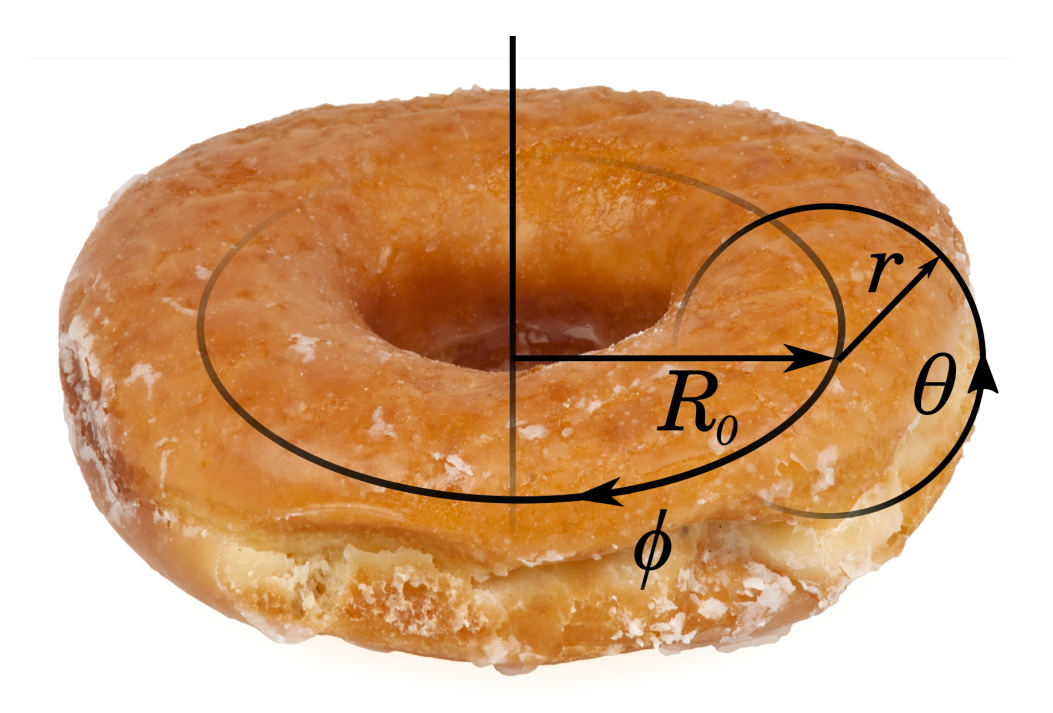


Figure 1.1: Illustration of toroidal coordinates, where R is the major radius, r is the minor radius, θ is the poloidal direction, and ϕ is the toroidal direction.

The two leading magnetic confinement concepts are the tokamak and the stellarator, both of which are toroidal, or doughnut-shaped, devices. Naturally, toroidal coordinates are used to describe phenomena in such devices, and are illustrated in Figure 1.1. These devices require both a toroidal and poloidal magnetic field to provide the magnetic bottle to confine the plasma. In a tokamak, a number of planar coils generate a toroidal magnetic field, and current is driven in the plasma itself to generate a poloidal magnetic field. A stellarator uses external coils to generate both the toroidal and poloidal magnetic fields, and does not require current driven within the plasma. However, in both tokamaks and stellarators, particles and energy continue to leak out of the magnetic bottle, reducing $nT\tau_E$. A major area of fusion research, including this dissertation, aims to understand and mitigate any leaks.

1.1 Turbulent transport and validation

Turbulence is a ubiquitous transport mechanism for particles and energy to leave the plasma. In a turbulent system, fluctuations are excited across a broad range of spatial scales. These fluctuations exchange energy, leading to a complex nonlinear system characterized by randomness and irreversibility. In a magnetically-confined plasma, gradients of the plasma temperature or density can drive a self-reinforcing instability. This instability grows until reaching saturation, the point at which the free energy available to the mode is equal to the energy transfer to other modes. As other modes grow, they affect the efficiency of this energy transfer, as well as transfer energy to still other modes. The resulting spectrum of interacting modes is turbulence, and such modes are responsible for the majority of particle and energy transport in modern fusion devices. Controlling turbulent transport would greatly improve plasma confinement, bringing fusion energy closer to realization. This dissertation further develops the understanding of turbulent transport in the three-dimensional geometry of a stellarator.

Optimization of turbulent transport

In a stellarator, where the magnetic field is generated by external coils, the magnetic field is necessarily three-dimensional, whereas the magnetic field in a tokamak is axisymmetric. This relaxation of axisymmetry gives stellarator plasmas many more degrees of freedom. In addition, because a stellarator does not rely on a plasma current for the confining magnetic field, designers have more control to impose choices on the plasma geometry. The advent of powerful computers and numerical tools has lead to the development of optimized stellarators, where the plasma boundary of a target geometry, defined by a Fourier expansion of 50 or more coefficients, is modified in order to meet specific physics goals. Neoclassical transport, or the modification of classical collisional transport due to a toroidal magnetic

field, is large in a conventional stellarator at low collisionality, and was a significant disadvantage for the development of a stellarator fusion reactor. Optimization to reduce neoclassical transport has been successfully demonstrated in Wendelstein 7-AS¹ and HSX.² With the reduction of neoclassical transport, turbulence is the dominant source of energy and particle transport throughout most of the device.³ Just as neoclassical transport can be minimized by geometry optimization, a similar strategy can target turbulent transport.⁴ Given the interaction of a large number of fluctuations across many scales, a nonlinear simulation to solve for transport uses a large amount of computational time and resources. This is unfeasible in an optimization loop, and success instead depends on the selection of a good proxy for turbulence. Efforts are underway to design such proxies⁵⁻⁷ and verify that simulations confirm reduced transport regimes identified by these proxies.^{8,9} While these studies confirm that a linear proxy can predict the turbulent transport in nonlinear simulation, at least under certain conditions, the question of whether nonlinear simulations predict the turbulent transport in real experiments is still unanswered.

These optimization tools and turbulence simulations are only useful to the design of next generation devices if they accurately model real turbulence. The process of testing a code is conceptually broken into two parts; verification and validation. Verification considers whether a given code correctly solves the underlying numerical model. Validation compares a code and underlying model to experimental results to determine whether they are adequate to represent the relevant physics. ^{10–12} By attempting to reproduce turbulence in existing experiments, validation increases confidence in the predictive ability of simulation, or identifies deficiencies for additional study. Currently, most plasma micro-turbulence simulations take advantage of the gyrokinetic formalism, where the dimensionality of the computational problem is reduced by averaging over the fast gyromotion of a particle around a field line. ¹³ The present work describes progress towards validation of such gyrokinetic simulations in an optimized stellarator.

Present status of the validation of gyrokinetic simulations

While optimization focuses on heat and particle fluxes driven by turbulence, numerical results give access to many other observables, such as density, temperature, and potential fluctuation amplitudes and frequencies, cross phases, or spectra of those quantities. Validation of a code entails comparing one or more of these numerical outputs with measurements from an experimental diagnostic to determine if the model accurately describes the real turbulence. 10–12 This process is complicated by the fact that any experimental measurement requires interpretation, which may involve statistics, analytic models, or extensive simulations of their own. Turbulence simulations are also sensitive to input parameters such as driving gradients, and the sensitivity of any given measurement should be included when assessing whether a model and experiment agree. Sensitive measurements can more easily identify differences between different models, but the larger disagreement between model and experiment must be addressed within the context of measurement uncertainties. Validation metrics can be defined to more clearly illustrate agreement or disagreement while accounting for this sensitivity, ¹⁴ but the assumptions that go into a single measurement can still provide misleading agreement. Well-designed studies measure two or more quantities to reduce this likelihood and further constrain matching simulations.

Validation in tokamaks

Comparisons of gyrokinetic simulations to experiment have been performed across a range of measurements in tokamaks. While validation targets necessarily depend on the diagnostic capabilities of a device, heat fluxes and density fluctuations feature strongly across the literature. These quantities are the most easily accessible, and the first validation studies on DIII-D compared gyrokinetic calculations to measurements of density fluctuations and the heat flux from experimental profiles. Density fluctuation correlation lengths measured by beam emission spectroscopy were in good agreement with simulations only

when the effect of the zonal flow was included. ¹⁵ While reduced-geometry simulations showed that the density fluctuation amplitude and heat flux were significantly larger in simulations than in experiment, ¹⁶ full-volume simulations did capture the experimental heat flux within uncertainties, ¹⁷ suggesting that fluctuations can couple between flux surfaces. Later studies on DIII-D added temperature fluctuations from a correlation electron cyclotron emission diagnostic ¹⁸ and density fluctuations from Doppler reflectometry ¹⁹ to the comparison, and found that density and temperature fluctuations, and heat and particle fluxes, could not all be matched simultaneously. This has motivated further development of the gyrokinetic simulations and synthetic diagnostics involved. Measurements of both density and temperature fluctuations offer the chance to measure the cross phase between fluctuations, as was done at DIII-D²⁰ and ASDEX Upgrade. ²¹ These studies found that the cross phase is a sensitive indicator of driving instability, even while the heat flux or fluctuation amplitude may differ significantly. This allows comparison to be made to the mode underlying turbulence, even while not reproducing an experimental discharge in every detail.

Given the large uncertainty in experimental measurements of temperature and density gradients, precise matching to an experimental discharge requires varying input parameters within their experimental uncertainties. This is referred to as "flux-matching", and finds that the scanning gradients in simulation within experimental gradient uncertainties can account for the anomalous flux measured in ASDEX Upgrade, ²² DIII-D, ²³ JET, ²⁴ and MAST. ²⁵ While flux-matching can likely determine that turbulence is responsible for transport, in most cases this obscures the sensitive differences between gyrokinetic codes or models. However, flux-matched simulations increase the confidence for a comparison of other sensitive turbulence measurements. Gyrokinetic simulations generally take advantage of the separation of scales between electron-scale and ion-scale turbulence to simulate a narrower range of wavenumbers and save on computational cost. However,

simulations simultaneously spanning ion and electron scales can be needed to account for the experimental heat flux in some situations. ^{26–28}

In the Tore-Supra tokamak, researchers have been able to simultaneously match heat diffusivity and reflectometry measurements with gyrokinetic simulation.²⁹ However, details of the density fluctuation spectra showed that instrumental effects are important in the comparison to simulation. Synthetic diagnostics apply an instrumental function to the underlying simulated fluctuations to try to reproduce a measurement as made by the actual diagnostic. Such synthetic diagnostics are required to identify coherent peaks in the frequency spectra of density fluctuations as a signature of TEM turbulence. 30-32 Reflectometry measurements are based on the backscattering of a microwave from the cutoff layer of a plasma, and are susceptible to significant deviation in reflection or refraction. Synthetic diagnostics for the purpose of interpreting reflectometry are specific to the machine and diagnostic system being modeled. These synthetic diagnostics range in complexity from a volume-averaged intensity to incorporating full-wave electromagnetic codes. 33 Comparison for the FT-2 tokamak found agreement in the Doppler shift and the width of the frequency spectrum.³⁴ A particularly thorough investigation of turbulence through the lens of reflectometry was completed by ASDEX Upgrade, TCV, and Tore-Supra, 35 including fluctuation power spectra, radial profiles of fluctuation amplitude and propagation velocity, and the measurement of geodesic acoustic modes. By surveying many measurements, it was possible to identify where simulations do not reproduce the experiment, and also where synthetic diagnostics do not reproduce the instrument function of the corresponding diagnostics. The shape of the wavenumber spectra is strongly modified by the synthetic diagnostic, flattening spectra when fluctuations are large and changing the relative amplitude of measured low-wavenumber and high-wavenumber turbulence. 36,37 While simulated fluctuations generally require a synthetic diagnostic to compare to experimental measurements, there is a linear relation between the scattered

power in reflectometry and density fluctuations at small fluctuation amplitudes.³⁸

Validation in tokamaks remains an active area of research as gyrokinetic simulations continue to extend the included physics and new and more precise measurements are available to compare to simulation. These studies must take into account the capabilities of the simulation, be it a limited computational domain or sensitivity to driving gradients, as well as the limited measurement of turbulence afforded by a real diagnostic. Nevertheless, efforts have produced very close comparisons between simulated and measured turbulence, indicating that gyrokinetic simulations are an appropriate framework for studies of plasma micro-turbulence.

Validation in stellarators

Gyrokinetics in three-dimensional geometry is more numerically expensive than in tokamak geometries, and synthetic analogues to experimental measurements are not straightforward. For a tokamak, and axisymmetry allows a reduced geometry computational domain to represent any location on the flux surface; however, a stellarator may require careful planning to simulate turbulence in the line-of-sight of a diagnostic. For this reason, comparisons between simulation and measurement on stellarators have only recently included a quantitative dimension. Studies at the Large Helical Device (LHD) have found that the inward-shifted configuration reduces neoclassical transport, but also significantly affects anomalous transport. Density fluctuation profiles measured by phase contrast imaging were found to peak in the same locations as peak linear growth rates for the TEM and ITG. ³⁹ Nonlinear gyrokinetic simulations of ITG turbulence with adiabatic electrons agreed with the experimental ion heat flux within 30% of measurements, and a the density fluctuation wavenumber spectrum was consistent with phase contrast imaging measurements. ⁴⁰ In addition, it was found that potential fluctuations shift to high-wavenumber regions where linear growth rates are more stable in the inward-shifted configuration, providing a

reduction in turbulent transport. Simulations of ITG turbulence in these inward-shifted configurations find quantitative agreement with the experimental heat flux, and show that the zonal flow is responsible for the transfer of energy to higher wavenumbers. ⁴¹ Nonlinear studies including kinetic electrons find good agreement with the electron energy flux, but significantly underpredict the ion heat flux. ⁴² In a study combining results from both LHD and Heliotron-J, simulations reproduced a reduction of turbulent transport in the inward-shifted configuration and determined that it was due to the relative strength of zonal flows. ⁴³ Flux-matched simulations have demonstrated the ion heat flux is very sensitive to the ion temperature gradient, and this sensitivity must be taken into account for comparison to the experiment. ⁴⁴ The understanding of turbulence regimes and interaction with the zonal flow have produced reduced models of ITG transport in LHD that are compatible with experimental profiles. ⁴⁵

The TJ-II team has invested considerable effort in the use of Doppler reflectometry for density fluctuation measurements, and has measured wavenumber spectra and correlation lengths. ⁴⁶ This work has provided the basis for a comparison of density fluctuations from Doppler reflectometry to linear instability calculations with Euterpe. ⁴⁷ Measurements found that fluctuations are localized on a flux surface in agreement with gyrokinetic simulation. However, this localization depends on the rotational transform, and this dependence was not the same in simulation and experiment. The TJ-II team has also measured zonal flow oscillations, ^{48,49} potentially allowing a new point of comparison between simulation and experiment that is unique to three dimensional devices. Recently, heavy-ion beam probes have been used to make two-dimensional maps of fluctuations for future validation studies that could investigate the validity of local approximations in three-dimensional systems. ⁵⁰

The Wendelstein 7-X (W7-X) stellarator is a nearly quasi-isodynamic stellarator, and thus is nearly stable to the TEM.⁵ The first flux-surface calculations in stellarator geometry

showed that the ITG is localized to a narrow band in the bad-curvature region of W7-X⁸, and could be stabilized by a poloidal shift of fluctuations to less-bad curvature due to the radial electric field. Consequently, studies have attempted to compare turbulence when the TEM or ITG drives transport. ⁵¹ A comparison between simulation and experimental heat flux shows that there is a transition from a higher-flux ITG-dominated state to a lower-flux TEM-dominated state when the electron density is strongly peaked. ⁵² However, simulations have not been matched to experimental parameters in a validation effort.

1.2 The Helically Symmetric eXperiment (HSX)

The Helically Symmetric eXperiment (HSX)⁵³ is a stellarator designed to demonstrate the feasibility and benefits of Quasi-Helical Symmetry (QHS) in a device optimized to reduce neoclassical transport. A quasi-symmetric stellarator has a symmetry in the magnitude of the magnetic field |B|, but not necessarily a symmetry in the vector \vec{B} . The magnitude of the magnetic field along a field line can be represented by a Fourier expansion as

$$B/B_0 = 1 + \sum b_{nm} \cos(n\phi - m\theta) . \tag{1.1}$$

Here, n and m are the toroidal and poloidal mode numbers, and ϕ and θ are the toroidal and poloidal coordinates, respectively. In a large-aspect-ratio tokamak, n=0 due to axisymmetry and m=1 due to the 1/R dependence of a toroidal magnetic field, where R is the major radius. The pitch of the field line is described by $t=\Delta\theta/\Delta\phi$, and the magnetic field is written as

$$B/B_0 \approx 1 - \epsilon_t \cos(\iota \phi)$$
, (1.2)

where $b_{01}=-\epsilon_t$. The field in a conventional stellarator may be described by a large number of contributing (n,m) modes, leading to large direct-loss orbits of trapped particles. The magnetic spectrum in a quasi-symmetric stellarator is dominated by a single mode b_{nm} , causing the collisionless bounce-averaged drift of trapped particles from a flux surface to go

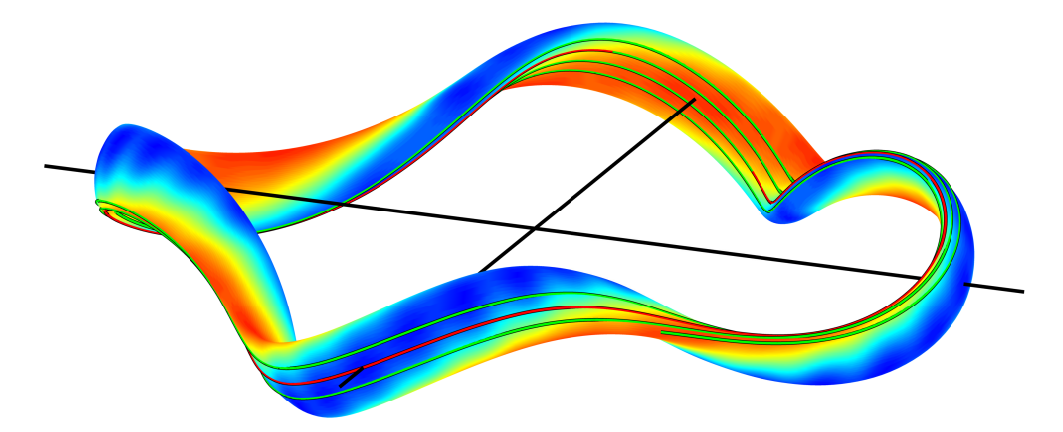


Figure 1.2: A flux surface and field line for the QHS configuration of HSX. Colors correspond to |B|, where blue is the minimum field strength. A field line followed for one poloidal turn is shown in red, and one extended to four poloidal turns is in green.

to zero and reducing neoclassical transport and flow damping. Different quasi-symmetries are defined by the choice of dominant mode in the magnetic spectrum. Quasi-polidal symmetry has a dominant m=0 mode, while quasi-axial symmetry has a dominant n=0 mode, similar to a tokamak. Quasi-helical symmetry uses a single $n\neq 0$, $m\neq 0$ mode, creating the helical shape of the |B| contours, as seen in Figure 1.2. By defining $t_{\rm eff}=n-mt$,

$$B/B_0 \approx 1 + b_{nm} \cos(t_{\text{eff}} \phi) , \qquad (1.3)$$

the dependence of the magnitude of the magnetic field can be written in a way similar to that in a tokamak.

The HSX stellarator has four field periods (n=4, m=1), and is designed with a rotational transform $t\approx 1$. Therefore $t_{\rm eff}\approx 3$ in HSX. The device has a $1.2\,{\rm m}$ average major radius and $15\,{\rm cm}$ average minor radius. The $B=1\,{\rm T}$ quasi-helically symmetric magnetic field is generated by a set of 48 modular coils with 12 coils per field period. Each field period is stellarator-symmetric 54 resulting in only 6 unique coil shapes. The field as produced by the coils has been confirmed to be dominated by the (4,1) mode and minimize non-symmetric components. 55 Plasmas are fueled throughout a $50\,{\rm ms}$ discharge by gas

puffing, and are heated by up to $100\,\mathrm{kW}$ of Electron Cyclotron Resonance Heating (ECRH). ECRH couples to the electrons, and ions are heated by collisions. Typical line-averaged plasma densities are $\approx 4\times10^{12}\,\mathrm{cm}^{-3}$, and core temperatures can reach $2\,\mathrm{keV}$.

The QHS and Mirror configurations

The standard operating configuration for HSX is the Quasi-Helical Symmetry configuration (QHS), where the magnetic spectrum is dominated by a (4,1) mode. However, a set of planar auxiliary coils can be energized to modify the magnetic spectrum, introducing non-symmetric terms similar to a conventional stellarator. This configuration flexibility has allowed experiments to directly compare quasi-symmetry to a variety of degraded-symmetry configurations. Experiments have previously demonstrated that flow damping 56 and neoclassical transport 2 are reduced in the QHS configuration by comparing to these broken symmetry configurations. Of particular interest to this work, it has been suggested that optimization for neoclassical transport can also reduce turbulent transport through the reduced damping of zonal flows. 57

The most studied of the degraded-symmetry configurations are the Mirror configurations, where the auxiliary coils are energized to add m=0 mirror terms to the spectrum. The configuration now known as "Old Mirror" introduces a (4,0) mode, but shifts the magnetic axis in the locations of the Thomson scattering profile diagnostic and ECRH heating, omitting measurements near the magnetic axis and changing the power deposition profile. In this work, "Mirror" refers to the "Flip 1-4 Mirror", developed in Reference 58. This configuration adds large (4,0) and (8,0) modes and avoids shifting the magnetic axis at the Thomson scattering diagnostic and ECRH heating. In addition, while quasi-symmetry is degraded, the plasma volume, rotational transform, and magnetic well depth are very similar between configurations. In other stellarators, these parameters are known to affect anomalous transport. ⁵⁹

While neoclassical transport is reduced in QHS, anomalous transport dominates the energy flux in both QHS and Mirror. As will be discussed next, the Trapped Electron Mode (TEM) is the dominant instability in HSX. Trapped particles in HSX are localized to regions of bad curvature, which increases the growth of TEMs. The additional mirror terms in the magnetic spectrum of the Mirror configuration increase the trapped particle fraction, but also reduces the overlap of particle trapping (minimum |B|) and bad curvature ($\kappa < 0$) regions This is shown in Figure 1.3 for a field line from the radial location r/a = 0.7, where r is the average minor radius of the flux surface of interest and a is the average minor radius of the last closed flux surface. According to the proxy from Reference 5 (see Appendix A), even after accounting for the increased trapped particle fraction in Mirror, this overlap is expected to make Mirror more stable to the TEM than QHS.

Previous work on the TEM in HSX

Calculations of the experimental heat diffusivity in HSX have shown that the neoclassical transport is reduced with quasi-symmetry inside r/a < 0.3, but also demonstrate that anomalous transport is much larger than the neoclassical contribution. 2,60,61 This is particularly true outside the core, r/a > 0.3, where the temperature profile is more flat and the density gradient is peaking. The normalized ion temperature gradient is likely small due to the low-density plasmas and significant charge exchange across the minor radius in HSX, and probably does not support Ion Temperature Gradient (ITG) modes. The Electron Temperature Gradient (ETG) mode likely exists in the core, but is stabilized when the density gradient is larger than the temperature gradient, and is unlikely to drive transport comparable to the experiment where the temperature profile is more flat. Fluctuations from ETG turbulence are on the scale of the electron gyroradius that is difficult to diagnose in the experiment. The Trapped Electron Mode (TEM) is largely responsible for anomalous transport in HSX, and previous work has provided a foundation for the comparison of

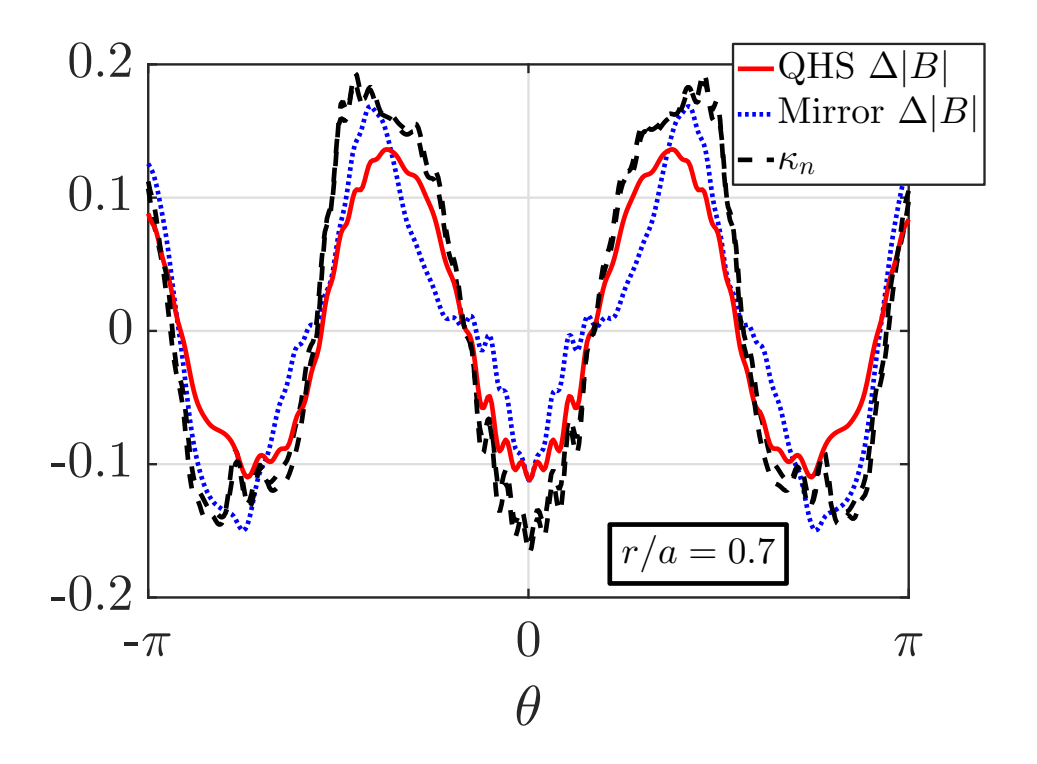


Figure 1.3: Comparison of the variation of the magnetic field $\Delta |B|$ and local curvature κ_n in the QHS and Mirror configurations along a field line, where θ is the poloidal coordinate. The difference of the local curvature in QHS and Mirror is nearly indiscernible. The Mirror configuration adds magnetic field in particle trapping regions, reducing the overlap of particle trapping and bad curvature.

experiment and simulation.

Initial analytic calculations showed that the TEM may be unstable in both the QHS and Mirror configurations, and that modes are more localized along the field line by magnetic curvature and local shear in the QHS configuration. 62,63 Growth rates were found to be largely similar between configurations. Linear gyrokinetic calculations in flux tube geometry predicted that the TEM is unstable in HSX, and that analysis with a quasilinear axisymmetric model, modified to account for the trapped particle fraction and larger curvature of QHS, closely matched the gyrokinetic growth rates. 64 Transport from this quasilinear model was able to match experimental energy transport for r/a > 0.3 in QHS, but an estimate of turbulence suppression by $E \times B$ flow shear was required to match

the peaked core temperature profile. Linear calculations also show larger growth rates in the Mirror configuration when driving gradients are large, particularly in a flux tube in the core (r/a=0.24). 60 This is attributed to the larger trapped particle population in Mirror. Langmuir probe measurements of density fluctuations, density-potential cross phase, particle flux, and growth rates were compared to a quasilinear model in $B=0.5\,\mathrm{T}$ QHS plasmas. 65 Measurements differed from the quasilinear model by a factor of 2-3, but showed significant variation across the flux surface. Density fluctuations, phase velocity, and particle flux were also compared between QHS and Mirror, but showed no significant difference between configurations.

While other measurements have not been compared to a turbulence model, they have shown that fluctuations increase strongly with the ∇n -drive and are insensitive to ∇T_e , ⁶⁶ consistent with the ∇n -driven TEM. Increasing density fluctuations are associated with a decrease in plasma flow, but probe measurements in the edge found that the Reynolds stress cannot account for the deviation of flow velocities from neoclassical predictions. ⁶⁷ Fluctuation comparisons have also found clear differences between the QHS and Mirror configurations. Fluctuation spectra measured with reflectometry are much broader in the Mirror configuration, ⁶⁸ a coherent mode that only appears in the Mirror configuration was identified with interferometry. ⁶⁹ However, it is unclear if these measurements directly relate to the TEM.

Recently, nonlinear simulations confirmed ∇n -driven TEM turbulence in the QHS configuration, and identified a double peak in the flux spectra that is not predicted by the linear growth rates. The simulations show zonal flows in saturated turbulence, but measurements in HSX have only identified zonal flows during strong biasing. The first comparison between experimental transport and nonlinear simulations of TEM turbulence used heat pulse propagation experiments on HSX within r/a < 0.4. The heat flux driven by the TEM was an order of magnitude larger than the experimental heat flux, while the

flux due to the ETG was an order of magnitude smaller. However, these simulations did not use experimental parameters, and further simulations demonstrated that extended flux tubes are needed to properly resolve eigenmodes in low-shear devices such as HSX.⁷³ These extended modes may also be involved in a path to turbulence saturation independent of the zonal flows.^{6,7} Prior to the studies described herein, nonlinear simulations at HSX had not used the experimental temperature ratio $T_{\rm i}/T_{\rm e}$, had not been compared to fluctuation measurements, and had not simulated TEM turbulence in the Mirror configuration.

1.3 Dissertation Overview

Very few validation studies exist for the three-dimensional geometry of a stellarator, and this dissertation starts the first steps of the process in the only existing quasi-symmetric stellarator. This work describes the first detailed comparison of experimental measurements in a stellarator to nonlinear gyrokinetic simulations of TEM turbulence at experimental parameters. The QHS and Mirror configurations provide an opportunity to predict how turbulent transport changes in quasi-symmetric and non-symmetric geometry, while matching the experimental conditions between configurations as closely as possible. By reproducing any difference between these configurations, validation will increase confidence in the ability of turbulence simulations to help design the next generation of optimized stellarators.

Experimental measurements of heat transport and density fluctuations are presented in Chapter 2. A large database of HSX profiles has been compiled, allowing discharges in the QHS and Mirror magnetic geometries to be matched for density and temperature profiles more closely than previously achievable. Power balance analysis shows that thermal transport is larger in the Mirror configuration when profile gradients are matched. A reduced power balance analysis is applied to profiles in the database, revealing that the heat flux increases with increasing density gradient but shows little dependence on the

temperature gradient. Comparison of two quantities between simulation and experiment reduces the likelihood of fortuitous agreement, and so a reflectometer is used to measure density fluctuations in a subset of these profiles. Density fluctuation amplitudes increase with increasing density gradient, but there is insufficient data to identify a difference between QHS and Mirror.

Gyrokinetic simulations of TEM turbulence using the Gene⁷⁴ code in a flux tube are presented in Chapter 3. This chapter contains the first nonlinear simulations in the Mirror configuration, as well as the first nonlinear simulations at experimental parameters in HSX. Linear calculations of the fastest-growing mode are used as a starting point to characterize configurations. While linear growth rates are smaller in Mirror than in QHS, as expected due to the reduced overlap of particle trapping regions and unfavorable curvature, the heat flux in nonlinear simulations is larger in the Mirror configuration at nominal profiles. The difference in heat flux between QHS and Mirror is eliminated with the experimentally relevant temperature ratio $T_i/T_e = 0.2$. The density and temperature gradients are varied in simulation, and while growth rates increase more strongly with the temperature gradient, the heat flux scales more strongly with the density gradient. Coincident changes of frequencies in nonlinear simulations suggest that the dynamics of the TEM are determined by nonlinear effects, and not only the linear instability. Finally, simulations are compared to the experimental heat flux and density fluctuation amplitude. The matched heat flux and gradient drive between simulation and experiment confirms that ∇n -driven TEM turbulence is the dominant cause of anomalous transport at the mid-radius in HSX.

Zonal flows are present in all simulations in Chapter 3 and can be important for TEM saturation.⁷⁵ In Chapter 4, the linear collisionless damping of the zonal flow is calculated in quasi-symmetric geometries for the first time. Comparisons of the QHS and Mirror configurations, as well as the quasi-axial symmetry configuration of the National Compact Stellarator experiment (NCSX), highlight zonal flow oscillations and long-time decay

that occur in plasmas with finite neoclassical radial drifts. Simulations are compared in flux-tube, flux-surface, and full-volume geometry to investigate the limitations of reduced geometry representations. While each flux tube on a flux surface is unique, several different flux tubes in HSX or NCSX can reproduce the zonal flow damping from a flux-surface calculation given an adequate parallel extent. Clear differences between the zonal flow damping in the QHS and Mirror configurations depend on the bounce-averaged radial particle drift in accordance with theory, and could provide a future point of comparison between simulation and experiment. The content of Chapter 4 has been published in Reference 76.

Chapter 5 will summarize the conclusions of this dissertation and present suggestions to continue the comparison of experimental measurements and turbulence simulations.

References

- [1] M. Kick, H. Maaßberg, M. Anton, J. Baldzuhn, M. Endler, C. Görner, M. Hirsch, A. Weller, and S. Zoletnik, *Electric field and transport in W7-AS*, Plasma Physics and Controlled Fusion **41**, A549 (1999).
- [2] J. M. Canik, D. T. Anderson, F. S. B. Anderson, K. M. Likin, J. N. Talmadge, and K. Zhai, *Experimental demonstration of improved neoclassical transport with quasihelical symmetry*, Physical Review Letters **98**, 085002 (2007).
- [3] W. Horton, *Drift waves and transport*, Reviews of Modern Physics **71**, 735 (1999).
- [4] H. E. Mynick, N. Pomphrey, and P. Xanthopoulos, *Optimizing stellarators for turbulent transport*, Physical Review Letters **105**, 095004 (2010).
- [5] J. H. E. Proll, H. E. Mynick, P. Xanthopoulos, S. A. Lazerson, and B. J. Faber, *TEM turbulence optimisation in stellarators*, Plasma Physics and Controlled Fusion **58**, 014006 (2016).
- [6] C. C. Hegna, P. W. Terry, and B. J. Faber, *Theory of ITG turbulent saturation in stellarators: Identifying mechanisms to reduce turbulent transport*, Physics of Plasmas **25**, 022511 (2018).
- [7] P. W. Terry, B. J. Faber, C. C. Hegna, V. V. Mirnov, M. J. Pueschel, and G. G. Whelan, *Saturation scalings of toroidal ion temperature gradient turbulence*, Physics of Plasmas **25**, 012308 (2018).
- [8] P. Xanthopoulos, H. E. Mynick, P. Helander, Y. Turkin, G. G. Plunk, F. Jenko, T. Görler, D. Told, T. Bird, and J. H. E. Proll, *Controlling turbulence in present and future stellarators*, Physical Review Letters **113**, 155001 (2014).
- [9] A. Bader, B. J. Faber, J. C. Schmitt, D. T. Anderson, M. Drevlak, J. M. Duff, H. Frerichs, C. C. Hegna, T. G. Kruger, M. Landreman, I. J. McKinney, L. Singh, J. M. Schroeder, P. W. Terry, and A. S. Ware, A new optimized quasihelically symmetric stellarator, (2020), arXiv:2004.11426 [physics].
- [10] P. W. Terry, M. Greenwald, J.-N. Leboeuf, G. R. McKee, D. R. Mikkelsen, W. M. Nevins, D. E. Newman, and D. P. Stotler, *Validation in fusion research: Towards guidelines and best practices*, Physics of Plasmas **15**, 062503 (2008).
- [11] M. Greenwald, *Verification and validation for magnetic fusion*, Physics of Plasmas 17, 058101 (2010).
- [12] A. E. White, *Validation of nonlinear gyrokinetic transport models using turbulence measure- ments*, Journal of Plasma Physics **85**, 745850101 (2019).

- [13] A. J. Brizard and T. S. Hahm, *Foundations of nonlinear gyrokinetic theory*, Reviews of Modern Physics **79**, 421 (2007).
- [14] C. Holland, Validation metrics for turbulent plasma transport, Physics of Plasmas 23, 060901 (2016).
- [15] T. L. Rhodes, J.-N. Leboeuf, R. D. Sydora, R. J. Groebner, E. J. Doyle, G. R. McKee, W. A. Peebles, C. L. Rettig, L. Zeng, and G. Wang, *Comparison of turbulence measurements from DIII-D low-mode and high-performance plasmas to turbulence simulations and models*, Physics of Plasmas **9**, 2141 (2002).
- [16] D. W. Ross and W. Dorland, *Comparing simulation of plasma turbulence with experiment*. *II. Gyrokinetic simulations*, Physics of Plasmas **9**, 5031 (2002).
- [17] J. Candy and R. E. Waltz, *Anomalous transport scaling in the DIII-D tokamak matched by supercomputer simulation*, Physical Review Letters **91**, 045001 (2003).
- [18] A. E. White, L. Schmitz, G. R. McKee, C. Holland, W. A. Peebles, T. A. Carter, M. W. Shafer, M. E. Austin, K. H. Burrell, J. Candy, J. C. DeBoo, E. J. Doyle, M. A. Makowski, R. Prater, T. L. Rhodes, G. M. Staebler, G. R. Tynan, R. E. Waltz, and G. Wang, *Measurements of core electron temperature and density fluctuations in DIII-D and comparison to nonlinear gyrokinetic simulations*, Physics of Plasmas **15**, 056116 (2008).
- [19] C. Holland, J. C. DeBoo, T. L. Rhodes, L. Schmitz, J. C. Hillesheim, G. Wang, A. E. White, M. E. Austin, E. J. Doyle, W. A. Peebles, C. C. Petty, L. Zeng, and J. Candy, *Testing gyrokinetic simulations of electron turbulence*, Nuclear Fusion **52**, 063028 (2012).
- [20] A. E. White, W. A. Peebles, T. L. Rhodes, C. H. Holland, G. Wang, L. Schmitz, T. A. Carter, J. C. Hillesheim, E. J. Doyle, L. Zeng, G. R. McKee, G. M. Staebler, R. E. Waltz, J. C. DeBoo, C. C. Petty, and K. H. Burrell, *Measurements of the cross-phase angle between density and electron temperature fluctuations and comparison with gyrokinetic simulations*, Physics of Plasmas 17, 056103 (2010).
- [21] S. J. Freethy, T. Görler, A. J. Creely, G. D. Conway, S. S. Denk, T. Happel, C. Koenen, P. Hennequin, and A. E. White, *Validation of gyrokinetic simulations with measurements of electron temperature fluctuations and density-temperature phase angles on ASDEX Upgrade*, Physics of Plasmas **25**, 055903 (2018).
- [22] D. Told, F. Jenko, T. Görler, F. J. Casson, and E. Fable, *Characterizing turbulent transport in ASDEX Upgrade L-mode plasmas via nonlinear gyrokinetic simulations*, Physics of Plasmas **20**, 122312 (2013).
- [23] T. Görler, A. E. White, D. Told, F. Jenko, C. Holland, and T. L. Rhodes, *A flux-matched gyrokinetic analysis of DIII-D L-mode turbulence*, Physics of Plasmas **21**, 122307 (2014).
- [24] J. Citrin, F. Jenko, P. Mantica, D. Told, C. Bourdelle, R. Dumont, J. Garcia, J. W. Haverkort, G. M. D. Hogeweij, T. Johnson, and M. J. Pueschel, *Ion temperature profile*

- stiffness: Non-linear gyrokinetic simulations and comparison with experiment, Nuclear Fusion 54, 023008 (2014).
- [25] F. van Wyk, E. G. Highcock, A. R. Field, C. M. Roach, A. A. Schekochihin, F. I. Parra, and W. Dorland, *Ion-scale turbulence in MAST: Anomalous transport, subcritical transitions, and comparison to BES measurements*, Plasma Physics and Controlled Fusion **59**, 114003 (2017).
- [26] A. J. Creely, N. T. Howard, P. Rodriguez-Fernandez, N. Cao, A. E. Hubbard, J. W. Hughes, J. E. Rice, A. E. White, J. Candy, G. M. Staebler, G. D. Conway, S. J. Freethy, and C. Sung, *Validation of nonlinear gyrokinetic simulations of L- and I-mode plasmas on Alcator C-Mod*, Physics of Plasmas **24**, 056104 (2017).
- [27] N. T. Howard, C. Holland, A. E. White, M. Greenwald, P. Rodriguez-Fernandez, J. Candy, and A. J. Creely, *Multi-scale gyrokinetic simulations of an Alcator C-Mod, ELM-y H-mode plasma*, Plasma Physics and Controlled Fusion **60**, 014034 (2017).
- [28] M. J. Pueschel, D. R. Hatch, M. Kotschenreuther, A. Ishizawa, and G. Merlo, *Multi-scale interactions of microtearing turbulence in the tokamak pedestal*, Nuclear Fusion **60**, 124005 (2020).
- [29] A. Casati, T. Gerbaud, P. Hennequin, C. Bourdelle, J. Candy, F. Clairet, X. Garbet, V. Grandgirard, Ö. D. Gürcan, S. Heuraux, G. T. Hoang, C. Honoré, F. Imbeaux, R. Sabot, Y. Sarazin, L. Vermare, and R. E. Waltz, *Turbulence in the TORE SUPRA tokamak: Measurements and validation of nonlinear simulations*, Physical Review Letters **102**, 165005 (2009).
- [30] H. Arnichand, J. Citrin, S. Hacquin, R. Sabot, A. Krämer-Flecken, X. Garbet, C. Bourdelle, C. Bottereau, F. Clairet, J. C. Giacalone, Z. O. Guimarães-Filho, R. Guirlet, G. Hornung, A. Lebschy, P. Lotte, P. Maget, A. Medvedeva, D. Molina, V. Nikolaeva, D. Prisiazhniuk, and the Tore Supra and ASDEX Upgrade Teams, *Identification of trapped electron modes in frequency fluctuation spectra*, Plasma Physics and Controlled Fusion 58, 014037 (2016).
- [31] S. Hacquin, J. Citrin, H. Arnichand, R. Sabot, C. Bourdelle, X. Garbet, and A. Krämer-Flecken, *Simulation of core turbulence measurement in Tore Supra ohmic regimes*, Physics of Plasmas **23**, 092303 (2016).
- [32] J. Citrin, H. Arnichand, J. Bernardo, C. Bourdelle, X. Garbet, F. Jenko, S. Hacquin, M. J. Pueschel, and R. Sabot, *Comparison between measured and predicted turbulence frequency spectra in ITG and TEM regimes*, Plasma Physics and Controlled Fusion **59**, 064010 (2017).
- [33] G. D. Conway, B. Kurzan, B. Scott, E. Holzhauer, and M. Kaufmann, *Coupling of turbulence and reflectometer simulation codes and comparison with experiment*, Plasma Physics and Controlled Fusion 44, 451 (2002).

- [34] S. Leerink, V. V. Bulanin, E. Z. Gusakov, J. Heikkinen, S. J. Janhunen, T. P. Kiviniemi, T. Korpilo, M. Nora, and F. Ogando, *Synthetic Doppler reflectometer diagnostic for nonlinear global gyrokinetic simulations*, Contributions to Plasma Physics **50**, 242 (2010).
- [35] U. Stroth, A. B. Navarro, G. D. Conway, T. Görler, T. Happel, P. Hennequin, C. Lechte, P. Manz, P. Simon, A. Biancalani, E. Blanco, C. Bottereau, F. Clairet, S. Coda, T. Eibert, T. Estrada, A. Fasoli, L. Guimarais, Ö. Gürcan, Z. Huang, F. Jenko, W. Kasparek, C. Koenen, A. Krämer-Flecken, M. E. Manso, A. Medvedeva, D. Molina, V. Nikolaeva, B. Plaum, L. Porte, D. Prisiazhniuk, T. Ribeiro, B. D. Scott, U. Siart, A. Storelli, L. Vermare, and S. Wolf, Experimental turbulence studies for gyro-kinetic code validation using advanced microwave diagnostics, Nuclear Fusion 55, 083027 (2015).
- [36] C. Lechte, G. D. Conway, T. Görler, C. Tröster, and the ASDEX Upgrade Team, *Doppler reflectometry simulations for ASDEX Upgrade*, in *Proc. 41st EPS Conf. on Plasma Physics* (Berlin, Germany, 2014).
- [37] T. Happel, T. Görler, P. Hennequin, C. Lechte, M. Bernert, G. D. Conway, S. J. Freethy, C. Honoré, J. R. Pinzón, U. Stroth, and the ASDEX Upgrade Team, *Comparison of detailed experimental wavenumber spectra with gyrokinetic simulation aided by two-dimensional full-wave simulations*, Plasma Physics and Controlled Fusion **59**, 054009 (2017).
- [38] C. Lechte, G. D. Conway, T. Görler, C. Tröster-Schmid, and the ASDEX Upgrade Team, *X mode Doppler reflectometry k-spectral measurements in ASDEX Upgrade: Experiments and simulations*, Plasma Physics and Controlled Fusion **59**, 075006 (2017).
- [39] K. Tanaka, C. Michael, L. N. Vyacheslavov, M. Yokoyama, S. Murakami, A. Wakasa, H. Takenaga, K. Muraoka, K. Kawahata, T. Tokuzawa, T. Akiyama, K. Ida, M. Yoshinuma, I. Yamada, K. Narihara, H. Yamada, and the LHD Experimental Group, *Particle transport and fluctuation characteristics around the neoclassically optimized configuration in LHD*, Plasma and Fusion Research 3, S1069 (2008).
- [40] M. Nunami, T.-H. Watanabe, H. Sugama, and K. Tanaka, *Gyrokinetic turbulent transport simulation of a high ion temperature plasma in Large Helical Device experiment*, Physics of Plasmas **19**, 042504 (2012).
- [41] T. Watanabe, M. Nunami, H. Sugama, S. Satake, S. Matsuoka, A. Ishizawa, S. Maeyama, and K. Tanaka, *Turbulence spectra, transport, and* $E \times B$ *flows in helical plasmas*, in *Proceedings of the 24th IAEA Fusion Energy Conference* (International Atomic Energy Agency, 2012).
- [42] A. Ishizawa, T.-H. Watanabe, H. Sugama, M. Nunami, K. Tanaka, S. Maeyama, and N. Nakajima, *Turbulent transport of heat and particles in a high ion temperature discharge of the Large Helical Device*, Nuclear Fusion 55, 043024 (2015).
- [43] A. Ishizawa, Y. Kishimoto, T.-H. Watanabe, H. Sugama, K. Tanaka, S. Satake, S. Kobayashi, K. Nagasaki, and Y. Nakamura, *Multi-machine analysis of turbulent transport in helical systems via gyrokinetic simulation*, Nuclear Fusion **57**, 066010 (2017).

- [44] M. Nunami, M. Nakata, S. Toda, A. Ishizawa, R. Kanno, and H. Sugama, *Simulation studies on temperature profile stiffness in ITG turbulent transport of helical plasmas for flux-matching technique*, Physics of Plasmas **25**, 082504 (2018).
- [45] S. Toda, M. Nakata, M. Nunami, A. Ishizawa, T.-H. Watanabe, and H. Sugama, *Transport simulation for helical plasmas by use of gyrokinetic transport model*, Plasma and Fusion Research **14**, 3403061 (2019).
- [46] F. Fernández-Marina, T. Estrada, and E. Blanco, *Turbulence radial correlation length measurements using Doppler reflectometry in TJ-II*, Nuclear Fusion **54**, 072001 (2014).
- [47] E. Sanchez, T. Estrada, J. L. Velasco, I. Calvo, A. Cappa, J. A. Alonso, J. M. García-Regaña, R. Kleiber, and J. Riemann, *Validation of global gyrokinetic simulations in stellarator configurations*, Nuclear Fusion **59**, 076029 (2019).
- [48] J. A. Alonso, I. Calvo, J. L. Velasco, K. J. McCarthy, A. Chmyga, L. G. Eliseev, T. Estrada, R. Kleiber, L. I. Krupnik, A. V. Melnikov, P. Monreal, F. I. Parra, S. Perfilov, and A. I. Zhezhera, *Observation of oscillatory radial electric field relaxation in a helical plasma*, Physical Review Letters **118**, 185002 (2017).
- [49] E. Sánchez, I. Calvo, J. L. Velasco, F. Medina, A. Alonso, P. Monreal, and R. Kleiber, *Oscillatory relaxation of zonal flows in a multi-species stellarator plasma*, Plasma Physics and Controlled Fusion **60**, 094003 (2018).
- [50] R. Sharma, P. O. Khabanov, A. V. Melnikov, C. Hidalgo, A. Cappa, A. Chmyga, L. G. Eliseev, T. Estrada, N. K. Kharchev, A. S. Kozachek, L. I. Krupnik, A. Malaquias, B. van Milligen, A. Molinero, J. L. de Pablos, I. Pastor, and V. N. Zenin, *Measurements of 2D poloidal plasma profiles and fluctuations in ECRH plasmas using the heavy ion beam probe system in the TJ-II stellarator*, Physics of Plasmas **27**, 062502 (2020).
- [51] J. A. Alcusón, P. Xanthopoulos, G. G. Plunk, P. Helander, F. Wilms, Y. Turkin, A. von Stechow, and O. Grulke, *Suppression of electrostatic micro-instabilities in maximum-J stellarators*, Plasma Physics and Controlled Fusion **62**, 035005 (2020).
- [52] P. Xanthopoulos, S. A. Bozhenkov, M. N. Beurskens, H. M. Smith, G. G. Plunk, P. Helander, C. D. Beidler, J. A. Alcusón, A. Alonso, A. Dinklage, O. Ford, G. Fuchert, J. Geiger, J. H. E. Proll, M. J. Pueschel, Y. Turkin, F. Warmer, and the W7-X Team, *Turbulence mechanisms of enhanced performance stellarator plasmas*, Physical Review Letters 125, 075001 (2020).
- [53] F. S. B. Anderson, A. F. Almagri, D. T. Anderson, P. G. Matthews, J. N. Talmadge, and J. L. Shohet, *The Helically Symmetric Experiment*, (HSX) Goals, design and status, Fusion Technology **27**, 273 (1995).
- [54] R. Dewar and S. Hudson, *Stellarator symmetry*, Physica D: Nonlinear Phenomena **112**, 275 (1998).

- [55] J. N. Talmadge, V. Sakaguchi, F. S. B. Anderson, D. T. Anderson, and A. F. Almagri, Experimental determination of the magnetic field spectrum in the Helically Symmetric Experiment using passing particle orbits, Physics of Plasmas 8, 5165 (2001).
- [56] S. P. Gerhardt, J. N. Talmadge, J. M. Canik, and D. T. Anderson, *Experimental evidence of reduced plasma flow damping with quasisymmetry*, Physical Review Letters **94**, 015002 (2005).
- [57] T.-H. Watanabe, H. Sugama, and S. Ferrando-Margalet, *Reduction of turbulent transport with zonal flows enhanced in helical systems*, Physical Review Letters **100**, 195002 (2008).
- [58] J. M. Canik, Measurements of Reduced Neoclassical Particle and Electron Heat Transport with Quasisymmetry in the HSX Stellarator, Ph.D. thesis, The University of Wisconsin-Madison (2007).
- [59] U. Stroth, M. Murakami, R. A. Dory, H. Yamada, S. Okamura, F. Sano, and T. Obiki, *Energy confinement scaling from the international stellarator database*, Nuclear Fusion **36**, 1063 (1996).
- [60] W. A. Guttenfelder, Measurements and Modeling of Turbulent Transport in the HSX Stellarator, Ph.D. thesis, The University of Wisconsin-Madison (2008).
- [61] J. D. Lore, Measurement and Transport Modeling with Momentum Conservation of an *Electron Internal Transport Barrier in HSX*, Ph.D. thesis, The University of Wisconsin-Madison (2010).
- [62] T. Rafiq and C. C. Hegna, *Drift waves in helically symmetric stellarators*, Physics of Plasmas **12**, 112505 (2005).
- [63] T. Rafiq and C. C. Hegna, *Dissipative trapped-electron instability in quasihelically symmetric stellarators*, Physics of Plasmas **13**, 062501 (2006).
- [64] W. Guttenfelder, J. Lore, D. T. Anderson, F. S. B. Anderson, J. M. Canik, W. Dorland, K. M. Likin, and J. N. Talmadge, *Effect of quasihelical symmetry on trapped-electron mode transport in the HSX stellarator*, Physical Review Letters **101**, 215002 (2008).
- [65] W. Guttenfelder, D. T. Anderson, F. S. B. Anderson, J. M. Canik, K. M. Likin, and J. N. Talmadge, *Edge turbulence measurements in electron-heated Helically Symmetric Experiment plasmas*, Physics of Plasmas **16**, 082508 (2009).
- [66] C. B. Deng, D. L. Brower, D. T. Anderson, F. S. B. Anderson, A. Briesemeister, and K. M. Likin, *Core density turbulence in the HSX Stellarator*, Nuclear Fusion **55**, 123003 (2015).
- [67] R. S. Wilcox, J. N. Talmadge, D. T. Anderson, F. S. B. Anderson, and J. D. Lore, *Intrinsic plasma rotation and Reynolds stress at the plasma edge in the HSX stellarator*, Nuclear Fusion **56**, 036002 (2016).

- [68] K. M. Likin, C. Lechte, H. Lu, and F. S. B. Anderson, ECE and reflectometry on the Helically Symmetric Experiment, in Proceedings of ITC/ISHW2007 (2007).
- [69] C. B. Deng and D. L. Brower, *Core density gradient fluctuation measurement by differential interferometry in the Helically Symmetric Experiment stellarator*, Review of Scientific Instruments **83**, 10E308 (2012).
- [70] B. J. Faber, M. J. Pueschel, J. H. E. Proll, P. Xanthopoulos, P. W. Terry, C. C. Hegna, G. M. Weir, K. M. Likin, and J. N. Talmadge, *Gyrokinetic studies of trapped electron mode turbulence in the Helically Symmetric eXperiment stellarator*, Physics of Plasmas 22, 072305 (2015).
- [71] R. S. Wilcox, B. P. van Milligen, C. Hidalgo, D. T. Anderson, J. N. Talmadge, F. S. B. Anderson, and M. Ramisch, *Measurements of bicoherence and long-range correlations during biasing in the HSX stellarator*, Nuclear Fusion **51**, 083048 (2011).
- [72] G. M. Weir, B. J. Faber, K. M. Likin, J. N. Talmadge, D. T. Anderson, and F. S. B. Anderson, *Profile stiffness measurements in the Helically Symmetric experiment and comparison to nonlinear gyrokinetic calculations*, Physics of Plasmas **22**, 056107 (2015).
- [73] B. J. Faber, M. J. Pueschel, P. W. Terry, C. C. Hegna, and J. E. Roman, *Stellarator microinstabilities and turbulence at low magnetic shear*, Journal of Plasma Physics **84**, 905840503 (2018).
- [74] F. Jenko, W. Dorland, M. Kotschenreuther, and B. N. Rogers, *Electron temperature gradient driven turbulence*, Physics of Plasmas 7, 1904 (2000).
- [75] D. R. Ernst, J. Lang, W. M. Nevins, M. Hoffman, Y. Chen, W. Dorland, and S. Parker, Role of zonal flows in trapped electron mode turbulence through nonlinear gyrokinetic particle and continuum simulation, Physics of Plasmas **16**, 055906 (2009).
- [76] J. Smoniewski, E. Sánchez, I. Calvo, M. J. Pueschel, and J. N. Talmadge, *Comparison of local and global gyrokinetic calculations of collisionless zonal flow damping in quasi-symmetric stellarators*, Physics of Plasmas **28**, 042503 (2021).

Experimental measurements in HSX

The same work that demonstrated reduced neoclassical transport with quasi-symmetry 1,2 showed that the experimental transport is much larger than the neoclassical contribution. As discussed in Section 1.2, the Trapped Electron Mode (TEM) is expected to be the most unstable mode in HSX and responsible for significant anomalous transport. The TEM can be driven by density or temperature gradients and drives fluctuations of those quantities. Interferometry measurements of density fluctuations on HSX scale strongly with the density gradient while showing a small or inverse relationship with the temperature gradient. Assuming these fluctuations are due to TEM turbulence, the ∇n -driven TEM is the primary turbulence drive mechanism in HSX. The TEM drives fluctuations in the temperature and density, which can in turn drive energy or particle transport. This study chooses measurements of energy transport and density fluctuations for comparison to simulation.

Previous studies of energy transport in the QHS and Mirror configurations range from finding smaller, ⁴ similar ^{2,5} or larger anomalous transport in Mirror than in QHS. ² Following these studies, Section 2.2 will examine energy transport in the QHS and Mirror configurations for comparison to simulation. Studies that match profiles in different configurations require a definition of matched profiles, such as matched density and temperature profiles, matched fueling and heating, or matched gradients. It can be difficult or infeasible to simultaneously match all the above conditions. Instead, this study examines

the scaling of heat flux with driving gradients. A reduced model of the power balance in HSX plasmas is used to calculate the heat flux for a large number of profiles with a range of driving gradients. Only measurements of the electron density and temperature profiles and total absorbed power are required, all of which are standard measurements during HSX discharges.

A proper validation study cannot depend on merely a single measurement for comparison to simulation. Turbulence simulations are extremely sensitive to input parameters such as driving gradients, and experimental measurements of those gradients involve large uncertainty. The heat flux is a global measure of energy transport, but involves multiple experimental measurements and models of energy deposition and transport. A simultaneous measurement of fluctuation amplitudes reduces the chances of finding accidental agreement with simulated turbulent transport while also providing a direct measurement of the underlying turbulence. The peak density gradient is too far from the plasma edge to be accessible to Langmuir probes. Instead, a reflectometer is used to measure density fluctuations. Reflectometry measures the phase and amplitude of the reflection of a microwave beam from the plasma. The beam is reflected from a cutoff layer set by the wave polarization and electron density, and so localization is determined by the density gradient. This diagnostic has the advantage of being most sensitive at the steep density gradient, precisely where the ∇n -driven TEM is expected to be most unstable. In Section 2.3, measurements of the density fluctuation amplitude are made in the QHS and Mirror configurations for comparison to simulation.

2.1 An HSX profile database

This study examines the trend of heat flux and density fluctuations as a function of driving gradients. This requires HSX profiles that scan the density and temperature gradient, but

experimental control of those profiles is limited. In addition, each Thomson scattering profile requires multiple reproducible discharges to accumulate sufficient photon counting statistics. It is currently infeasible to control the density and temperature gradient precisely enough to execute such a scan. Instead, this study has adopted reduced heat flux and density fluctuation analyses that can be applied to a number of profiles largely unsupervised. This opens up the entire HSX data archive to look for profiles across a range of gradients.

Example profiles of the electron temperature and density from Thomson scattering are plotted in Figure 2.1. The radial coordinate ρ is defined as r/a, defined by

$$\rho = \frac{r}{a} = \sqrt{\frac{\Psi}{\Psi_0}} \,, \tag{2.1}$$

where Ψ/Ψ_0 is the toroidal flux normalized to the toroidal flux at the last closed flux surface, and a is the average minor radius of that surface. Density and temperature gradients are normalized as a/L_n and a/L_{Te} , where $L_n^{-1} = -\nabla \ln n$ and $L_{Te}^{-1} = -\nabla \ln T_e$. The HSX Thomson scattering diagnostic requires 2-12 reproducible plasma discharges to accumulate statistics, and provides measurements of the electron density n_e and temperature T_e at 10 points across the minor radius⁶.

Discharges are judged to be reproducible by comparing a number of operational and plasma parameters. Matched heating power, magnet current, neutral pressure, and timing of diagnostic data collection ensure that the experimental setup is not changing between discharges. Interferometry is used to measure the line-averaged plasma density, and is the primary diagnostic that guides operations when trying to reproduce discharges. A diamagnetic loop measures the total plasma energy W, and is also essential for the thermal transport analysis in Section 2.2. Assuming that transport is changing slowly compared to changes in heating, the only change in power to the plasma when heating is turned off will be the power absorbed from ECRH. Then the absorbed power is

$$P_{\rm abs} = \left. \frac{dW}{dt} \right|^{t-} - \left. \frac{dW}{dt} \right|^{t+} , \qquad (2.2)$$

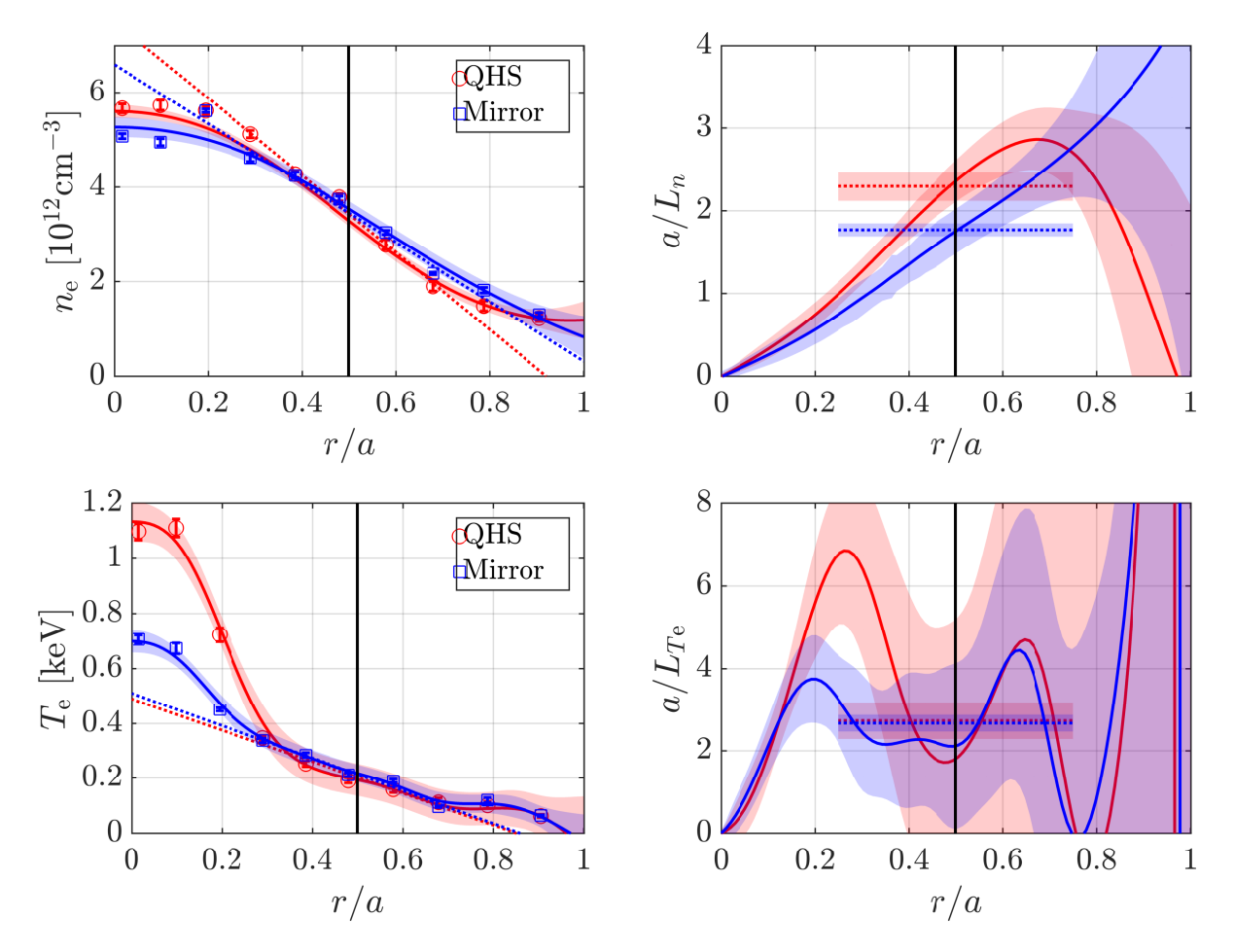


Figure 2.1: Temperature and density profiles and their normalized gradients when the absorbed ECRH power $P_{\rm abs}=18\pm3\,{\rm kW}$ is the same in both the QHS (red) and Mirror (blue) configurations. Measurements from Thomson scattering are plotted as symbols. Gaussian process regression is used to make a smooth fit to the experimental data, and dotted lines are a linear fit to $0.3\leq r/a\leq 0.7$. The shaded regions are the 1σ uncertainty of the fits. The temperature gradient peaks within $r/a\lesssim 0.3$, while the density gradient is largest for $r/a\gtrsim 0.5$.

where t- and t+ refer to the time immediately before and after the ECRH turnoff, respectively. Plasma profile changes may be driven by the ratio of ionization in the plasma core versus in the edge, and this is indicated by H_{α} emission profiles. The total radiated power from the plasma is measured by bolometers, and generally indicates impurity content of the plasma. To be included in an ensemble of discharges, each of these quantities is required to be within $\approx 10\%$ of the ensemble average for at least $10\,\mathrm{ms}$ before the Thomson scattering laser is fired and profile data is collected.

Gaussian process regression (GPR) is a robust way to fit entire profiles, gradients, and their uncertainty, and is a powerful tool to combine diagnostic observations to infer one consistent profile. A GPR tool was used to fit some profiles from the HSX profile database and compare to a linear fit. As seen in Figures 2.1, the mid-radius $0.3 \le r/a \le 0.7$ is adequately represented by a linear fit to density and temperature profiles. The uncertainty is much larger in the GPR fits due to the added complexity of fitting the whole profile to an underlying shape model, while the linear fit only includes 5 points about the mid-radius. In addition, GPR fitting as currently implemented requires significant intervention to find good fits for profiles, which makes it unfeasible to use for the hundreds of profiles in this study. Therefore, this study uses the linear fit y = mx + b to derive gradients from density and temperature profiles. The linear fit is not always a good representation of the mid-radius, and these cases are generally identified by large gradient uncertainties $\delta(a/L) > 2$. However, studies that require profiles or gradients away from r/a = 0.5 will need to use GPR or similar to fit the whole profile, and future work towards integrated data analysis at HSX could greatly reduce uncertainty in the GPR fit.

A database of 200 profiles has been collected consisting of 1435 plasma shots. The distribution of gradients in the database is shown in Figure 2.2, where it is immediately clear that both gradients a/L_n and a/L_{Te} tend to be larger in QHS than in Mirror profiles. It is not clear if this is a physical effect, or due to sampling bias from the fact that experimental

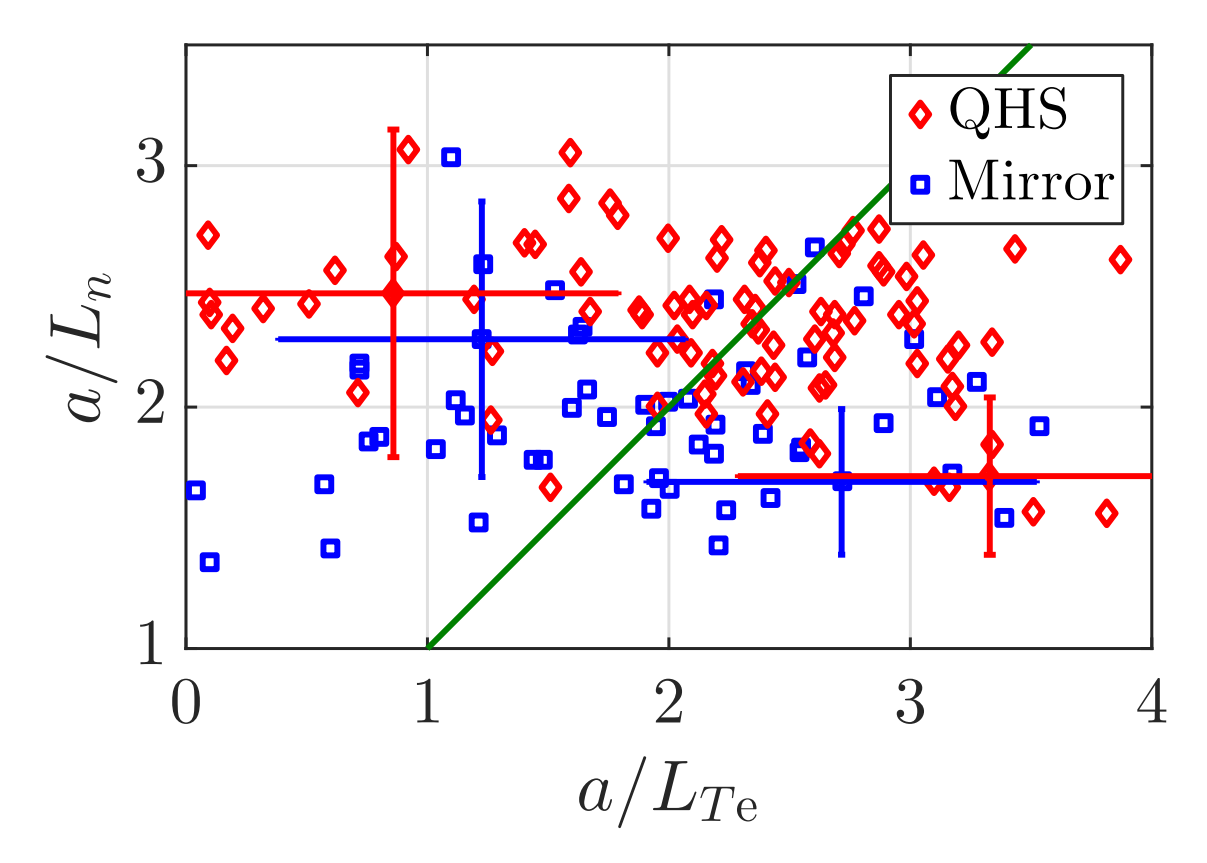


Figure 2.2: The distribution of gradients in the HSX profile database at r/a=0.5 for QHS (red diamonds) and Mirror (blue squares). Several points are drawn with a representative uncertainty. The straight green line corresponds to $a/L_{\rm Te}=a/L_n$, and QHS profiles tend towards the upper right part of the plot.

operations have more fully explored the QHS operation space. The database can be filtered by any standard measurements at HSX, such as $n_{\rm e}$, $T_{\rm e}$, and absorbed power $P_{\rm abs}$, to find similar plasma profiles. Further filtering can select a narrow range of a/L_n or $a/L_{\rm Te}$ to compare the scaling of a measurement with driving gradient. Previously at HSX, plasma fueling and heating was adjusted during experimental operations to attempt to match plasma conditions, a process that required multiple days of experimental operations. Often, plasmas were matched solely on the line-averaged density measured by interferometry. By

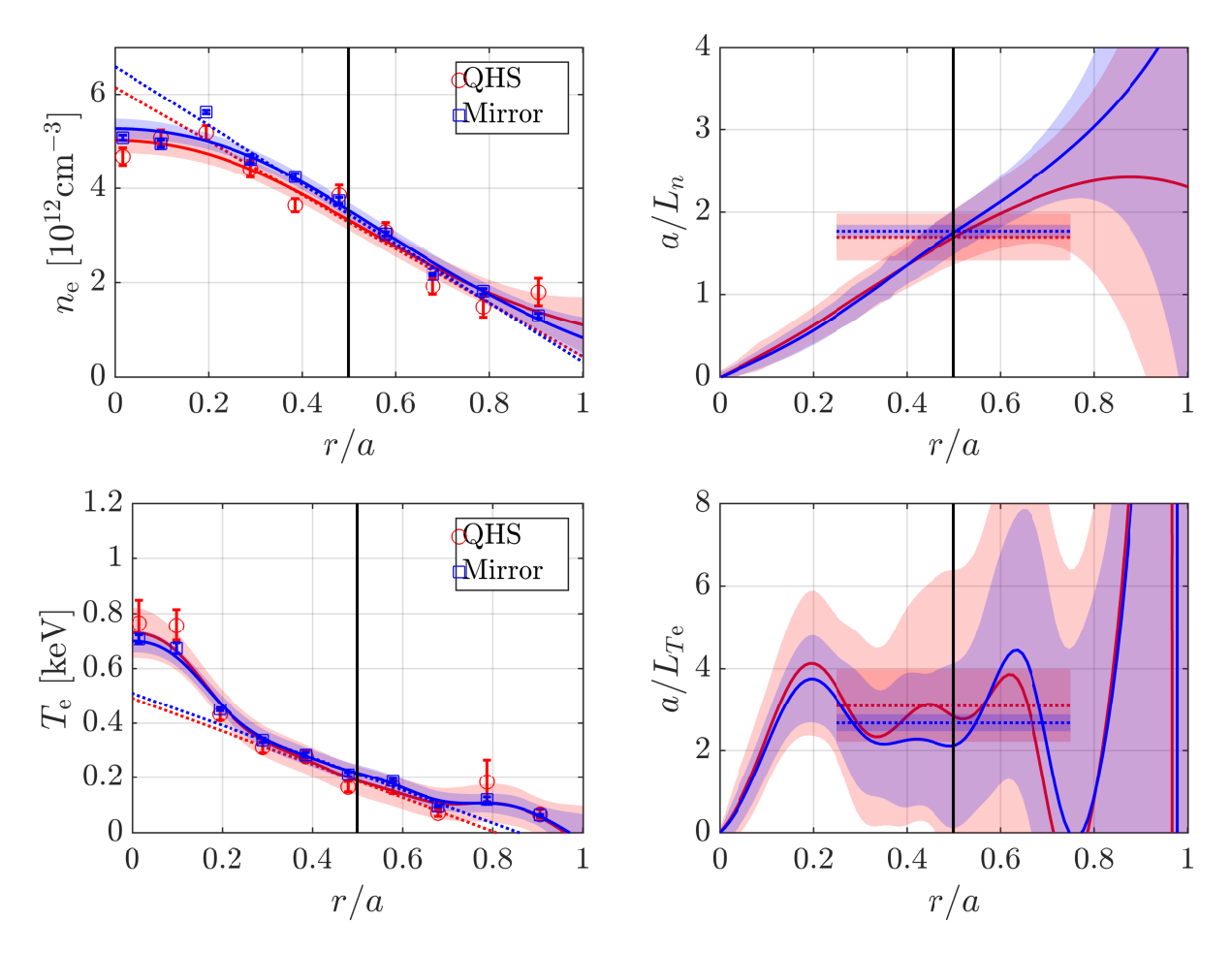


Figure 2.3: The HSX profile database enables matching QHS and Mirror profiles to within experimental uncertainties. An atypical QHS discharge is required to avoid the typically larger core temperature and mid-radius density gradient. Here, the QHS profile is from operations when the magnetic field was reversed as to its normal direction. Data from Thomson scattering is plotted as points, and Gaussian process regression is used to make a smooth fit to the experimental data. The dotted straight lines are a linear fit to $0.3 \lesssim r/a \lesssim 0.7$. The shaded regions are the 1σ uncertainty of the linear and GPR fits.

collecting a large amount of archived profiles, new criteria can be used to find comparable plasma discharges. In the past, QHS and Mirror profile have been compared for the same launched ECRH power. The profiles in Figure 2.1 were found by filtering the database for QHS and Mirror profiles with the same absorbed power $P_{\rm abs} = 18 \pm 3 \, \rm kW$. The QHS profile comes from a typical set of discharges with 44 kW of launched power. In the Mirror profile, 100 kW of power were launched, but half of that heating power was modulated, resulting in the same absorbed power. As seen in Figure 2.1, the temperature is typically more peaked towards the magnetic axis and the mid-radius density gradient is larger in QHS as compared to Mirror. Efforts to match profiles use less heating power in the QHS configuration to compensate, but have not been able to match both core parameters and gradients between configurations. The database compiled for the present work has enabled matching profiles between QHS and Mirror across the entire minor radius to within experimental uncertainties for the first time, as seen in Figure 2.3. The Mirror profile is the same as in Figure 2.1, but precise profile matching requires an atypical QHS discharge where the magnetic field was reversed with respect to its normal direction. Reversed-field operations have exhibited an asymmetry in ion flows, 9 but any further investigation of these profile changes is left to future work.

Measurements in this chapter target the mid-radius $r/a \approx 0.5$, where anomalous transport and the normalized density gradient are both large. Deep in the core of the plasma, density gradients are small, and the large temperature gradient may make the ETG mode important, which exists at scales too small to be measured by current diagnostics on HSX. Within $r/a \lesssim 0.3$, neoclassical calculations predict very strong $E \times B$ shearing that could have a suppression effect on turbulence, possibly complicating interpretation of the TEM. For r/a > 0.3, the electric field is measured to be relatively constant with very little shear, 11,12 and is not expected to affect turbulence. Towards the edge, r/a > 0.8, the low density and temperature in HSX plasmas make charge exchange and ionization

important parts of transport, which is outside the scope of this work. Finally, reflectometer measurements are only available for electron densities $n_{\rm e}\gtrsim 3.5\times 10^{12}\,{\rm cm^{-3}}$, corresponding to $r/a\lesssim 0.5$. While the matched profiles in this section compared plasmas across the entire minor radius, the gradient scans in this chapter only compare plasma parameters at the mid-radius.

2.2 Electron energy transport

This study examines the dependence of energy transport, quantified by the electron heat flux $Q_{\rm e}$, on the density a/L_n and temperature $a/L_{\rm Te}$ gradients. In this section, measurements of the heat flux take advantage of several assumptions. The flux-surface-averaged energy continuity equation for the electrons is

$$\frac{\partial}{\partial t} \left(\frac{3}{2} n_{\rm e} T_{\rm e} \right) + \frac{\partial}{\partial V} \left\langle Q_{\rm e} \cdot \nabla V \right\rangle = \sum P(V) , \qquad (2.3)$$

where V is the volume enclosed by a flux surface, $\langle \cdot \rangle$ denotes a flux-surface average, and $\sum P(\rho)$ is the sum of all energy sources and sinks. The volume is only a function of the radial coordinate, defined as $\rho = r/a$, and so $V = V(\rho)$, $dV = V'd\rho$, and $\nabla V = V'\nabla\rho$, where $V' = dV/d\rho$. In steady state, Equation (2.3) can be written as

$$\frac{1}{V'}\frac{\partial}{\partial\rho}V'\langle Q_{\rm e}\cdot\nabla\rho\rangle = \sum P(\rho) . \qquad (2.4)$$

Integrating Equation (2.4) over ρ , one obtains

$$Q_{\rm e} = \frac{\int_0^\rho \sum P(\rho') V'(\rho') d\rho'}{V'(\rho) \langle |\nabla \rho| \rangle} . \tag{2.5}$$

Previous studies on HSX assumed diffusive energy transport, using $Q=-n\chi\nabla T$ and calculated the experimental thermal diffusivity

$$\chi_{\rm e} = -\frac{\int_0^\rho \sum P(\rho')V'(\rho')d\rho'}{V'\langle |\nabla \rho|^2 \rangle n\frac{\partial T}{\partial \rho}} \,. \tag{2.6}$$

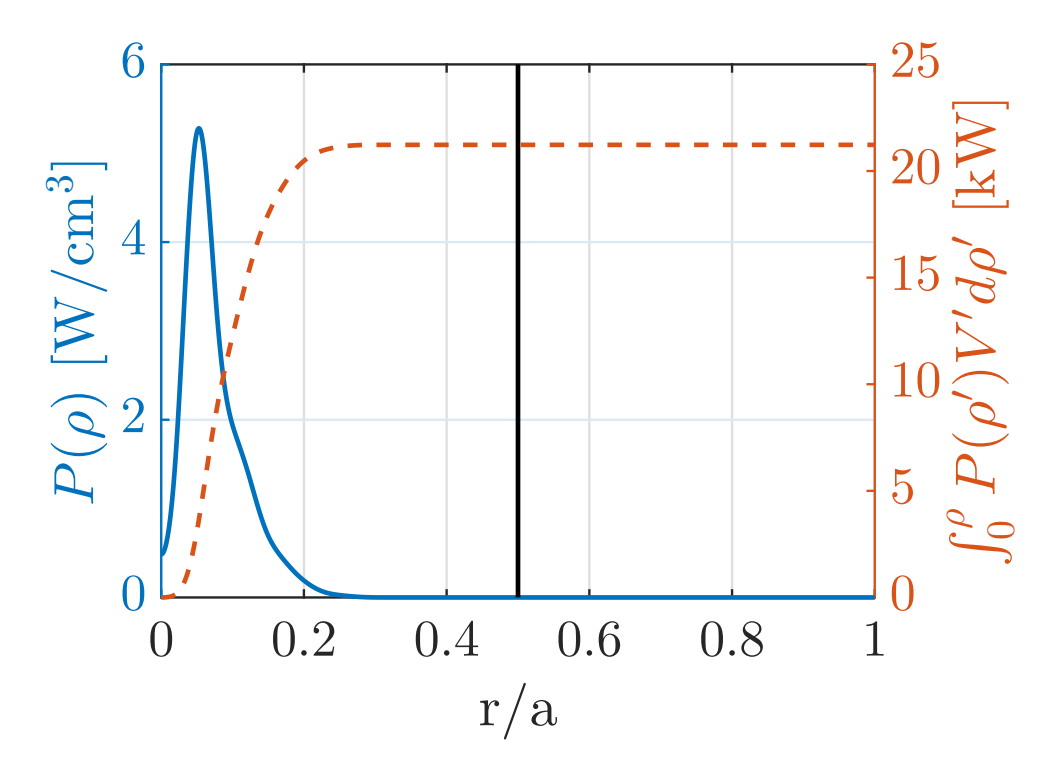


Figure 2.4: The heating power from ECRH $P(\rho)$ (solid line) is deposited within $r/a \approx 0.3$ as calculated by ray-tracing. The absorbed power (dashed line) is the integrated power deposited inside the flux surface. For power balance at r/a = 0.5 (black line), the power deposited inside the flux surface is the total absorbed power $P_{\rm abs}$.

The diffusivity is a normalized measure of energy transport which can be used to make comparisons between plasmas with varying pressure profiles. However, the temperature gradient introduces very large uncertainty into the calculation. This study selects a range of similar plasmas and calculates the heat flux $Q_{\rm e}$ as in Equation (2.5), as well as the thermal diffusivity $\chi_{\rm e}$ as in Equation (2.6).

The only source of energy is the absorbed power from electron cyclotron resonance heating (ECRH). While energy is lost due to radiated power, ionization, and electron-ion collisions, these account for a small fraction of the absorbed power. For the profiles in Figures 2.1 and 2.3, the radiated power is $3-4\,\mathrm{kW}$. The Thomson scattering profiles do not change even with large changes in radiated power, indicating that most of the power is radiated in the plasma periphery. A bolometer viewing $r/a \lesssim 0.6$ only measures

 $\approx 1\,\mathrm{kW}$, but most of this power is due to looking through the edge plasma. Particle transport calculations in previous studies estimate that ionization accounts for $\approx 1\,\mathrm{kW}$ within $r/a \lesssim 0.6$. Collisions between electrons and ions transfer energy calculated as 5

$$P^{\rm e/i} = \frac{3}{2} n_{\rm e} \frac{dT_{\rm e}}{dt} = -\nu_{\epsilon}^{\rm e/i} n_{\rm e} (T_{\rm e} - T_{\rm i}) ,$$
 (2.7a)

$$\nu_{\epsilon}^{e/i} = \frac{4}{\sqrt{\pi}} \frac{4\pi n_{i} Z_{i}^{2} e^{4} \ln \Lambda}{(4\pi\epsilon_{0})^{2} m_{e} m_{i} v_{Tei}^{3}},$$
(2.7b)

$$v_{Tei} = \sqrt{\frac{2T_{\rm e}}{m_{\rm e}} + \frac{2T_{\rm i}}{m_{\rm i}}}$$
, (2.7c)

$$\ln \Lambda \cong \ln \left(\frac{12\pi n_{\mathrm{e}} \lambda_{\mathrm{De}}^{3}}{Z_{\mathrm{i}}} \right)$$
 , (2.7d)

where (Z_ie) is the ion charge, $\ln \Lambda$ is the coulomb logarithm, and $\lambda_{\rm De}$ is the electron Debye length. For 50 eV ions with $Z_{\rm i}=1$, the power to ions is $\approx 1\,{\rm kW}$ within r/a<0.6. These energy losses are on the order of the uncertainty of the measured $P_{\rm abs}$ and are ignored here. Ray-tracing calculations in Figure 2.4 show that power deposition from ECRH takes place entirely within $r/a\lesssim0.3$, but ray-tracing is not executed for every profile. For the analysis in this section, an approximate ray-tracing calculation is scaled to match the measured absorbed power in the experiment. By calculating the heat flux outside the power deposition region for gradient scans, the numerator is the total absorbed power $P_{\rm abs}$, and the heat flux is

$$Q_{\rm e} = \frac{P_{\rm abs}}{V' \langle |\nabla \rho| \rangle} \ . \tag{2.8}$$

while the geometric terms come from calculations of the vacuum magnetic geometry.

The heat flux Q is the power passing through a surface, and the geometry terms $\langle |\nabla V| \rangle = V' \langle |\nabla \rho| \rangle$ calculate the flux surface area. While $V = V(\rho)$ is used in Equation (2.4) to aid comparison to experimental profiles in r/a, the volume can be parametrized as $V = V(\psi)$, where ψ is the toroidal flux and is related to ρ by Equation (2.1). Then,

$$\langle |\nabla V| \rangle = \frac{\partial V}{\partial \psi} \langle |\nabla \psi| \rangle . \tag{2.9}$$

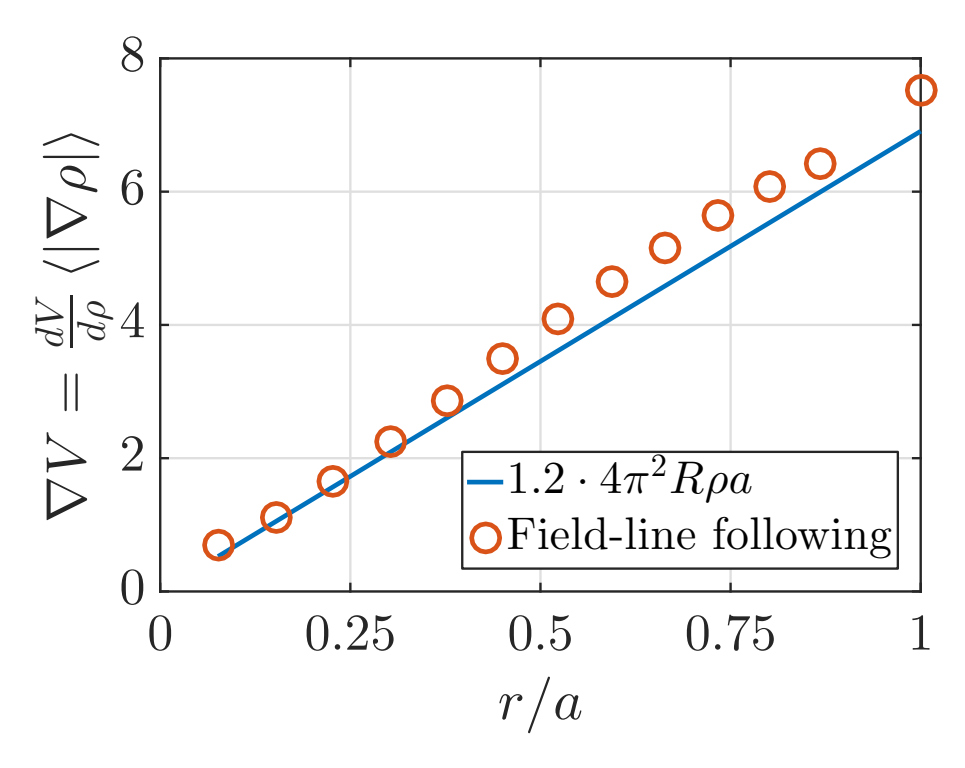


Figure 2.5: Comparison of $V'\langle |\nabla \rho| \rangle$ from a large-aspect-ratio torus geometric estimate to the calculation by field-line following in the QHS geometry.

Equation (2.4) would then be integrated over ψ instead of ρ . However, this study only addresses the heat flux outside the ECRH deposition region and the integration is trivial for either variable. The terms on the right-hand side of Equation (2.9) can be solved numerically ¹³ by integrating along a field line, such as

$$\frac{dV}{d\psi} = \lim_{N \to \infty} \frac{1}{N} \int \frac{dl}{B} , \qquad (2.10)$$

where N is the number of toroidal transits along a field line. ^{14,15} Previous work ^{2,16} used estimates of the geometric terms without clearly identifying their source. Using a large-aspect-ratio torus approximation, the area A of a flux surface is $A=2\pi r\cdot 2\pi R=4\pi^2Rr$, where R is the major radius. The volume is $V=\pi r^2\cdot 2\pi R=2\pi^2Rr^2$. Using $\rho=r/a$ and taking the derivative with respect to ρ , one obtains $dV/d\rho=4\pi^2R\rho a^2$. Assuming axisymmetric circular flux surfaces, $\rho=r/a$, and it follows that $\langle |\nabla \rho| \rangle=1/a$. In HSX,

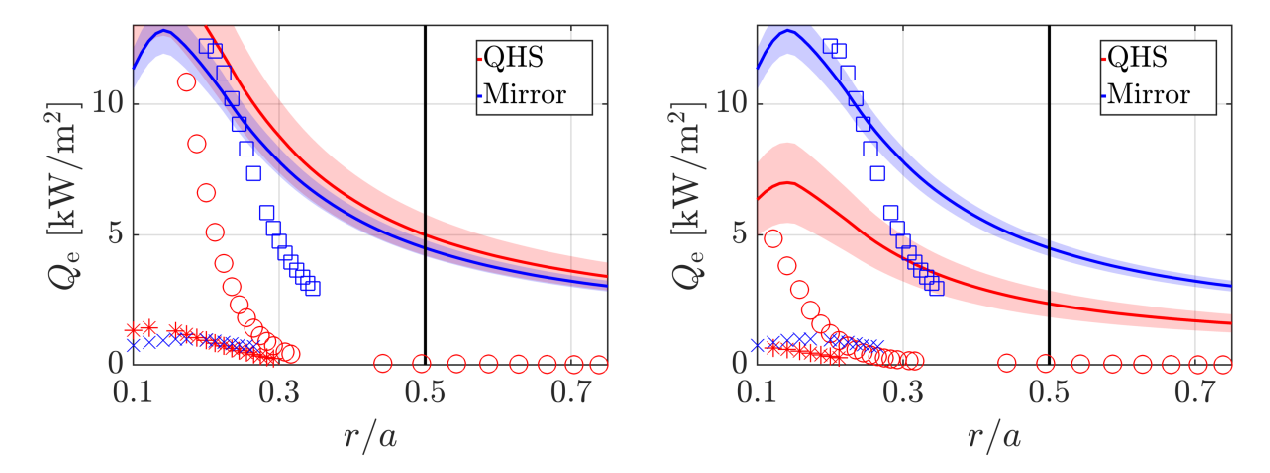


Figure 2.6: The heat flux (lines) for profiles with the same $P_{\rm abs}$ (left, from Figure 2.1) and matched profiles (right, from Figure 2.3) compared to neoclassical calculations. The indicated uncertainty in $Q_{\rm e}$ is solely due to uncertainty in $P_{\rm abs}$. In neoclassical calculations, two ambipolar roots exist in the core: the ion root (circles in QHS, squares in Mirror), and the electron root (stars in QHS, crosses in Mirror). When $P_{\rm abs}$ is the same, a/L_n is larger in QHS. When profiles and gradients are matched, the heat flux is smaller in QHS.

there is a factor of 1.2 to account for the helical excursion of the magnetic axis. ¹⁵ These values are compared to vacuum magnetic calculations for QHS in Figure 2.5. Actual values from field-line following at r/a=0.5 are $V'\langle|\nabla\rho|\rangle=3.898$ in QHS and $V'\langle|\nabla\rho|\rangle=3.801$ in Mirror.

Typical QHS profiles have higher core temperatures and steeper mid-radius density gradients than comparable Mirror plasmas, as in Figure 2.1. The TEM is driven by temperature and density gradients, and a comparative study in the QHS and Mirror configurations should match normalized gradients to avoid a difference in free energy of the gradient drive. Such matched profiles were presented in Figure 2.3. The heat flux for both these profiles is plotted in Figure 2.6, along with calculations of neoclassical transport. As the heat flux in Equation (2.8) only depends on a measurement of the absorbed power, the uncertainty is relatively small and $Q_{\rm e}$ is clearly larger in the Mirror configuration when profiles are matched. The difference in $V'\langle|\nabla\rho|\rangle$ between configurations is small, and so this is due to a difference in $P_{\rm abs}$. Less power is required to sustain the same profile in

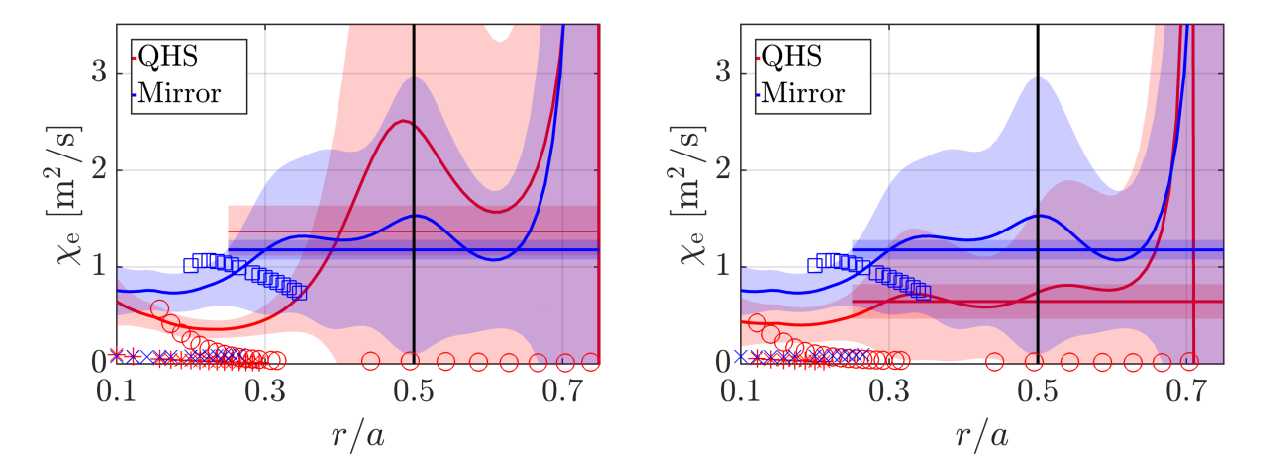


Figure 2.7: The thermal diffusivity for profiles with the same $P_{\rm abs}$ (left, from Figure 2.1) and matched profiles (right, from Figure 2.3) compared to neoclassical calculations. Profiles are fit by GPR (not straight) and the linear fit at r/a=0.5 (straight line). The indicated uncertainty in $\chi_{\rm e}$ is due predominantly due to uncertainty in $a/L_{\rm Te}$. Symbols are defined as in Figure 2.6. While the thermal diffusivity is larger in Mirror at r/a=0.5 in the right panel, differences are well within the uncertainty of the GPR fit. Changes in the diffusivity follow the change in heat flux.

the QHS configuration as in Mirror. Inside $r/a \lesssim 0.3$, the heat flux is reduced in the QHS configuration, illustrating reduced neoclassical transport. This region has been investigated thoroughly in earlier work, 1,2,5,17 and is not the focus of the present study.

Neoclassical transport is calculated by PENTA² and plotted as symbols in Figure 2.6. PENTA uses the monoenergetic transport coefficients calculated by DKES to solve for particle fluxes as a function of the radial electric field. The electric field is determined using the ambipolarity constraint that the ion and electron fluxes are equal. This may yield one or more roots of the equation that satisfy the constraint. Typically, there may be an ion root that corresponds to a negative or small positive electric field, a large positive electric field called an electron root and a third unstable root between them. The particular value of the electric field that satisfies the ambipolarity constraint is then used to determine the heat flux. The ion root (circles in QHS, squares in Mirror) is present across most of the minor radius, and approaches the experimental heat flux in the core. Deeper in the core, there is

an electron root (stars in QHS, crosses in Mirror) that drives very little flux. A possible transition to the electron root in the core has been associated with an internal transport barrier and peaked temperature profiles at HSX. ¹⁸ Outside $r/a \gtrsim 0.3$, the experimental heat flux is much larger than the neoclassical heat flux. Neoclassical calculations are missing for the Mirror configuration for $0.4 \le r/a \le 0.8$, but the heat flux is already small and trending downward at r/a = 0.35 and cannot account for the difference between the QHS and Mirror configurations. The thermal diffusivity for the profiles in Figure 2.3 is plotted in Figure 2.7. While the heat flux only involves the uncertainty in the absorbed power, the thermal diffusivity also depends on the density and the temperature gradients. This introduces a very large uncertainty to the thermal diffusivity. The difference in transport between QHS and Mirror at $r/a \approx 0.2$ is robust, but any difference at $r/a \approx 0.5$ is within the uncertainty due to the GPR fit. The localized linear fit minimizes this uncertainty and provides a good estimate of the thermal diffusivity at the mid-radius.

The difference between the experimental and neoclassical heat flux is the anomalous heat flux, expected to be turbulent heat flux driven by the TEM, as discussed in detail in Chapter 3. While the temperature gradient peaks in the core, the anomalous flux is larger at the mid-radius where the density gradient is largest. This supports the idea that the TEM is primarily driven by the density gradient in HSX. The neoclassical transport provides a very small contribution to the overall thermal transport at r/a = 0.5, and performing neoclassical calculations for every profile would constitute a highly inefficient approach. Therefore, neoclassical transport will be ignored in this study.

Scaling of heat flux with driving gradients

Energy transport analysis of a single profile in Figures 2.6 and 2.7 shows that the heat flux and thermal diffusivity are larger in the Mirror configuration when profiles are matched. Analysis of multiple profiles describes the scaling of the thermal transport with driving

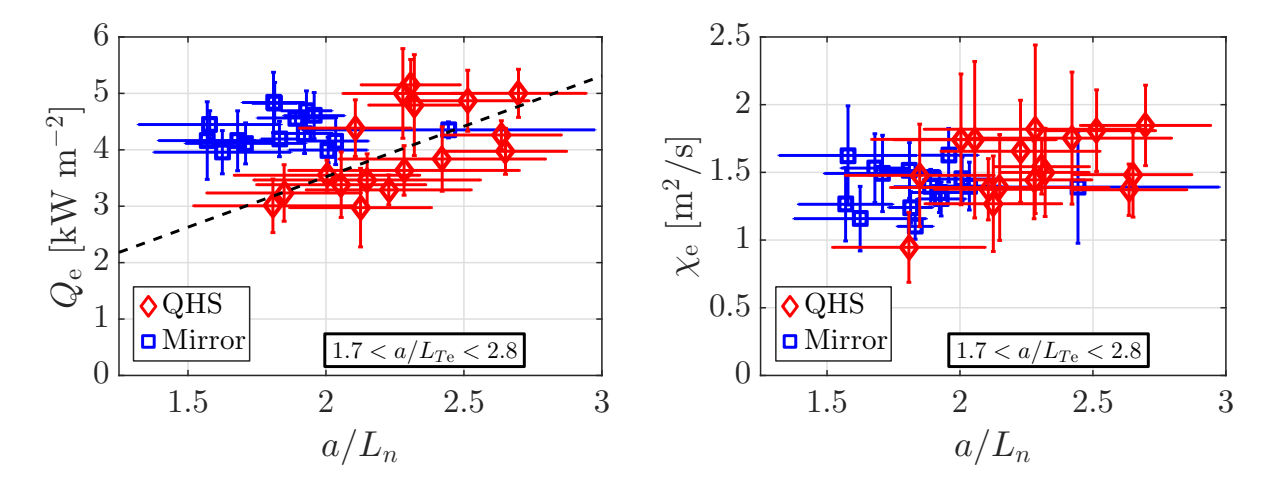


Figure 2.8: The scaling of the heat flux $Q_{\rm e}$ and thermal diffusivity $\chi_{\rm e}$ with density gradient a/L_n . A linear fit (dashed line) shows that the heat flux in QHS increases with a/L_n ($\Delta Q_{\rm e}/\Delta (a/L_n)=1.8$), but there is not enough Mirror data to determine a scaling. The heat flux is larger in the Mirror configuration at small gradients, but this difference does not appear in $\chi_{\rm e}$, primarily due to the larger density $n_{\rm e}$ in Mirror profiles to match a/L_n .

gradients, and will be compared to simulation in Chapter 3. Here, the profile database is filtered to find similar plasma profiles across a range of density or temperature gradients. In effect, one gradient can be scanned while holding the other approximately constant. While the uncertainty in a/L_n , a/L_{Te} , $Q_{\rm e}$, and $\chi_{\rm e}$ is large for an individual profile, this analysis can capture the gross trend. A linear fit to profiles at the mid-radius is not always a good approximation. This is apparent when the uncertainty of a/L_n or a/L_{Te} is very large, and profiles with large gradient uncertainties $\delta(a/L)>2$ are removed. The stored energy measurement is complicated by large signal oscillations that sometimes contaminate the result. This appears as a large uncertainty in the absorbed power for the collection of shots that compose a profile, and those profiles are also removed. Filters on the electron temperature and power-per-particle $P_{\rm abs}/n_{\rm e}$ isolate a cluster of similar profiles.

A scan of the density gradient is shown in Figure 2.8. Profiles have been selected for $1.7 < a/L_{Te} < 2.8$, which is about equal to the typical uncertainty in a/L_{Te} . There is not enough data to determine a scaling in Mirror, but the heat flux in QHS increases from 3 kW

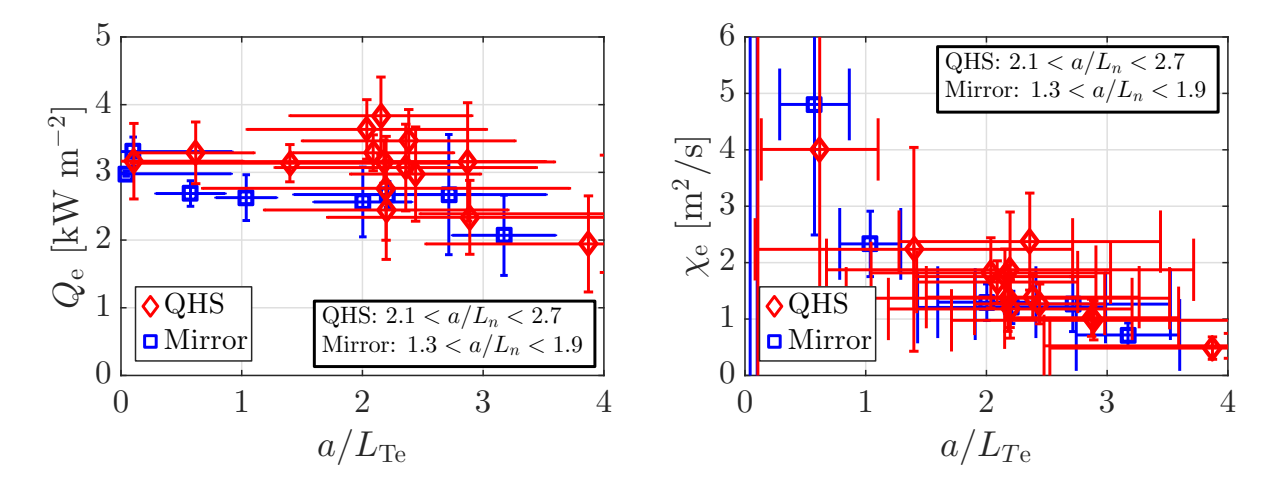


Figure 2.9: The scaling of the heat flux $Q_{\rm e}$ and thermal diffusivity $\chi_{\rm e}$ with temperature gradient $a/L_{T\rm e}$. Different filters on a/L_n are used in the QHS and Mirror configurations due to the profile distribution in Figure 2.2. The heat flux in both configurations is nearly independent of $a/L_{T\rm e}$. The heat flux is similar in the QHS and Mirror configurations, despite smaller density gradients in the Mirror configuration. The diffusivity demonstrates the expected $1/\nabla T_{\rm e}$ dependence in Equation (2.6).

to $5\,\mathrm{kW}$ across a change in a/L_n of 0.5. While a diffusive heat flux is related to ∇T_e , the flux can be driven by an instability destabilized by the density gradient. Where Mirror data is available, Q_e is larger than in the QHS configuration. However, in χ_e , this is compensated by the larger density, and there is no significant difference in diffusivity between QHS and Mirror. A similar scan of the temperature gradient is shown in Figure 2.9. Mirror profiles are generally distributed at lower density gradient, as seen in Figure 2.2, and so different gradient filters were used for the QHS and Mirror profiles. For these filters, the heat flux is similar in QHS and Mirror, despite a significantly smaller density gradient in the Mirror profiles. This indicates that the difference between QHS and Mirror in Figure 2.8 applies to the broader profile database. In both configurations, the heat flux is roughly independent of the temperature gradient. Together, the scaling with density gradient and lack of scaling with temperature gradient, is indicative of predominantly ∇n -driven turbulence.

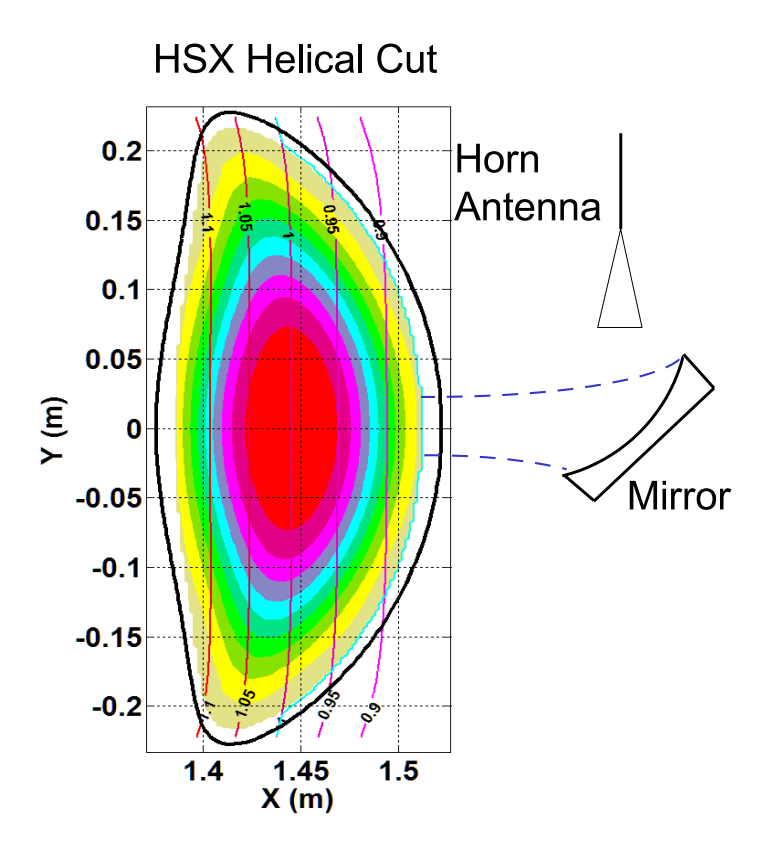


Figure 2.10: A schematic of the reflectometer from Reference 20. The horn antenna acts as both transmitter and receiver for the probe beam. A mirror at the midplane directs the probe beam toward the plasma on the outboard side of the bean cross section. Filled contours show flux surfaces, while labeled contours indicate the magnetic field.

2.3 Density fluctuation measurements from reflectometry

The heat flux presented in Section 2.2 demonstrates the global trend of energy transport in the QHS and F14 Mirror configurations. This section analyzes density fluctuations amplitudes, a measurement related directly to the underlying turbulence. These measurements come from a reflectometer installed and operated on HSX by K.M. Likin for the purpose of measuring fluctuations. ¹⁹ Measurements with this diagnostic are localized to the steep-density-gradient area, matching the region of the plasma most unstable to the ∇n -driven TEM.

Reflectometry operates by directing a probe microwave beam into the plasma at a

frequency below the cutoff frequency. The probe beam at HSX is ordinary-wave polarized, and the cutoff frequency for the ordinary wave is the plasma frequency

$$\omega_{\rm p} = \sqrt{\frac{n_{\rm e}e^2}{m_{\rm e}\epsilon_0}} \,. \tag{2.11}$$

The cutoff frequency depends on density, and so we can define a cutoff density

$$n_{\rm c} = \omega_{\rm b}^2 m_{\rm e} \epsilon_0 / e^2 \,, \tag{2.12}$$

where the plasma frequency is equal to a given probe beam frequency $\omega_{\rm b}$. Here, ϵ_0 is the permittivity of free space. At the radial location of the cutoff density, the probing beam is modulated by density fluctuations and reflected back to a receiving antenna, where the phase and power of the reflected beam are measured. The temporal response of the reflected beam provides information on the fluctuations at that location. Frequency steps of the probing beam match different cutoff densities, providing an effective way to scan measurements across the plasma density profile. In some systems, the phase delay in the probe beam is measured to provide the density profile itself. However, the HSX reflectometer is designed for high time resolution (1 MHz) for the measurement of turbulence, and phase jumps at frequency steps make profile measurements difficult. Instead, a density profile from Thomson scattering provides the radial location of the cutoff location. ¹⁹ Typical operation scans the probe beam frequency in steps across $15-26\,\mathrm{GHz}$ ($n_{\rm c} \approx 3.5-8 \times 10^{12}\,\mathrm{cm}^{-3}$).

The HSX reflectometer is mounted at the midplane on the outer wall of the bean-shaped cross section, as shown in Figure 2.10. As will be discussed in Chapter 3, simulations use a local flux tube geometry that does not cover an entire flux surface. However, the flux tube is centered on the outboard midplane of the bean-shaped cross section, directly on the line-of-sight of the HSX reflectometer. The probe beam has a diameter of 8 cm and measures fluctuations in the range $0.2 \lesssim k_\perp \rho_{\rm s} \lesssim 1$.

Analysis of fluctuations in reflectometry

Reflectometry provides the required location, resolution, and wavenumber sensitivity to measure the TEM, but measurements of density fluctuations must contend with the complexities of microwave beam reflection and refraction in a plasma. Fluctuations of the phase of the reflected beam are interpreted as radial fluctuations of the cutoff layer, but diagnostic geometry, plasma profiles, and fluctuation characteristics can all affect the measurement. In the simplest interpretation, fluctuations of the phase of the reflected beam are linearly related to density fluctuations at the cutoff layer. However, the microwave beam may encounter significant refraction before reaching the cutoff layer, spreading beam power and expanding the volume of the reflection layer. If fluctuations are of large enough amplitude, the specular reflection of the microwave beam may not be directed back to the receiving antenna and the reflectometer is measuring a higher-order reflection. These effects can break down the linear relationship, and fluctuations of the beam phase will saturate and decouple from the density fluctuations of the cutoff layer. Full-wave simulations of microwave propagation through a turbulent plasma can show when measurements enter this nonlinear regime. 21 When they do, it manifests as a saturation of the reflected beam fluctuations despite increasing density fluctuations.

If density fluctuations are large enough that the relationship between fluctuations and reflectometry measurements is nonlinear, the standard deviation of the reflected power would be comparable to the total reflected power as the specular reflection wanders across the antenna. In addition, the measured phase would be evenly distributed between $-\pi$ and π . As seen in Figure 2.11, HSX measurements do not show either of these indicators of saturated reflectometry measurements. There is also a nonlinearity parameter γ to estimate when measurements are in this nonlinear regime. ²² Significant nonlinear effects

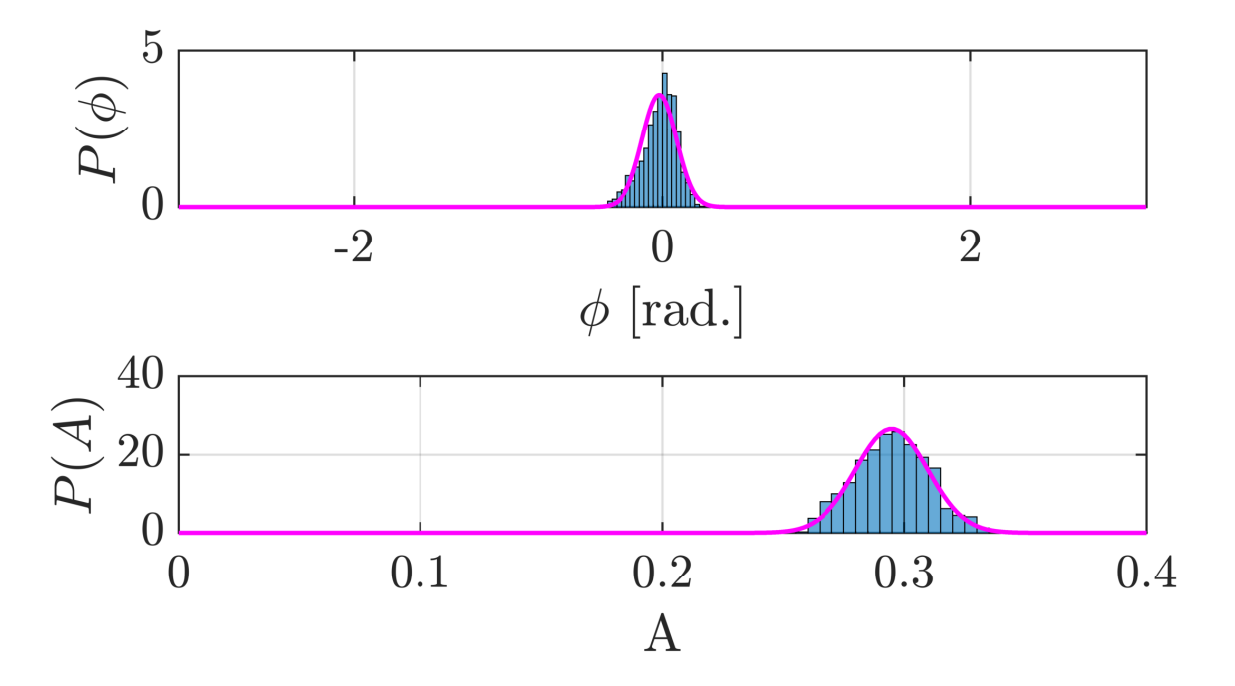


Figure 2.11: The probability density of the phase and amplitude of the probe beam. Blue bars are a histogram of experimental data, and the magenta line is a normal distribution fit. Beam power fluctuations are significantly smaller than the total beam power, and phase fluctuations are narrowly distributed about $\phi=0$, indicating that fluctuations are not too large for a linear interpretation.

are expected when $\gamma > 1$. The nonlinearity parameter is 23

$$\gamma = \left(\frac{\delta n}{n}\right)^2 \frac{G^2 \omega_b^2 x_c l_{cx}}{c^2} \ln \frac{x_c}{l_{cx}} , \qquad (2.13)$$

where G=1 in the ordinary mode polarization, $x_{\rm c}$ is the distance traveled inside the plasma to the cutoff layer, $l_{\rm cx}$ is the turbulent radial correlation length, and c is the speed of light. For measurements at r/a=0.5 with the HSX reflectometer, $\omega_{\rm b}=2\pi f=2\pi\cdot 19\,{\rm GHz}$ and $x_{\rm c}=6\,{\rm cm}$. The density fluctuation amplitude and radial correlation length must be estimated, such as from simulations in Chapter 3. We use conservative estimates of $\delta n/n\approx 0.05$ and $l_{\rm cx}\approx 0.015\,{\rm m}$. Density fluctuations from simulations in Chapter 3 predict amplitudes around 2%, and measurements at r/a=0.8 find that $l_{\rm cx}=\approx 1.5\,{\rm cm}$ at low density and decreases with increasing density. This gives a nonlinearity parameter $\gamma\approx 0.5$;

hence the fluctuation amplitude should be linearly related to fluctuations in the reflected beam.

At small amplitude, density fluctuations are directly related to fluctuations of the measured phase by 24

$$\phi_{\rm sd} = \frac{4\pi\sigma}{\lambda} \frac{\cos\theta_1}{\sqrt{2}} \left(\frac{k_{\rm w}w}{2\pi}\right)^{-0.6} . \tag{2.14}$$

Here, $\phi_{\rm sd}$ is the standard deviation of the measurement of the phase, σ/λ is the radial dimension of fluctuations normalized to the wavelength of the probe beam, θ_1 is the incident angle of the probe beam, $k_{\rm w}$ is the spectral half-width of the fluctuations and w is the beam radius. For a normal-incident probe beam, as in HSX, $\theta_1=0$. The spectral half-width assumes a Gaussian distribution with respect to fluctuation wavenumbers, and simulations in Chapter 3 estimate $k_w\approx 1/\rho_{\rm s}$. While $\phi_{\rm sd}$ is measured in the experiment, fluctuations are normalized as \tilde{n}/n for comparison to simulated turbulence, which is determined from the amplitude of fluctuations σ by 25

$$\frac{\delta n}{n} \approx \left. \frac{\sigma}{n} \frac{dn}{dr} \right|_{n=n_c}$$
 (2.15)

By rearranging Equation (2.14), the normalized density fluctuations measured by the HSX reflectometer can be written as a function of the measurements of the density gradient and the standard deviation of the reflectometer phase as

$$\frac{\delta n}{n} \approx \left[\frac{\lambda \sqrt{2}}{4\pi a} \left(\frac{k_{\rm w} w}{2\pi} \right)^{0.6} \right] \phi_{\rm sd} \left(\frac{1}{n} \frac{dn}{d\rho} \right) \bigg|_{n=n_{\rm c}} \approx 0.0464 \phi_{\rm sd} \left(\frac{1}{n} \frac{dn}{d\rho} \right) \bigg|_{n=n_{\rm c}} . \tag{2.16}$$

Scaling of density fluctuations with driving gradients

Thanks to K.M. Likin, a subset of profiles in the database have reflectometry measurements available, although the limited number of profiles does not enable a scan of one gradient with the other gradient fixed, as in Section 2.2. The gradients of the QHS and Mirror profiles that are available overlap very little. The entirety of this subset of profiles is used for the scaling plotted in Figure 2.12. Density fluctuations increase with density gradient,

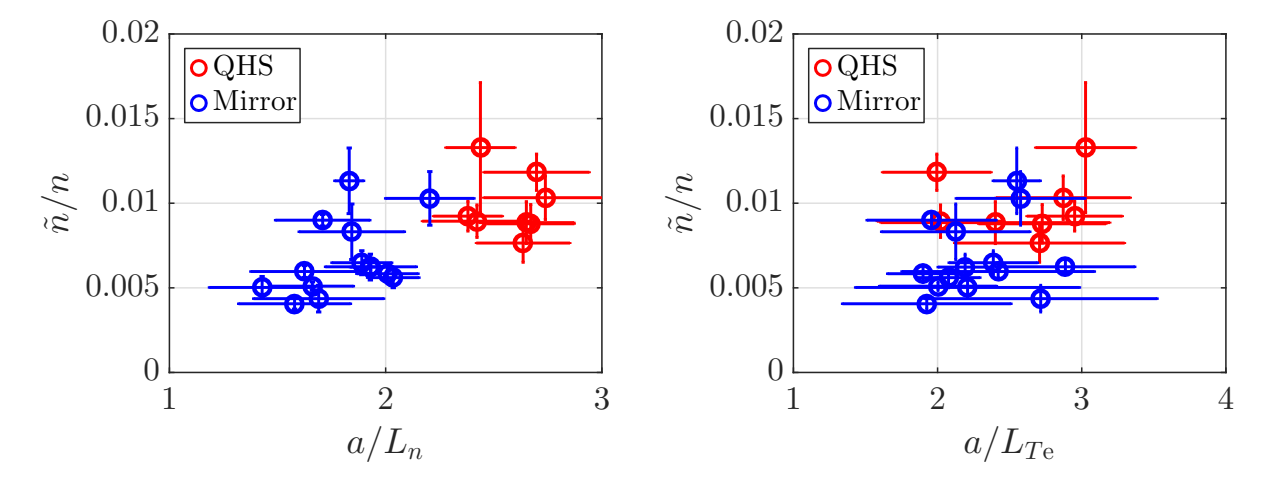


Figure 2.12: Density fluctuations increase with density gradient. There is insufficient data to compare the QHS and Mirror configurations, although a linear relationship between \tilde{n}/n and a/L_n would indicate that there is no difference between configurations. Density fluctuations show no dependence on the temperature gradient.

but have no relationship to the temperature gradient. This is consistent with fluctuations driven by an instability destabilized by the density gradient.

The density gradient is related to the background density, and both tend to increase together in experimental profiles. In Figure 2.13, density fluctuations also increase with the background density. Here, fluctuations are larger in the QHS configuration across the density range. This is explained in Figure 2.12 by the larger a/L_n in QHS. Therefore, density fluctuations depend on the normalized gradient, which tend to increase with the background density, rather than on the background density itself.

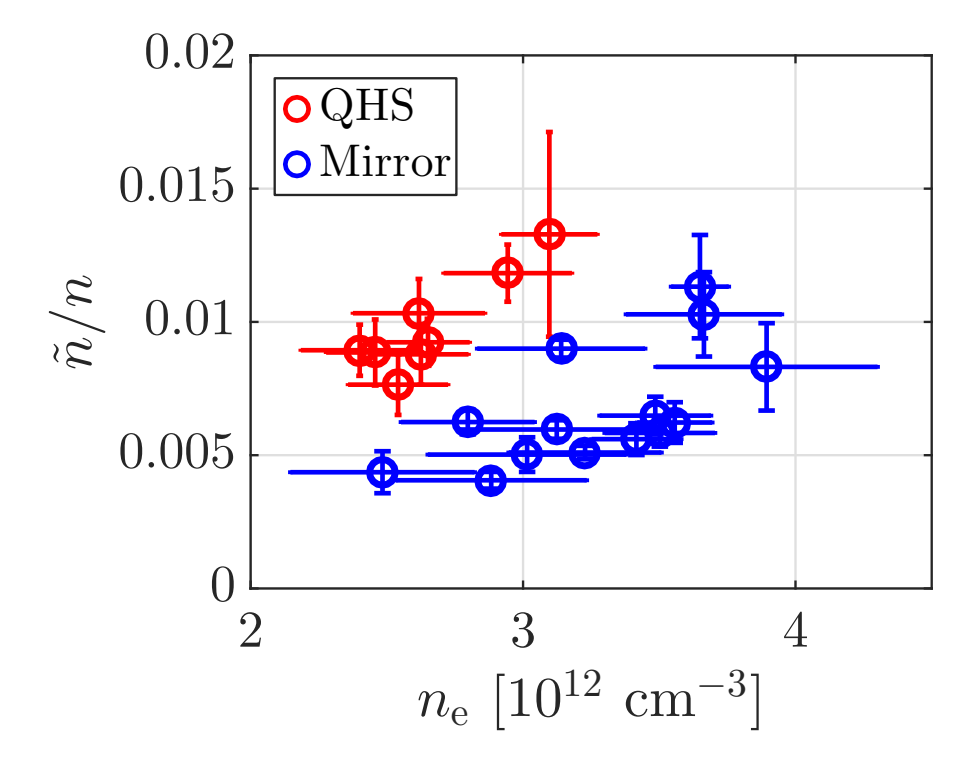


Figure 2.13: Density fluctuations increase with increasing background density $n_{\rm e}$. The QHS profiles have larger \tilde{n}/n , despite having similar or smaller density. This is explained in Figure 2.12 by the larger a/L_n .

2.4 Chapter Summary

This chapter has described the analysis of experimental profiles in the QHS and Mirror configurations targeting the physics of the trapped electron mode. In Section 2.1, a profile database was introduced to search archived experimental data for matching plasma discharges. This database allowed precise matching of plasma profiles in the QHS and Mirror configurations. In Section 2.2, energy balance was applied to this profile to show that, under matching gradient drive, the heat flux and diffusivity are larger in the Mirror configuration. This reduced analysis was then applied to subsets of the profile database to scan the driving gradients. It is shown that the heat flux increases with the density gradient but is independent of the temperature gradient. In Section 2.3, a linear model was used to interpret reflectometry measurements and derive the density fluctuation amplitude.

Density fluctuations are also shown to increase with the density gradient, but not the temperature gradient. These findings are consistent with an instability destabilized by the density gradient, such as the ∇n -driven TEM.

The experimental analysis in this chapter will be compared to simulations of TEM turbulence in Chapter 3. The stability of the TEM will be compared in the QHS and Mirror configurations, the measured heat flux will be compared to the simulated heat flux driven by TEM turbulence, and the qualitative scaling of the heat flux with driving gradients will be compared to gradient scans in simulations. The scaling and amplitude of density fluctuations will provide an additional point of comparison to simulation.

References

- [1] J. M. Canik, D. T. Anderson, F. S. B. Anderson, K. M. Likin, J. N. Talmadge, and K. Zhai, *Experimental demonstration of improved neoclassical transport with quasihelical symmetry*, Physical Review Letters **98**, 085002 (2007).
- [2] J. D. Lore, Measurement and Transport Modeling with Momentum Conservation of an Electron Internal Transport Barrier in HSX, Ph.D. thesis, The University of Wisconsin-Madison (2010).
- [3] C. B. Deng, D. L. Brower, D. T. Anderson, F. S. B. Anderson, A. Briesemeister, and K. M. Likin, *Core density turbulence in the HSX Stellarator*, Nuclear Fusion **55**, 123003 (2015).
- [4] J. M. Canik, Measurements of Reduced Neoclassical Particle and Electron Heat Transport with Quasisymmetry in the HSX Stellarator, Ph.D. thesis, The University of Wisconsin-Madison (2007).
- [5] W. A. Guttenfelder, Measurements and Modeling of Turbulent Transport in the HSX Stellarator, Ph.D. thesis, The University of Wisconsin-Madison (2008).
- [6] K. Zhai, F. S. B. Anderson, K. Willis, K. Likin, and D. T. Anderson, *Performance of the Thomson scattering diagnostic on Helical Symmetry Experiment*, Review of Scientific Instruments **75**, 3900 (2004).
- [7] M. A. Chilenski, M. Greenwald, Y. Marzouk, N. T. Howard, A. E. White, J. E. Rice, and J. R. Walk, *Improved profile fitting and quantification of uncertainty in experimental measurements of impurity transport coefficients using Gaussian process regression*, Nuclear Fusion **55**, 023012 (2015).
- [8] T. Nishizawa, M. Cavedon, R. Dux, F. Reimold, and U. von Toussaint, *Plasma parameter profile inference from limited data utilizing second-order derivative priors and physic-based constraints*, Physics of Plasmas **28**, 032504 (2021).
- [9] A. R. Briesemeister, Measurement and Modeling of the Flows and Radial Electric Field in the HSX Stellarator, Ph.D. thesis, The University of Wisconsin-Madison (2013).
- [10] W. Guttenfelder, J. Lore, D. T. Anderson, F. S. B. Anderson, J. M. Canik, W. Dorland, K. M. Likin, and J. N. Talmadge, *Effect of quasihelical symmetry on trapped-electron mode transport in the HSX stellarator*, Physical Review Letters **101**, 215002 (2008).
- [11] A. Briesemeister, K. Zhai, D. T. Anderson, F. S. B. Anderson, and J. N. Talmadge, *Comparison of the flows and radial electric field in the HSX stellarator to neoclassical calculations*, Plasma Physics and Controlled Fusion **55**, 014002 (2013).

- [12] S. T. A. Kumar, J. N. Talmadge, T. J. Dobbins, F. S. B. Anderson, K. M. Likin, and D. T. Anderson, *Determination of radial electric field from Pfirsch–Schlüter flows in the HSX stellarator*, Nuclear Fusion **57**, 036030 (2017).
- [13] V. V. Nemov, Calculations of the magnetic surface function gradient and associated quantities in a torsatron, Nuclear Fusion **28**, 1727 (1988).
- [14] W. D. D'haeseleer, W. N. G. Hitchon, J. D. Callen, and J. L. Shohet, *Flux Coordinates and Magnetic Field Structure* (Springer Berlin Heidelberg, Berlin, Heidelberg, 1991).
- [15] J. N. Talmadge and S. P. Gerhardt, *Numerical calculation of the Hamada basis vectors for three-dimensional toroidal magnetic configurations*, Physics of Plasmas **12**, 072513 (2005).
- [16] G. M. Weir, *Heat Transport Experiments on the HSX Stellarator*, Ph.D. thesis, The University of Wisconsin-Madison (2014).
- [17] G. M. Weir, B. J. Faber, K. M. Likin, J. N. Talmadge, D. T. Anderson, and F. S. B. Anderson, *Profile stiffness measurements in the Helically Symmetric experiment and comparison to nonlinear gyrokinetic calculations*, Physics of Plasmas **22**, 056107 (2015).
- [18] J. Lore, W. Guttenfelder, A. Briesemeister, D. T. Anderson, F. S. B. Anderson, C. B. Deng, K. M. Likin, D. A. Spong, J. N. Talmadge, and K. Zhai, *Internal electron transport barrier due to neoclassical ambipolarity in the Helically Symmetric Experiment*, Physics of Plasmas 17, 056101 (2010).
- [19] K. M. Likin, C. Lechte, H. Lu, and F. S. B. Anderson, ECE and reflectometry on the Helically Symmetric Experiment, in Proceedings of ITC/ISHW2007 (2007).
- [20] K. M. Likin, D. T. Anderson, F. S. B. Anderson, C. Deng, and J. N. Talmadge, *Frequency spectra of plasma density fluctuations in HSX*, 53rd APS Division of Plasma Physics Annual Meeting in Salt Lake City, UT, USA (2011).
- [21] C. Lechte, G. D. Conway, T. Görler, C. Tröster-Schmid, and the ASDEX Upgrade Team, *X mode Doppler reflectometry k-spectral measurements in ASDEX Upgrade: Experiments and simulations*, Plasma Physics and Controlled Fusion **59**, 075006 (2017).
- [22] E. Z. Gusakov and A. Y. Popov, *Non-linear theory of fluctuation reflectometry*, Plasma Physics and Controlled Fusion 44, 2327 (2002).
- [23] T. Happel, T. Görler, P. Hennequin, C. Lechte, M. Bernert, G. D. Conway, S. J. Freethy, C. Honoré, J. R. Pinzón, U. Stroth, and the ASDEX Upgrade Team, *Comparison of detailed experimental wavenumber spectra with gyrokinetic simulation aided by two-dimensional full-wave simulations*, Plasma Physics and Controlled Fusion **59**, 054009 (2017).
- [24] G. D. Conway, Effects of reflectometer asymmetries on fluctuation measurements, Plasma Physics and Controlled Fusion 41, 65 (1999).

[25] G. D. Conway, L. Schott, and A. Hirose, *Comparison of reflectometer fluctuation measure-ments from experiment and two-dimensional numerical simulation*, Review of Scientific Instruments **67**, 3861 (1996).

Gyrokinetic simulation of TEM turbulence in HSX

In Chapter 2, experimental measurements of the heat flux and density fluctuations targeted the peak density gradient, where the ∇n -driven TEM is expected to be the most unstable. However, those measurements describe overall turbulence in the experiment, and not the TEM instability directly. Simulations are required to attribute any difference in experimental measurements to TEM turbulence. This Chapter uses the Gene code, described in Section 3.1, for linear and nonlinear numerical investigations of TEMs in HSX geometry at experimental parameters. Linear calculations, which are used to obtain growth rate, frequency, and eigenmode structure, are significantly cheaper and the first point of comparison between configurations. Commonly, quasilinear mixing-length models are employed to approximate nonlinear fluxes through linear mode characteristics $(Q \sim \gamma/\langle k_{\perp}^2 \rangle)$. However, turbulence is defined by the random and coupled excitation of fluctuations over a broad range of scales. Nonlinear simulations include the coupling of energy between modes, energy is transferred from unstable to stable ones, and the turbulence reaches a quasi-stationary saturated state with a well-defined heat and particle flux. In particular, comparisons of the heat flux and density fluctuation amplitude to experimental measurements require simulations of saturated turbulence.

Previous nonlinear work³ focused on only the ∇n -driven TEM in the QHS configuration by using $a/L_{Te}=0$ and $T_{\rm i}/T_{\rm e}=1$. For comparison to that study, and to isolate

the effect of the density gradient drive in HSX, Section 3.2 uses these same parameters for the first comparison of nonlinear simulations in the QHS and Mirror configurations. Section 3.3 examines the effect of increasing a/L_{Te} and using an experimental temperature ratio $T_{\rm i}/T_{\rm e}\approx 0.2$. The first nonlinear simulations to be performed at experimental parameters are presented in Section 3.4 to enable direct comparison with the experiment. This section examines the dependence of linear growth rates and nonlinear heat flux on the driving gradients a/L_n and a/L_{Te} to match gradient scans in Chapter 2. Finally, the heat flux and density fluctuations from nonlinear simulations are compared to experimental measurements in Section 3.5.

3.1 Gyrokinetic simulation with Gene

The Gyrokinetic Electromagnetic Numerical Experiment code $(Gene)^4$ is used for calculations and simulations of the TEM in HSX. Gene is a gyrokinetic δf continuum code that solves the kinetic equation in realistic geometry. The kinetic equation describes the fundamental plasma dynamics as

$$\frac{d}{dt}F(\vec{x}, \vec{v}, t) = \left(\frac{\partial}{\partial t} + \vec{v} \cdot \frac{\partial}{\partial \vec{x}} + \frac{q}{m} \left(\vec{E} + \vec{v} \times \vec{B}\right) \cdot \frac{\partial}{\partial \vec{v}}\right) F(\vec{x}, \vec{v}, t) = \left.\frac{dF}{dt}\right|_{\text{collisions}} \tag{3.1}$$

where $F(\vec{x}, \vec{v}, t)$ is the distribution function that depends on position \vec{x} , velocity \vec{v} , and time t. For the standard perturbative approach, the distribution function is split into a background Maxwellian F_0 and a δf perturbation. The gyrokinetic formalism rewrites the Vlasov equation in gyrocenter coordinates and averages over the gyrophase, effectively approximating a particle orbiting a field line as a charged ring, but retaining finite Larmor radius effects important for short-wavelength turbulence. This assumes that the gyromotion of the particle is much faster than the turbulence dynamics, removing timescales on the order of the gyrofrequency and reducing the dimensionality of the problem by one. Gene

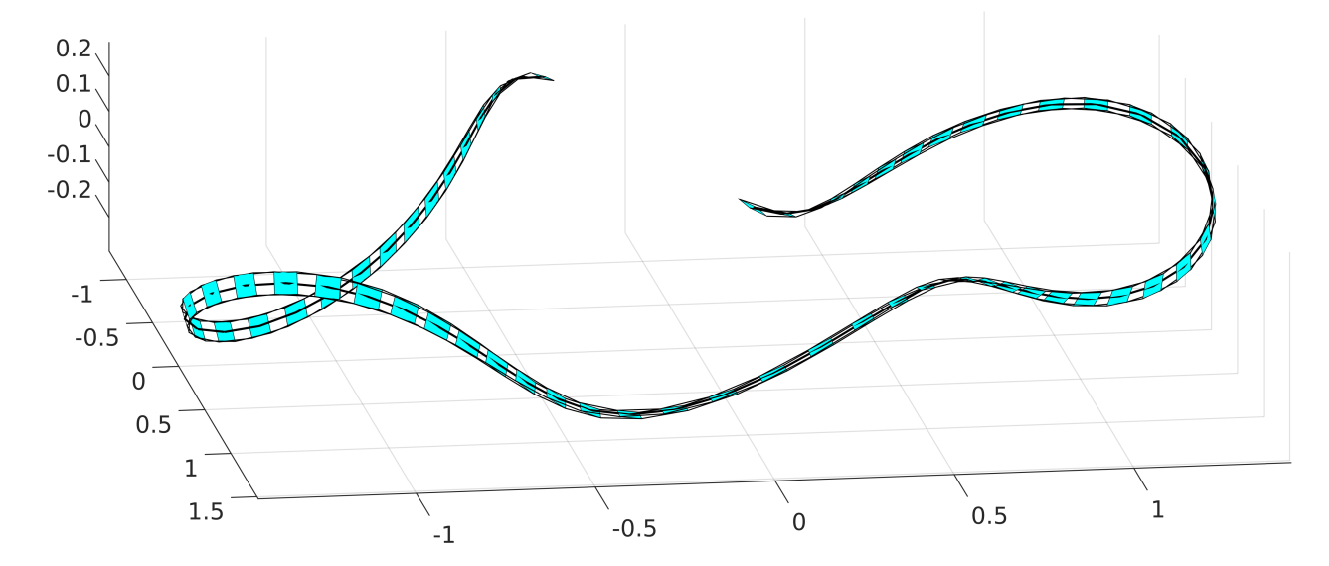


Figure 3.1: A representation of a flux tube in the QHS geometry with t=1.06. Slices in the x-y planes are plotted in blue. Black lines follow the field line in the center of the box, and connect the corners of the x-y planes. Flux tube coordinates are not orthogonal. In lab coordinates, the radial size of the box is small, and the y direction is nearly in the same direction as the field line z.

can be used to solve the linearized gyrokinetic Vlasov equation to describe individual eigenmodes, or for nonlinear simulations of, typically, quasi-stationary turbulence.

While the magnetic geometry can be specified for an entire plasma, the fine spatial and temporal scales for turbulence make a simulation of the full HSX plasma volume prohibitively expensive. Due to the fast parallel motion of particles, turbulence tends to exhibit highly anisotropic characteristics, and the domain can be reduced while retaining the relevant physics. In local simulations, the magnetic geometry is represented by a flux tube, calculated with the GIST code⁵ from VMEC equilibria.⁶ While equilibria typically depend on the plasma pressure, vacuum fields are used here, which is consistent with the very low plasma pressure in HSX. A flux tube is a reduced-geometry representation for toroidal magnetic geometries,⁷ and is constructed from a sheared box around a single field line identified by a field-line label in PEST⁸ coordinates as $\alpha = (\sqrt{s}/q) (q\theta^* - \phi)$, where s is the normalized toroidal flux, q = 1/t is the safety factor, ϕ is the toroidal angle, and θ^* is

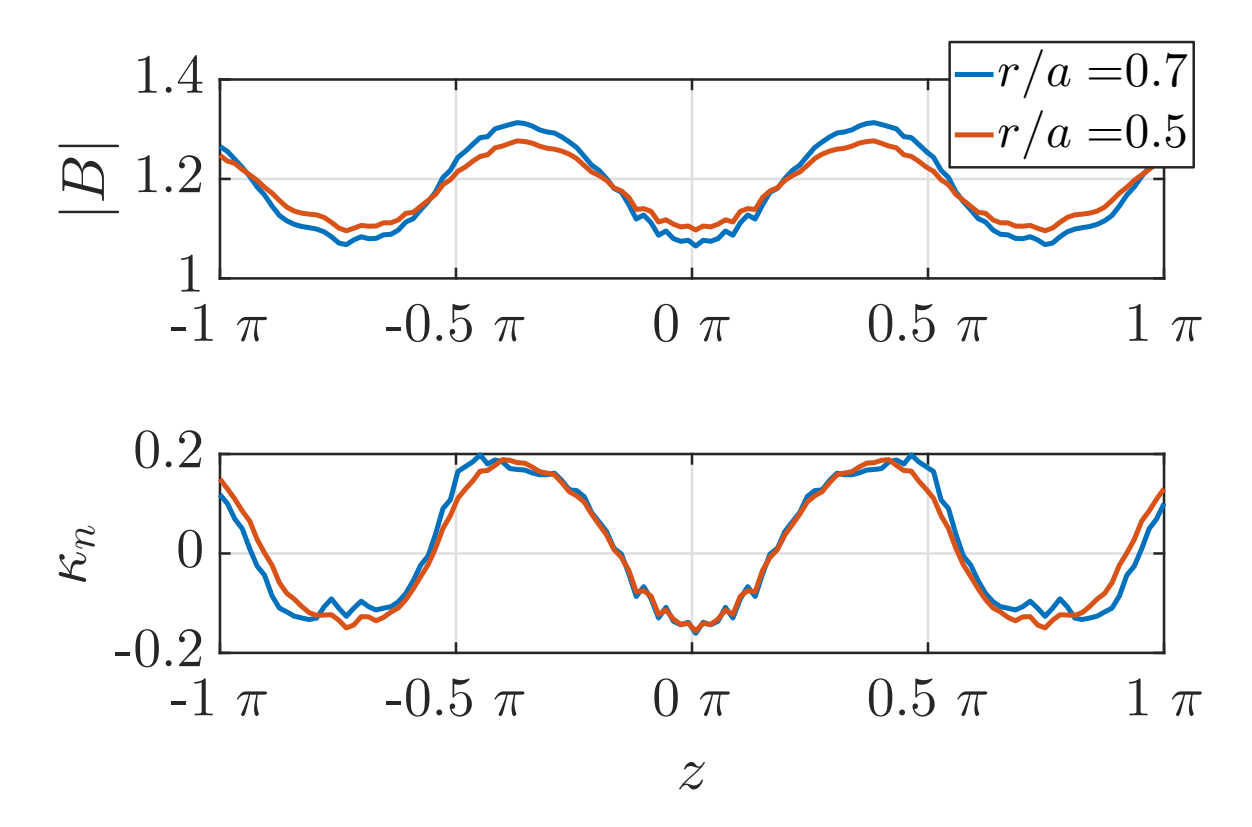


Figure 3.2: A comparison of the variation and curvature of the magnetic field at two radial locations. Due to the small global shear in HSX, changes in the magnetic geometry are relatively small across the minor radius.

the poloidal angle defined such that field lines are straight. An example flux tube in QHS geometry is plotted in Figure 3.1. The box uses non-orthogonal coordinates x in the radial direction, y in the flux surface, and z along the field line. In a Gene flux tube, a spectral representation is used for the x and y directions, while the quasi-periodic z direction is in real space. A local representation does not permit inclusion of the radial electric field, but only of radial electric field shear. While electric field shear can suppress turbulence, the ambipolar electric field in HSX is about $5\,\mathrm{kV/m}$ with little shear across the minor radius, $^{9-12}$ and is neglected in these simulations.

The radial box size of a flux tube is a function of the global shear through the "twist-and-shift" boundary condition as $l_x = N/(\hat{s}k_{y,\min}n_{\text{pol}})$, where \hat{s} is the global magnetic shear,

 $k_{y, \min}$ is the minimum y-wavenumber in simulation, $n_{\rm pol}$ is the parallel length of the flux tube in number of poloidal turns, and N determines the aspect ratio of the computational domain. In HSX, the global shear is very small, $\hat{s}\approx 0.05$ at $r/a\approx 0.7$, and simulations require large radial domains. For simulations here, the small shear also requires that flux tubes are extended to multiple poloidal turns, as discussed in References 13 and 14. However, the small shear in HSX suggests that differences of the magnetic geometry between surfaces are small. In order to mitigate the large resolutions required at r/a=0.5 where the shear is even smaller, and to facilitate comparison with previous work, a flux tube from the r/a=0.7 flux surface is used for simulations in this chapter. A comparison of the magnetic variation and curvature at r/a=0.5 and 0.7 is plotted in Figure 3.2.

In perfectly axisymmetric tokamaks, every flux tube on a given flux surface is identical. A single flux tube is generally expected to capture the physics on a given flux surface. Each flux tube in a stellarator is unique, and a local simulation will not always capture surfaceaveraged transport. However, Gene has been extended to include an entire flux surface, and quasi-stationary transport for the flux surface is generally found to lie between that of the highest and lowest transport tubes. ¹⁵ For HSX, the flux from different flux tubes converges as flux tubes are extended to four poloidal turns. Simulations here use the flux tube centered on the outboard midplane of the bean-shaped cross section ($\alpha = 0$), where the magnetictrapping and bad-curvature regions overlap. The flux tube is extended to four poloidal turns, and typical resolutions for nonlinear simulations use $N_x \times N_y \times N_z \times N_{v_{\parallel}} \times N_{\mu} =$ $128 \times 32 \times 256 \times 32 \times 8$ where x, y, and z are the spatial coordinates, v_{\parallel} is the velocity along the field line, and μ is the magnetic moment. Simulations here are collisionless and have kinetic ion and electron species. The ion temperature is small in HSX, with $T_{\rm i} < 70\,{\rm eV}$ across the plasma radius, and the gradient a/L_{Ti} is set to zero. The linear physics of the TEM can be modified by ion temperature gradients, but investigation of this effect is left to future work.

3.2 Comparison of the QHS and Mirror configurations

Evidence, both experimental 16 and numerical 17,18 , suggests that the ∇n drive of the TEM is more important than the $\nabla T_{\rm e}$ drive in HSX. The previous study 3 of nonlinear simulations of TEM turbulence in HSX artificially isolated the ∇n -driven TEM by eliminating the $\nabla T_{\rm e}$ drive with $a/L_{T\rm e}=0$ and $T_{\rm i}/T_{\rm e}=1$. This was motivated by the relatively flat electron temperature gradient outside $r/a\gtrsim 0.3$, while the density gradient peaks at $r/a\approx 0.6$. TEM simulations in the QHS configuration found that the nonlinear heat flux increased more quickly with the density gradient than would be expected from linear growth rates. A low- k_y peak in the heat flux was identified that could not be related to any unstable linear mode and which remains the subject of ongoing research. This peak exists in the Mirror configuration as well, and will be discussed at the end of Section 3.4. This section uses the same artificial parameters to compare ∇n -driven TEMs in QHS and Mirror, and contains the first comparison of nonlinear simulations between these configurations.

The Mirror configuration, introduced in Section 1.2, is expected to be more linearly stable to the TEM due to the reduced overlap of the trapped-particle regions and bad curvature. This is confirmed by linear growth rates γ in Figure 3.3. At $a/L_n=2$, the QHS configuration is more unstable for $k_y>0.7$. Eigenmodes have a potential structure extended along the field line that is categorically different between branches. Higher- k_y modes tend to have a narrower eigenfunction and follow the expected dependence on the overlap of the local trapped particle and bad curvature region. Low- k_y modes have a broader eigenfunction that is extended along the field line and insensitive to the individual trapped particle regions. There is no significant difference between the QHS and Mirror configurations at these small wavenumbers. However, at $a/L_n=4$, the TEM is more unstable in the QHS configuration for all k_y . Typically, the growth rate is a good indicator of transport in saturated turbulence, 19 and fluxes would be expected to be larger in the QHS configuration.

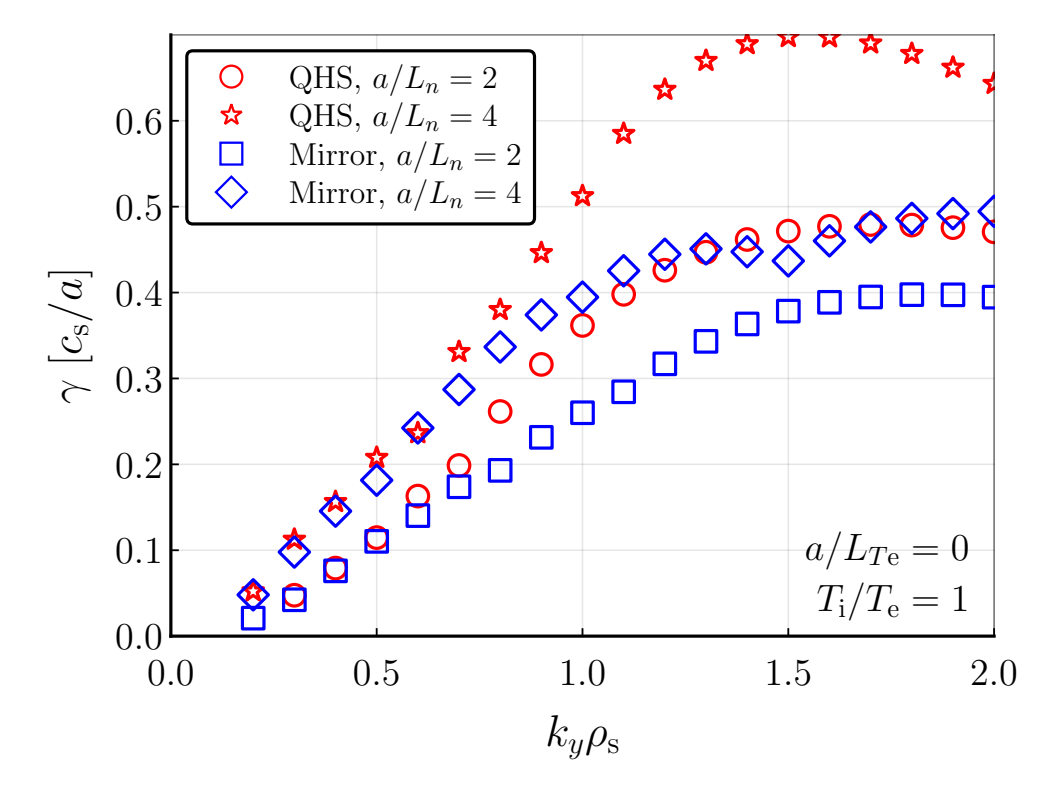


Figure 3.3: Linear growth rate spectra of the most unstable mode in the QHS and Mirror configurations for $a/L_{Te}=0$ and $T_{\rm i}/T_{\rm e}=1$ at two different density gradients. The QHS configuration is somewhat more unstable to the TEM, particularly at larger a/L_n , following the expected dependence on the overlap of trapped particle and bad curvature regions.

Nonlinear simulations tell a different story from the linear growth rates. The heat and particle fluxes in the QHS and Mirror configurations, presented in Figure 3.4, scale strongly with the density gradient in both the QHS and Mirror configurations. The turbulent particle flux Γ and heat flux Q depend on fluctuation amplitudes as

$$\Gamma = \langle \tilde{n}\tilde{v}_{Er} \rangle \; ; \quad Q = (3/2)\langle \tilde{p}\tilde{v}_{Er} \rangle \; .$$
 (3.2)

when magnetic fluctuations can be ignored.²⁰ Here, $\langle \cdot \rangle$ is an ensemble average, \tilde{n} is the fluctuating density, \tilde{p} is the fluctuating pressure, and \tilde{v}_{Er} is the radial $\vec{E} \times \vec{B}$ drift velocity due to potential fluctuations. Here, no difference is found in the dependence of the fluxes or the fluctuations on the gradient, and either flux is a good indicator of TEM turbulence activity. The heat flux is an easier quantity to determine from experimental measurements,

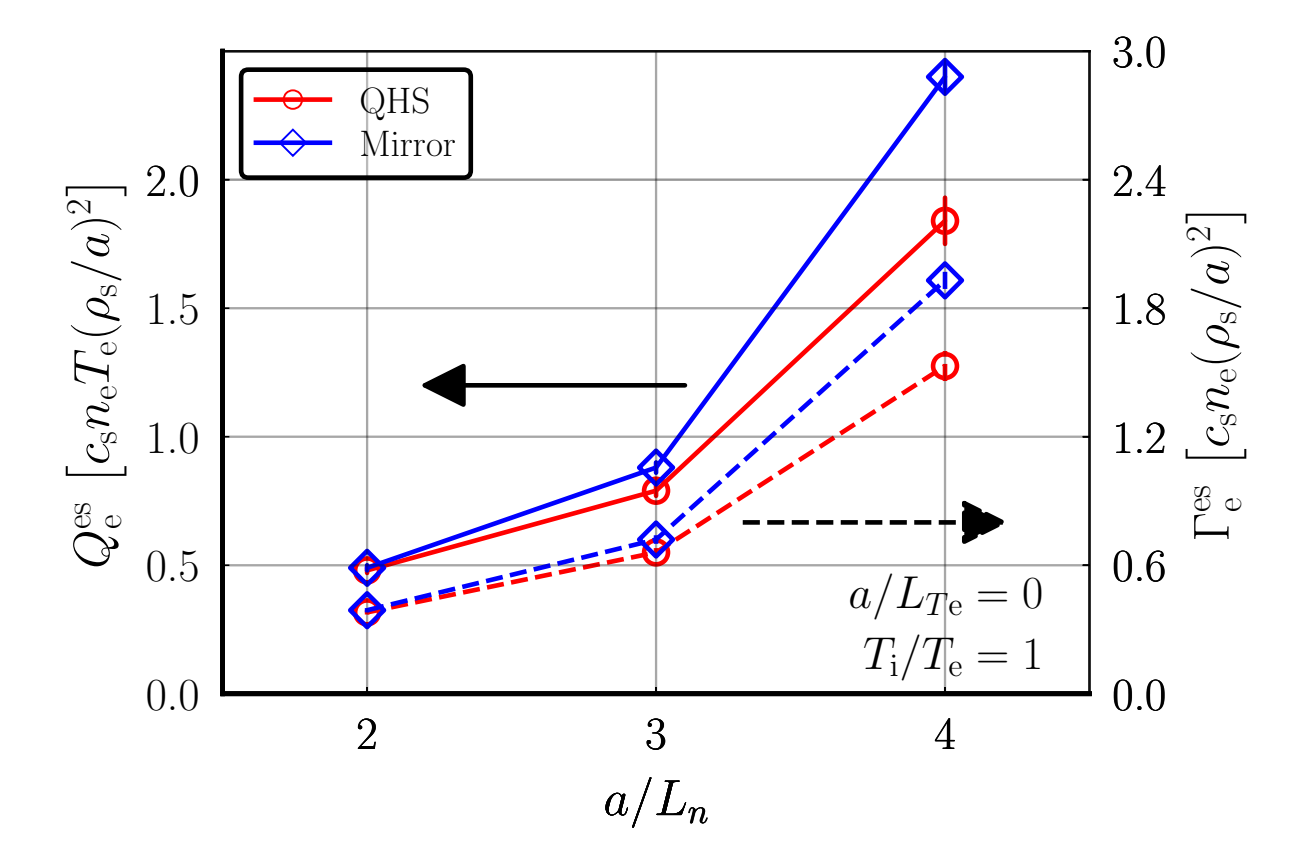


Figure 3.4: The heat flux (solid lines) and particle flux (dashed lines) from nonlinear TEM simulations increase strongly with a/L_n . Despite larger growth rates in the QHS configuration, both fluxes are slightly larger in the Mirror configuration. Statistical error bars of the flux in the quasi-stationary state are much smaller than the size of symbols plotted.

as energy deposition and power sinks are easier to determine that particle sourcing. Also in simulations, the particle flux can be a more difficult quantity to determine due to higher sensitivity to various simulation parameters, which leads to somewhat more sensitive convergence requirements.²¹ However, while growth rates are larger in the QHS configuration, both fluxes are larger in the Mirror configuration. Evidently the growth rate of the most unstable mode is not a good proxy for transport driven in saturated turbulence. The discrepancy between the linear expectation and the nonlinear transport could be due to other unstable but subdominant modes. It could also be due to a difference in the satura-

tion efficiency between the two configurations. The ∇n -driven TEM is known to saturate by transferring energy to stable modes through the zonal flow, and this motivated the investigation of collisionless zonal flow damping in Chapter 4. However, a full explanation of the increased transport in the Mirror configuration is beyond the scope of this study and left for future work.

3.3 Temperature effects on TEM simulations in HSX

While simulations with artificial parameters are important to reduce the complexity of a system and isolate targeted physics, comparisons to experiments require matching experimental parameters as much as possible. This section investigates how the TEM and quasi-stationary turbulence change when experimentally-relevant temperature effects are included in simulation.

In Chapter 2, and particularly Figure 2.2, it was shown that there is significant variation in the normalized density and temperature gradients. While fluctuations and heat transport point to the importance of the density gradient, it is not uncommon for the temperature gradient to actually be larger at $r/a \approx 0.5$ in experimental profiles. The TEM can be destabilized by either a/L_n or a/L_{Te} , and the mixed gradients in experiment indicate that either gradient could be the dominant drive. When a temperature gradient $a/L_{Te} = 2$ is included in linear calculations, as in the left panel of Figure 3.5, growth rates increase for all k_y . Additional gradient drive is added to the system, and the linear instability is further destabilized, while the peak growth rate shifts slightly to higher k_y . However, growth rates change in the same way for both the QHS and Mirror configurations, and do not predict any significant change to the comparison of configurations at $T_i/T_e = 1$.

Previous simulations have used unity temperature ratio $T_{\rm i}/T_{\rm e}=1$, but electron temperatures in HSX are much larger than ion temperatures. At $r/a\approx 0.5$, the electron temperature

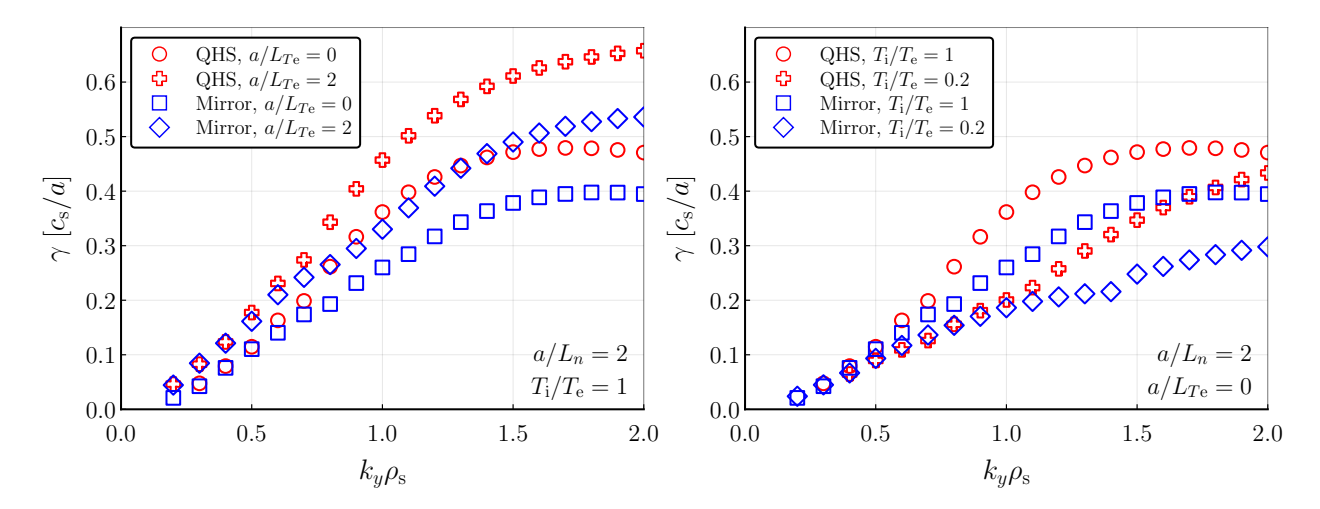


Figure 3.5: Spectra of linear growth rates of the most unstable mode in the QHS and Mirror configurations when $a/L_n=2$ and accounting for a/L_{Te} and non-unity $T_{\rm i}/T_{\rm e}$. The addition of a temperature gradient $a/L_{Te}=2$ increases growth rates for all k_y and shifts the peak growth rate slightly to higher k_y . Changing the temperature ratio to $T_{\rm i}/T_{\rm e}=0.2$ reduces growth rates for $k_y\rho_{\rm s}>0.5$, but also significantly reduces the difference between the Mirror and QHS configurations.

of most profiles is $200-250\,\mathrm{eV}$, while the ion temperature from CHERS measurements $^{9-12}$ is $40-70\,\mathrm{eV}$. Due to the lack of additional ion heating in HSX and the temperature dependence of electron-ion collisions, $\nu_{\mathrm{ei}} \propto 1/T^{3/2}$, lower electron temperatures are generally associated with hotter ions, and the maximum range of the temperature ratio is $0.15 \lesssim T_{\mathrm{i}}/T_{\mathrm{e}} \lesssim 0.35$. For this thesis, simulations use a baseline temperature ratio of $T_{\mathrm{i}}/T_{\mathrm{e}} = 0.2$ to represent the experiment. Linear calculations at this temperature ratio, on the right in Figure 3.5, show that growth rates are reduced in both configurations for $k_y \rho_s > 0.5$. However, growth rates are not reduced equally in the QHS and Mirror configurations. With a unity temperature ratio, growth rates are larger in the QHS configuration for $k_y \rho_s > 0.7$. When the ion temperature is reduced and $T_{\mathrm{i}}/T_{\mathrm{e}} = 0.2$, the divergence point between the QHS and Mirror growth rates shifts to $k_y \rho_s \approx 1.1$. Heat flux spectra in non-linear simulations for HSX generally peak at $0.8 \lesssim k_y \rho_s \lesssim 1$, and the range $0.7 < k_y \rho_s < 1.2$ covers a significant part of the wavenumbers most relevant to transport. These linear growth rates suggest that transport differences between the QHS and Mirror configurations would be reduced when

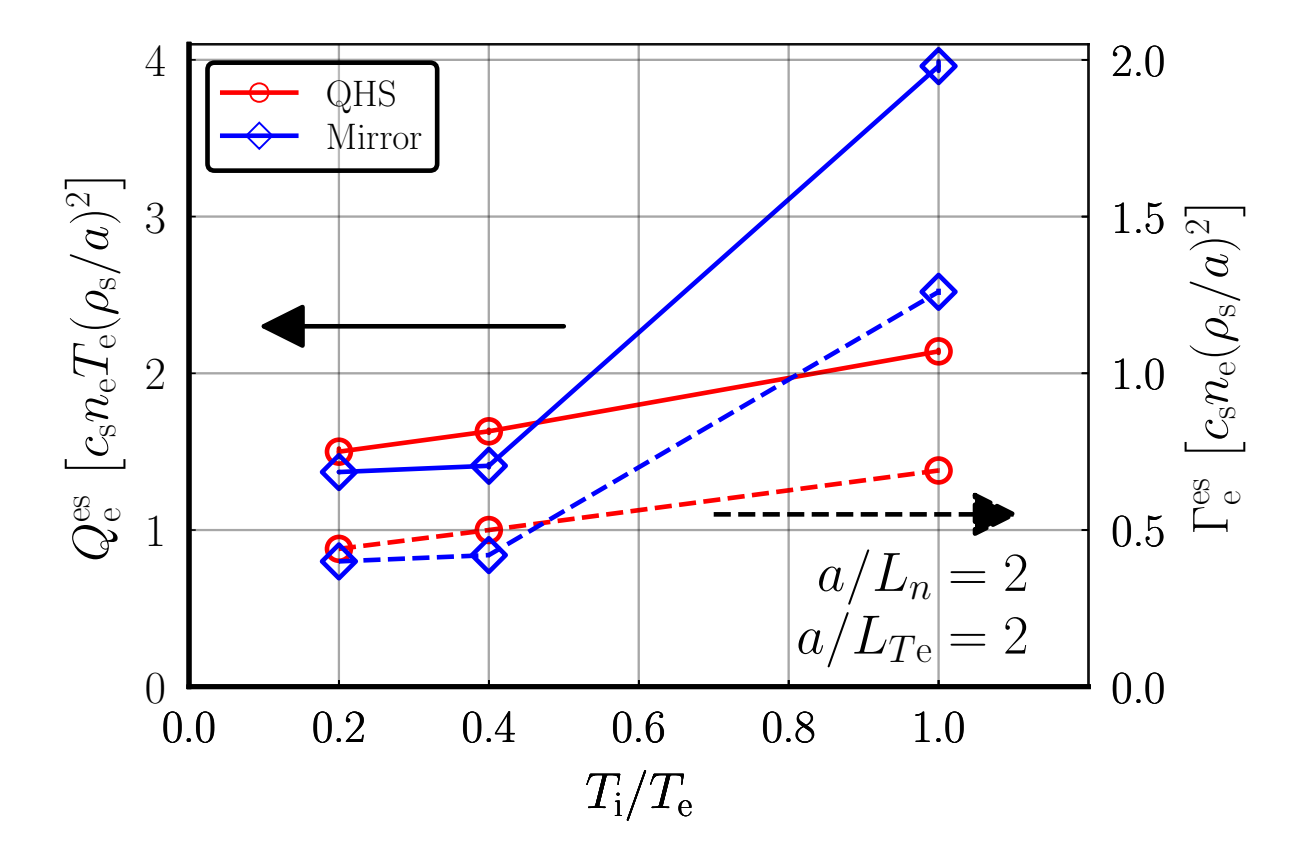


Figure 3.6: The heat flux (solid lines) and particle flux (dashed lines) from nonlinear simulations with changing temperature ratio $T_{\rm i}/T_{\rm e}$. Simulations here include both density and temperature gradient drives, $a/L_n=2$ and $a/L_{T\rm e}=2$. The large difference between QHS and Mirror configurations disappears when the ion temperature is reduced. Statistical error bars of the flux in the quasi-stationary state are much smaller than the size of symbols plotted.

the electron temperature is much higher than the ion temperature.

The difference of transport between QHS and Mirror in nonlinear simulations is indeed reduced when using the experimentally relevant $T_{\rm i}/T_{\rm e}=0.2$. This is despite the fact that the difference in heat flux at $T_{\rm i}/T_{\rm e}=1$ is opposite to what would be expected from the difference in linear growth rates. Also note that the difference in the heat flux between configurations at $T_{\rm i}/T_{\rm e}=1$ is much larger in Figure 3.6, where a temperature gradient $a/L_{T\rm e}=2$ is included, than in Figure 3.4. Within the expected range of temperature ratios $T_{\rm i}/T_{\rm e}<0.4$, the temperature ratio does not have a large effect on transport in nonlinear

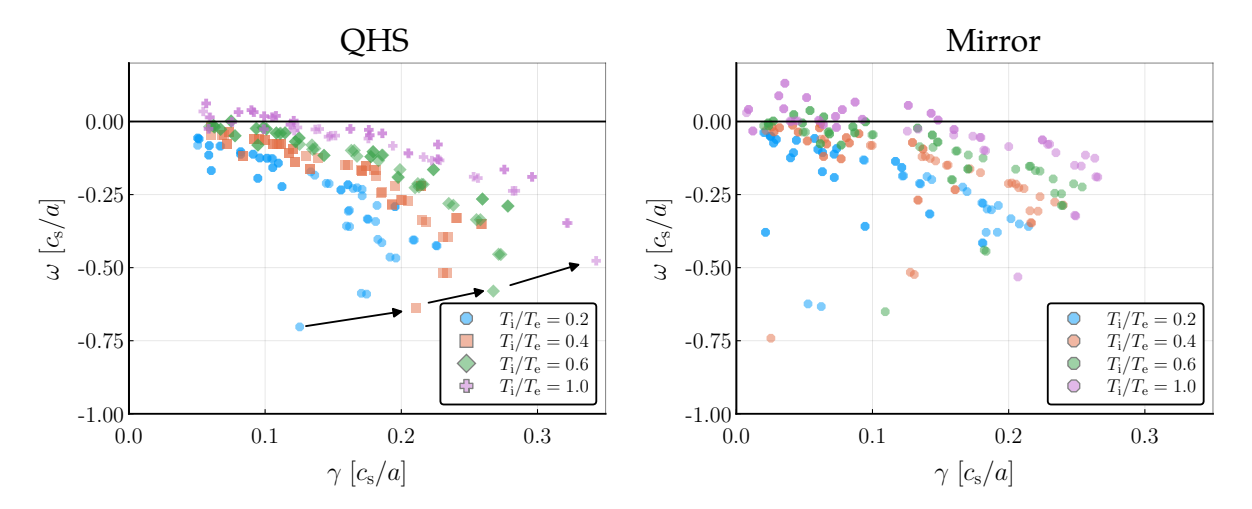


Figure 3.7: The eigenspectrum of the largest 64 modes in the QHS and Mirror configurations at $k_y \rho_{\rm s} = 0.8$ with $a/L_n = 2$ and $a/L_{T\rm e} = 2$. As the temperature ratio is increased from $T_{\rm i}/T_{\rm e} = 0.2$ to $T_{\rm i}/T_{\rm e} = 1.0$, growth rates increase and frequencies shift positive. At unity temperature ratio, a significant number of modes cross $\omega = 0$ and are in the ion diamagnetic direction. The indicated mode transitions from subdominant to dominant as $T_{\rm i}/T_{\rm e}$ is changed.

simulations, and a large difference between the actual QHS and Mirror configurations in HSX is not expected. However, the difference between QHS and Mirror could become important in an upgraded HSX with hotter ions.

As the temperature ratio is adjusted from $T_{\rm i}/T_{\rm e}=1$ to $T_{\rm i}/T_{\rm e}=0.2$, there is a significant change in the heat flux, as well as a shift in the point at which linear growth rates diverge between the QHS and Mirror configurations. A proper quasilinear estimate of transport would include the growth rates of all unstable linear modes. Such an estimate is outside the scope of this work. Instead, a cursory investigation of subdominant modes in shown in Figure 3.7. As the temperature ratio is decreased, growth rates across the spectrum decrease, as was seen in Figure 3.5. However, the frequency of modes also shifts. At $T_{\rm i}/T_{\rm e}=0.2$, all subdominant modes drift in the electron diamagnetic direction (negative ω), but a significant number of modes drift in the ion direction at $T_{\rm i}/T_{\rm e}=1$. Frequencies are involved in the coupling coefficients that determine how energy is transferred, and it is possible that this frequency shift could change the relative contribution of modes involved

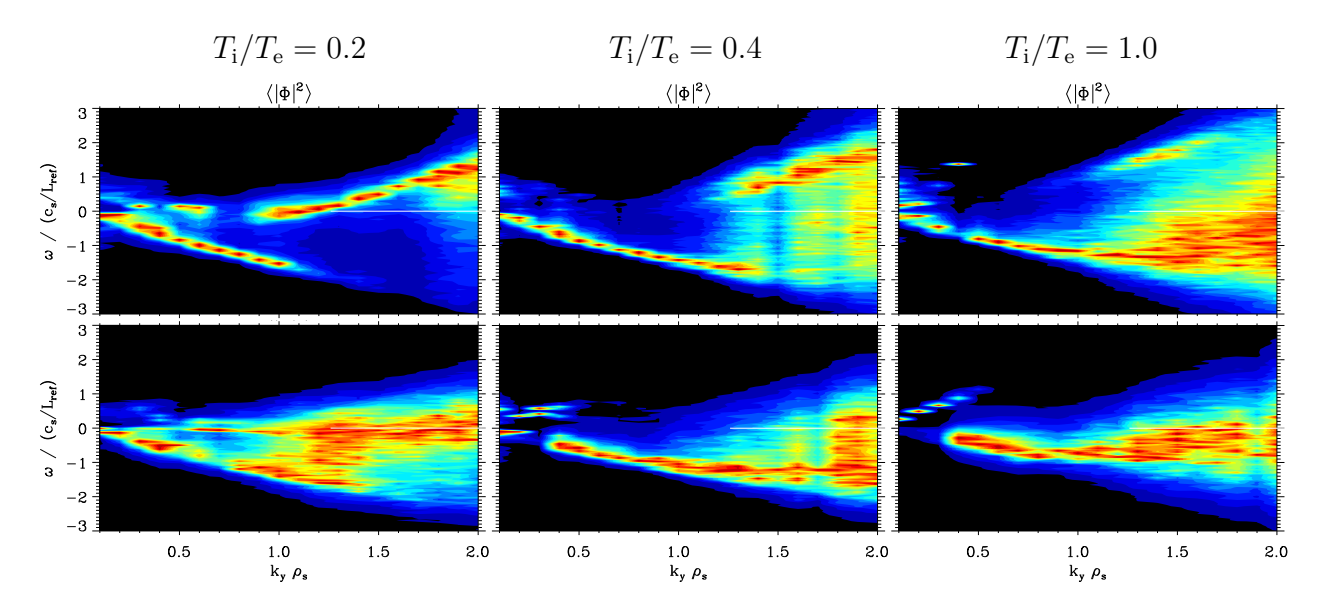


Figure 3.8: Frequencies from nonlinear simulations in QHS (top) and Mirror (bottom) geometries with $a/L_n=2$ and $a/L_{Te}=2$. The linear color scale signifies intensity and is normalized independently for each k_y . As the temperature ratio increases from left to right, the strong negative frequency band shifts in the positive direction, but does not cross $\omega=0$. In the QHS configuration, a strong positive frequency band at high k_y is reduced in intensity with increasing $T_{\rm i}/T_{\rm e}$. Conversely, at small k_y , positive-frequency modes appear at $T_{\rm i}/T_{\rm e}=1$, as discussed in Reference 3.

in turbulence saturation. In addition, a transition of the most unstable mode is apparent in the QHS configuration. The most negative frequency mode in the left plot of Figure 3.7 goes from subdominant when $T_{\rm i}/T_{\rm e}=0.2$ to dominant when $T_{\rm i}/T_{\rm e}=1$.

The frequency shift towards the ion diamagnetic direction is also seen in frequencies from nonlinear simulations in Figure 3.8, even though nonlinear frequencies do not appear to match the frequency of any linear mode. The band of negative frequencies for $k_y \rho_s \lesssim 1.5$ corresponds to the wavenumber range around the TEM transport peak. This band shifts towards positive frequencies as T_i/T_e is increased, but does not cross $\omega=0$. In the QHS configuration, there is also a band of positive frequencies at $k_y \rho_s \gtrsim 1.0$. This appears to be an analogue to the band of negative frequencies associated with nonlinear dynamics in ITG turbulence in HSX.² This mode is nearly eliminated as T_i/T_e is increased, suggesting a change in the dominant mode at high k_y . At very small k_y , positive-frequency features

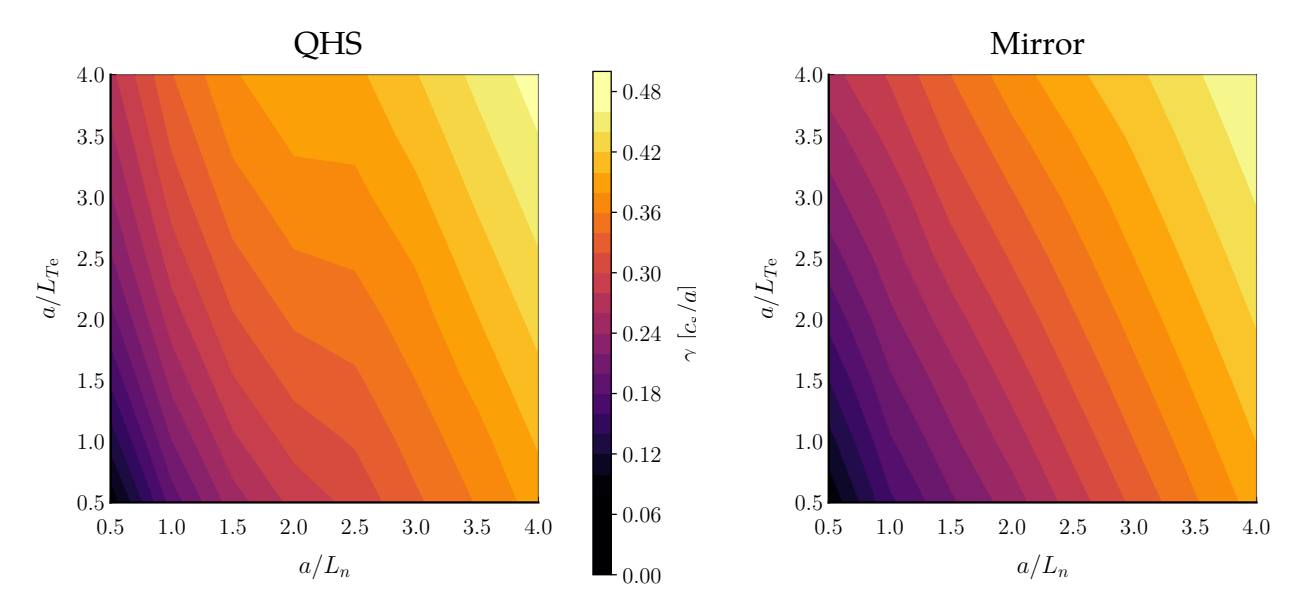


Figure 3.9: Contours of TEM growth rates over a/L_n and a/L_{Te} for $k_y \rho_s = 0.8$ at $T_i/T_e = 1$ in QHS and Mirror. Growth rates generally increase more strongly with a/L_n than a/L_{Te} . At low a/L_n , growth rates increase more steeply in the QHS configuration.

appear at $T_i/T_e = 1$, as discussed in Reference 3.

The experimental temperature ratio inverts the relative heat flux in QHS and Mirror in simulation, and can be expected to have significant effects on the gradient scaling. In Figure 3.9, contours of the linear growth rate over a/L_n and a/L_{Te} are plotted for $k_y=0.8$ and $T_{\rm i}/T_{\rm e}=0.2$. The growth rate of the TEM depends on both gradients, but somewhat more strongly on a/L_n , as expected for the ∇n -driven TEM. In the QHS configuration, growth rates increase more quickly at small a/L_n than in Mirror, but stagnate around $a/L_n\approx 2$.

The contours for $T_{\rm i}/T_{\rm e}=0.2$ in Figure 3.10 are very different than those for $T_{\rm i}/T_{\rm e}=1$ in Figure 3.9. In both configurations, the growth rates do not increase monotonically with a/L_n . This may be due to the exchange of the dominant unstable mode with a subdominant one that depends more strongly on the temperature gradient instead of the density gradient. This transition happens at a smaller a/L_n in QHS than in Mirror.

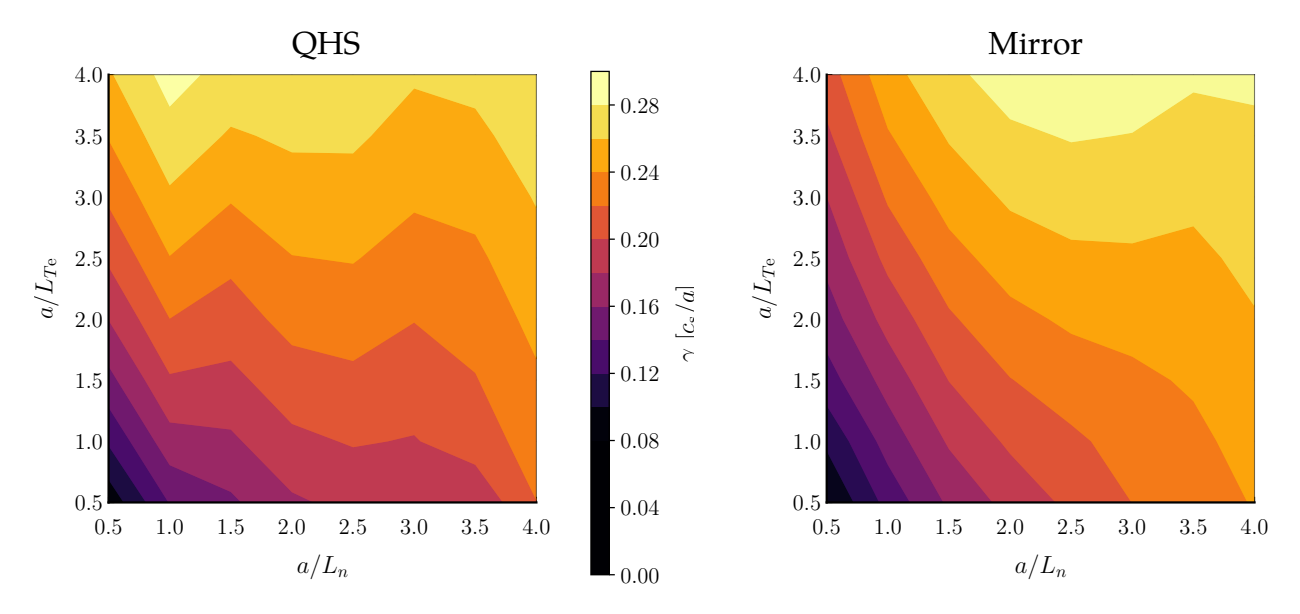


Figure 3.10: Contours of TEM growth rates over a/L_n and a/L_{Te} for $k_y\rho_s=0.8$ at $T_i/T_e=0.2$ in QHS and Mirror. In both configurations, a/L_{Te} becomes the primary drive in significant parts of the investigated parameters space. The increase of the growth rate is not monotonic with a/L_n in either configuration.

3.4 TEM simulations at experimental gradients

Turbulent fluxes can be very sensitive to the driving gradients, and experimental gradients commonly come with a large uncertainty. This combination of sensitivity and uncertainty can cause comparisons to misleadingly identify a difference between experiment and simulation. The gradients in simulation must be varied across the uncertainty of the gradient measurement to match the experimental flux in the quasi-stationary state. Further comparisons can investigate whether the underlying turbulence in this matched simulation reproduces experimental measurements. Precisely matching the flux in this way can be expensive, and instead of matching simulations to a particular experimental discharge, this section scans gradients across the experimental distribution to compare how the heat flux scales with driving gradient. Simulations here fix one gradient and scan either the density gradient $a/L_n = [1.5, 2, 2.5]$ or temperature gradient $a/L_{Te} = [1, 2, 3]$. The values of the gradient scan are based on the distribution of experimental gradients in Figure 2.2.

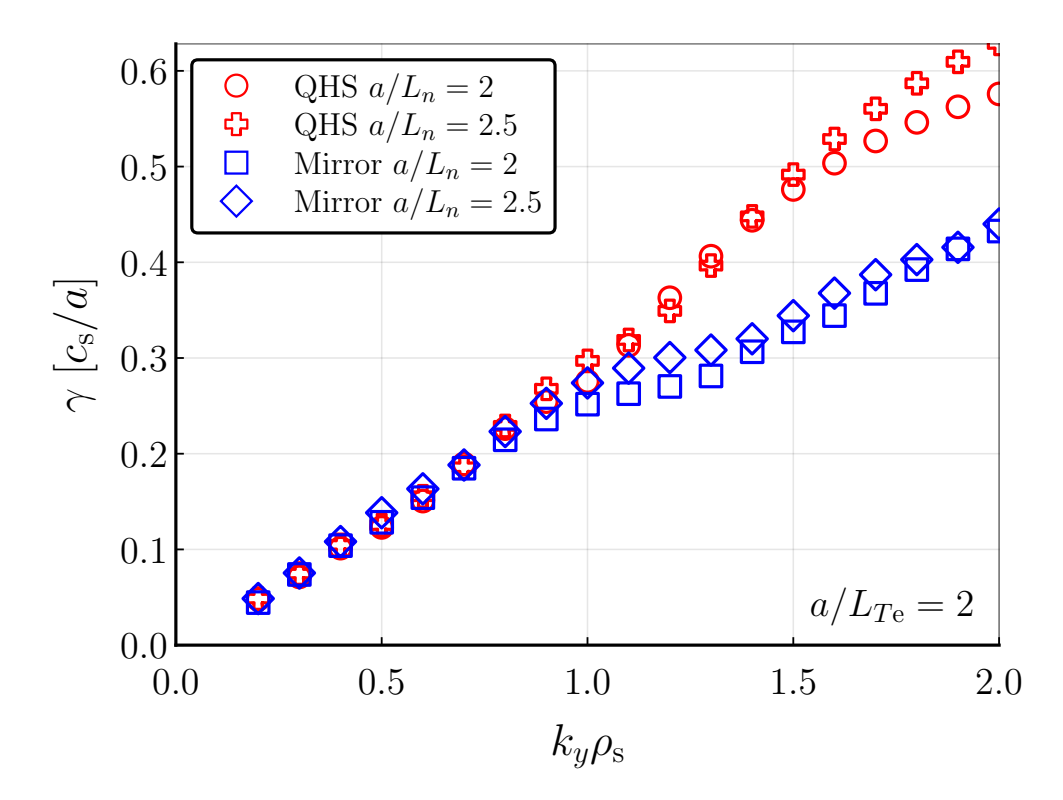


Figure 3.11: Spectra of linear growth rates with increasing a/L_n for $a/L_{Te}=2$, $T_{\rm i}/T_{\rm e}=0.2$ in the QHS and Mirror configurations. Growth rates do not differ significantly between QHS and Mirror for $k_y < 1$, but are smaller in the Mirror configuration for $k_y > 1$, similar to Figure 3.3. In both configurations, growth rates change minimally between $a/L_n=2$ and 2.5.

While Figures 3.3 and 3.9 showed that dominant linear growth rates depend strongly on the density gradient at the artificial setting of $T_{\rm i}/T_{\rm e}=1$, Figure 3.10 shows that the situation is different when $T_{\rm i}/T_{\rm e}=0.2$ as in experiment. For $a/L_n\approx 2$, growth rates are expected to scale only weakly with the density gradient. The linear growth rates in Figure 3.11 confirm this weak scaling. The Mirror configuration has reduced growth rates for $k_y\rho_{\rm s}>1$ due to the reduced overlap of particle trapping regions and bad curvature. The difference between QHS and Mirror for $k_y\rho_{\rm s}<1$ is minimal due to the temperature ratio $T_{\rm i}/T_{\rm e}=0.2$, as demonstrated in Figure 3.5. Analysis of subdominant modes at $k_y=0.8$, shown in Figure 3.12, do not identify any large change in eigenspectra with changing density gradient.

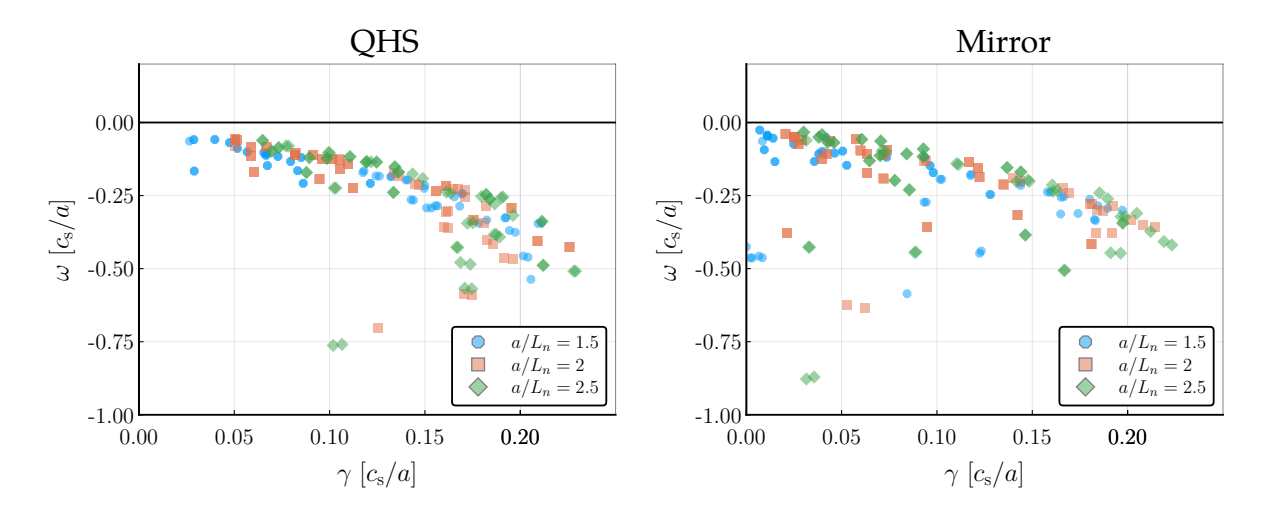


Figure 3.12: The eigenspectrum of the largest 64 modes in the QHS and Mirror configurations at $k_y \rho_s = 0.8$ with $a/L_{Te} = 2$. As the density gradient is increased, there is no clear systematic change of growth rates or frequencies of subdominant modes. Individual modes, particularly at more negative frequencies, may change significantly, and their importance to saturated turbulence is unclear. In particular, no subdominant modes are found with positive frequency.

The heat flux is plotted for nonlinear simulations scanning the density gradient in Figure 3.13. As the density gradient increases from $a/L_n=2$ to 2.5, the heat flux increases steeply by a factor of about 2.5. This increase in transport raises the possibility that the ∇n -driven TEM could be limiting the maximum achievable profile gradients at this location in both the QHS and Mirror configurations. Very few profiles have density gradients larger than $a/L_n \gtrsim 2.5$ in Figure 2.2. However, more nonlinear simulations are needed to understand if the increased flux is a function of a/L_n or L_{Te}/L_n in order to compare to the distribution of experimental profiles. While linear growth rates in Figure 3.11 and 3.12 increase slightly with density gradient, there is no sudden change in growth rates similar to the steep change in heat flux. At the high k_y where QHS and Mirror do differ, the usual quasilinear expectation $(Q \sim \gamma/k_y^2)$ would suggest that these modes contribute only slightly to the nonlinear heat flux. Differences between the QHS and Mirror configuration in nonlinear simulation are small, and this difference would not be measurable in the experiment.

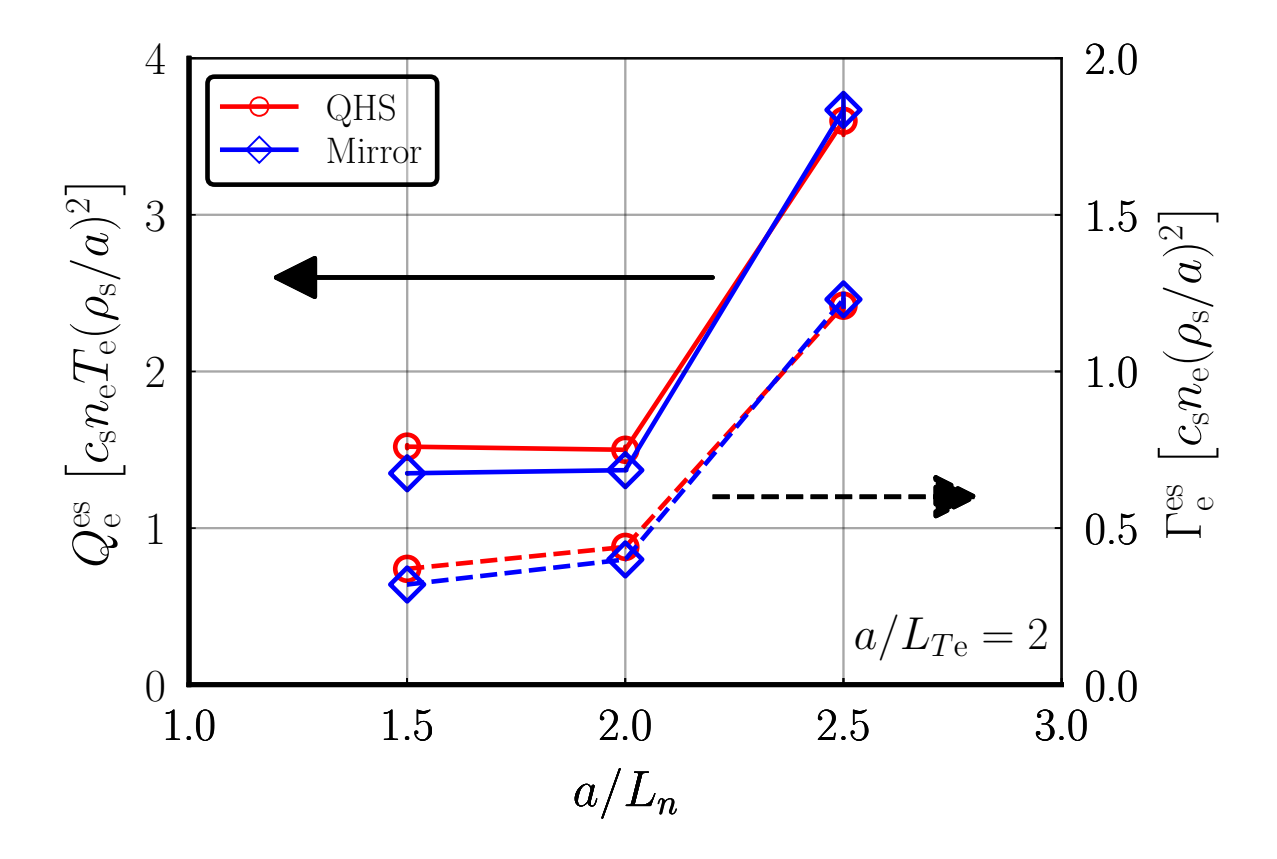


Figure 3.13: The nonlinear heat flux (solid lines) and particle flux (dashed lines) for simulations scanning a/L_n with $a/L_{T\rm e}=2$ and $T_{\rm i}/T_{\rm e}=0.2$ show no significant difference between the QHS and Mirror configurations. However fluxes increase sharply above $a/L_n=2$. Statistical error bars of the flux in the quasi-stationary state are much smaller than the size of symbols plotted.

As seen in Figure 3.14, increasing the temperature gradient proportionally increases growth rates across all k_y , as expected from Figures 3.5 and 3.10. The eigenspectrum in Figure 3.15 shows that growth rates increase for all subdominant modes, but does not find any frequency shift or change in dominant mode. However, the transport in nonlinear simulations scanning the temperature gradient, shown in Figure 3.16, do not increase smoothly with temperature gradient. Particularly at $a/L_{Te}=3$, where linear growth rates in Figure 3.14 increase similarly for both the QHS and Mirror configuration, the heat flux increases in QHS but not in Mirror. In addition, the heat and particle flux do not

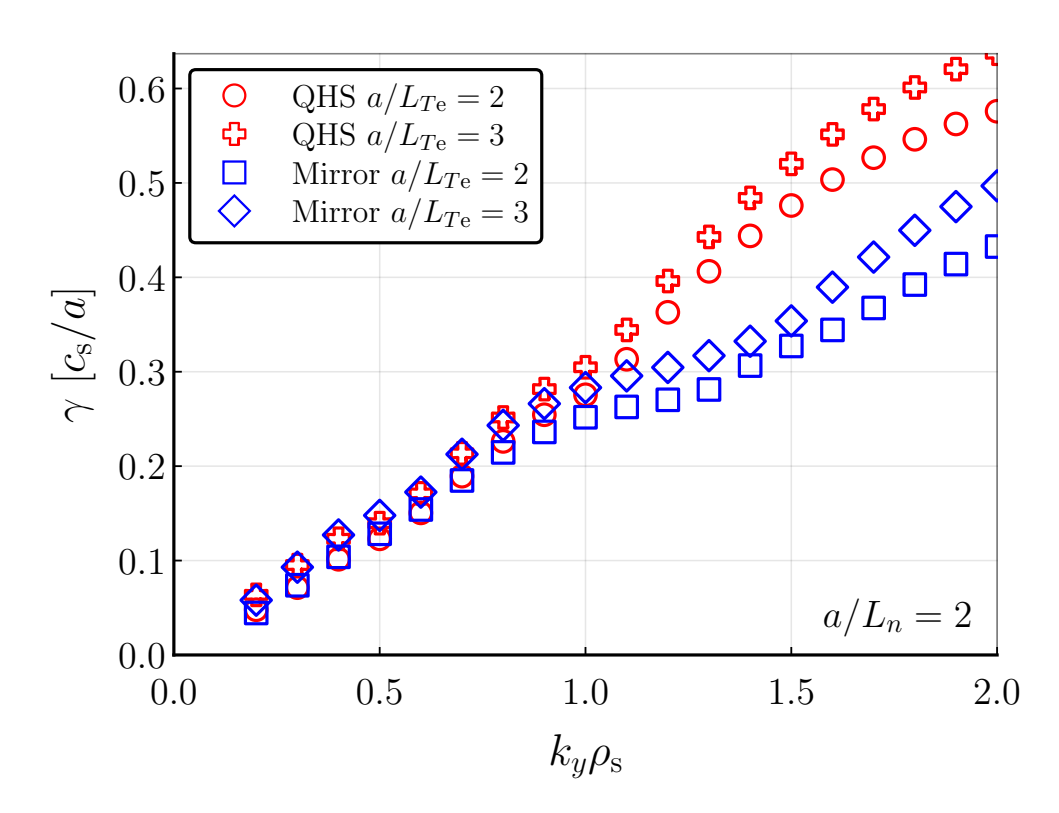


Figure 3.14: Linear growth rates for $a/L_n=2$, $T_{\rm i}/T_{\rm e}=0.2$ in the QHS and Mirror configurations. Similar to Figure 3.11, growth rates do not differ significantly between QHS and Mirror for the range of transport-relevant wavenumbers $k_y<1$. Increasing the temperature gradient increases the growth rates evenly across the spectrum for both configurations.

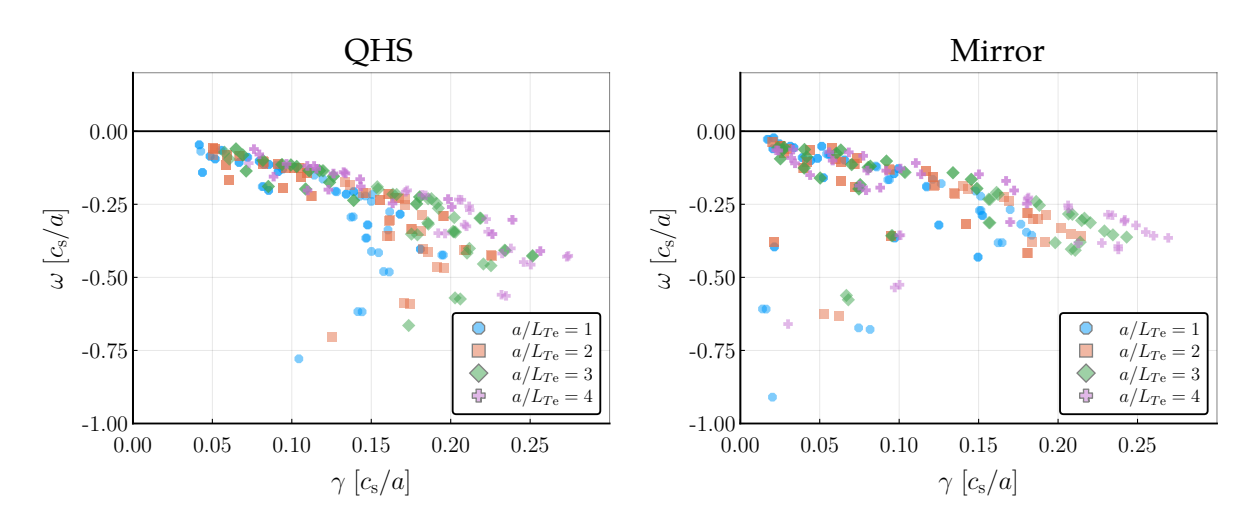


Figure 3.15: The eigenspectrum of the largest 64 modes in the QHS and Mirror configurations at $k_y \rho_s = 0.8$ with $a/L_n = 2$. As the temperature gradient is increased, growth rates increase proportionally in both configurations, as opposed to the unclear change with a/L_n in Figure 3.12.

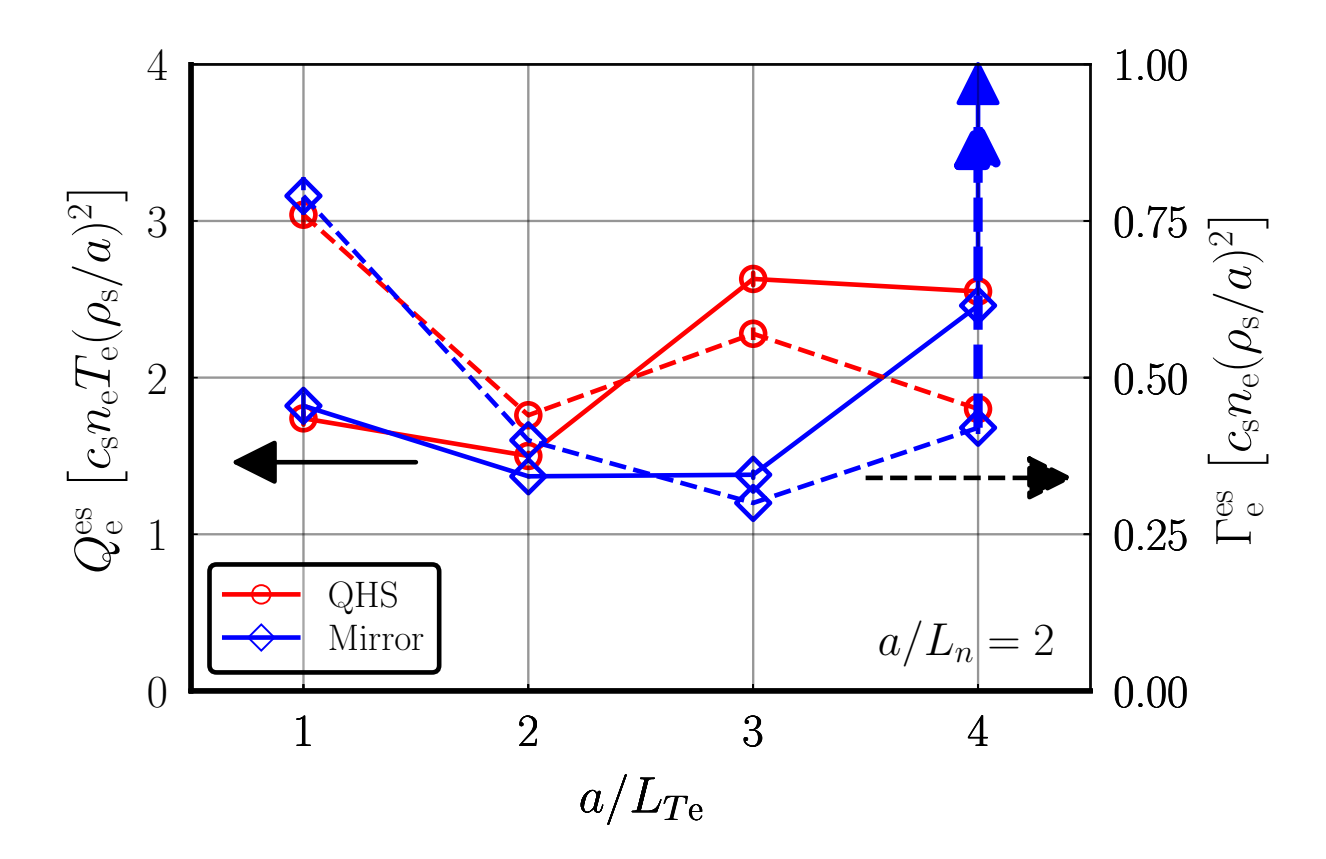


Figure 3.16: The nonlinear heat flux ($Q_{\rm e}^{\rm es}$, solid lines) and particle flux ($\Gamma_{\rm e}^{\rm es}$, dashed lines) for simulations scanning $a/L_{T\rm e}$ with $a/L_n=2$ and $T_{\rm i}/T_{\rm e}=0.2$. Unlike the a/L_n scan in Figure 3.13, the dependence on $a/L_{T\rm e}$ is different between the heat and particle flux. For $a/L_{T\rm e}>a/L_n$, the heat flux is more sensitive than $\Gamma_{\rm e}^{\rm es}$ to the gradient drive, though this dependence is still weaker than the dependence on a/L_n . For $a/L_{T\rm e}<a/a/L_n$, the particle flux increases sharply, while there is only a moderate increase in $Q_{\rm e}^{\rm es}$. The Mirror simulation at $a/L_{T\rm e}=4$ shows a likely transition to a higher-flux state, as discussed in the text. Statistical error bars of both the heat and particle fluxes in the quasi-stationary state are much smaller than the size of symbols plotted.

scale similarly with the temperature gradient. While the temperature gradient is larger than the density gradient, the heat flux roughly increases with increasing a/L_{Te} , but the particle flux is significantly less sensitive. Both fluxes increase when the temperature gradient is smaller than the density gradient, but the increase in particle flux is much larger. The fluxes are described by Equation 3.2, and the different dependence of the heat and particle flux is directly related to different temperature and density fluctuation amplitudes in the simulations. These results show that the particle flux may actually be reduced by increasing a/L_{Te} . The more complex dependence of $\Gamma_{\rm e}^{\rm es}$ is likely related to nontrivial competition between the diffusive and convective components of the flux, whereas the heat flux is predominantly diffusive. Crossing $a/L_n = a/L_{Te}$ results in a change of the dominant gradient-drive, which is associated here with different sensitivities to the gradient. Simulations are needed that scan gradients without crossing $a/L_n = a/L_{Te}$ to understand the significance of which gradient drives turbulence. This gradient at $a/L_{Te} = 4$ is not comparable to experimental data, and was included merely to elucidate underlying physics. In the Mirror simulation, the turbulent flux, after reaching an apparently quasi-stationary state, began to rise strongly, possibly transitioning to a higher-flux state. This could indicate a slowly growing mode or slowly building nonlinear interaction process that requires long simulation times to properly resolve.

Spectra of the heat flux from nonlinear simulations, presented in Figures 3.17 and 3.18, show that the bulk of transport is driven by modes around $k_y \rho_{\rm s} \approx 1$. As the density gradient increases in Figure 3.17, the peak flux shifts slightly to higher wavenumbers. Nonlinear simulations in Reference 3 with $T_{\rm i}/T_{\rm e}=1$ previously identified a low- k_y feature in flux spectra of the QHS configuration. This feature is reproduced in Figures 3.17 and 3.18 for simulations with finite $a/L_{T\rm e}$ and $T_{\rm i}/T_{\rm e}=0.2$. The low- k_y peak does not depend only on a/L_n , but rather increases in height with some ratio of a/L_n to $a/L_{T\rm e}$. The peak is stronger in the Mirror configuration, and appears when $a/L_n=a/L_{T\rm e}$, while a/L_n must be larger

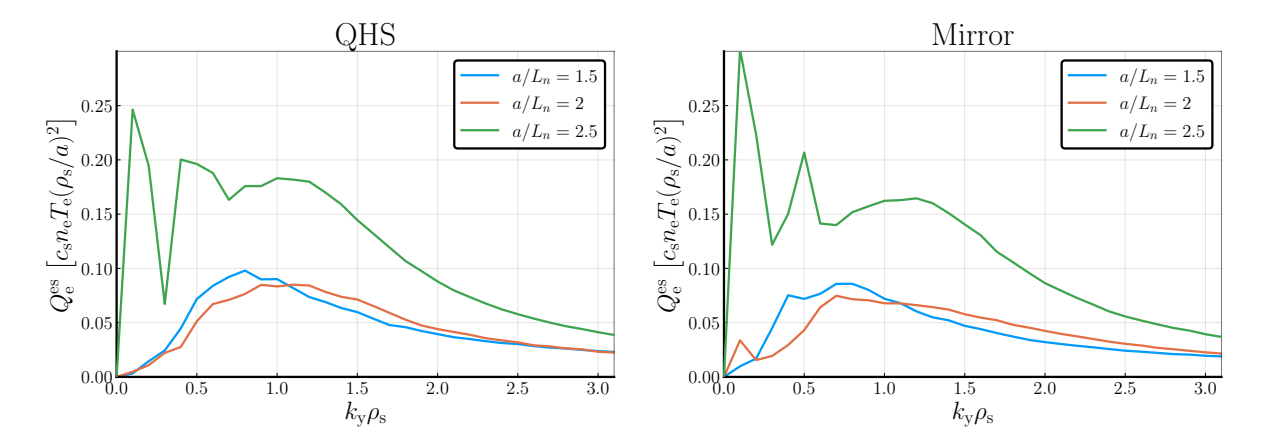


Figure 3.17: Heat flux spectra from nonlinear simulations in the QHS and Mirror density gradient scans ($a/L_{Te}=2$). The bulk flux peak shifts from $k_y\rho_{\rm s}\approx 0.8$ to $k_y\rho_{\rm s}\approx 1.2$ with increasing a/L_n . The low- k_y peak³ increases with a/L_n , and is stronger in the Mirror configuration.

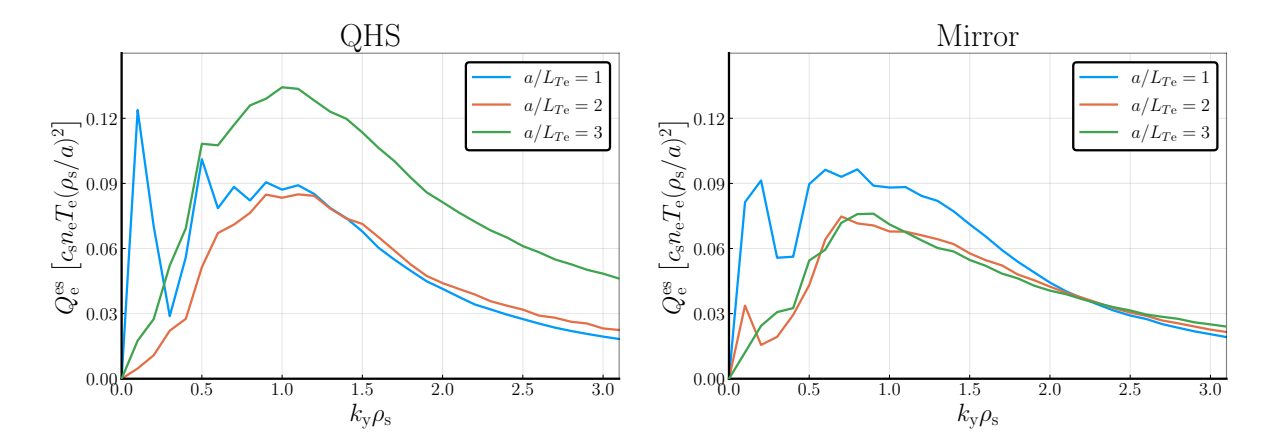


Figure 3.18: Heat flux spectra from nonlinear simulations in the QHS and Mirror temperature gradient scans ($a/L_n=2$). The bulk flux peak does not significantly shift with a/L_{Te} , and the low- k_y peak decreases with the a/L_{Te} .

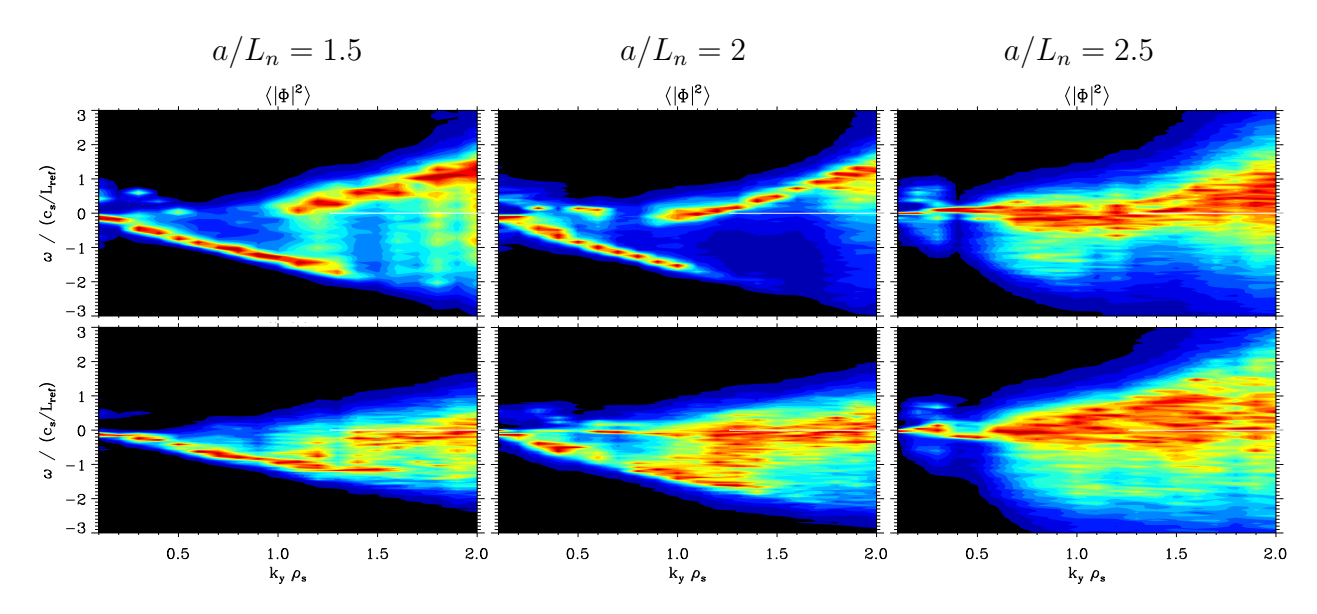


Figure 3.19: Frequencies from nonlinear simulations in QHS (top) and Mirror (bottom) with $a/L_{\rm Te}=2$ and $T_{\rm i}/T_{\rm e}=0.2$. The color scale is linear and independent for each k_y . As the density gradient increases, the strong negative frequency band recedes towards small k_y and is replaced by a wide positive frequency band from high k_y .

than a/L_{Te} to drive the peak in the QHS configuration. As discussed in Reference 3, this feature is well resolved numerically and, for realistic gradients, does not correspond to much flux relative to the total flux. However, it may have an effect on energy transfer between modes and the overall saturation level. A greater understanding of the low- k_y peak is left for future work.

In Figure 3.13, transport increases sharply as the density gradient is increased above $a/L_n = a/L_{Te}$. In Figure 3.16, there is a similar increase in transport above $a/L_{Te} = a/L_n$ in QHS. However, in the QHS configuration, the dependence of the heat flux on the temperature gradient between $a/L_{Te} = 2$ and 3 is weaker than the dependence on the density gradient between $a/L_n = 2$ and 2.5 by a factor of three. Linear growth rates in Figure 3.11 predicted no change with density gradient, while growth rates in Figure 3.14 increase with a/L_{Te} . Instead, the nonlinear heat flux is more sensitive to the density gradient.

The frequency spectra from nonlinear simulations offer a clue to explain the discrepancy

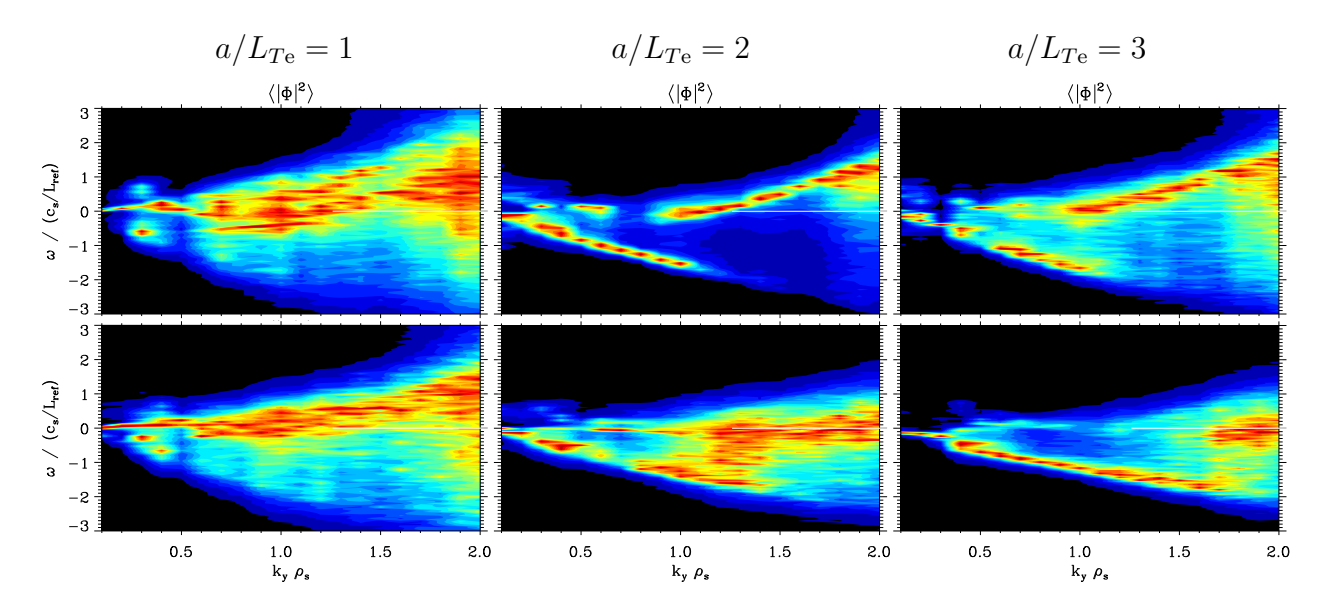


Figure 3.20: Frequencies from nonlinear simulations in QHS (top) and Mirror (bottom) with $a/L_n=2$ and $T_{\rm i}/T_{\rm e}=0.2$. The color scale is linear and independent for each k_y . At $a/L_{T\rm e}=1$, frequencies are broad and in the positive direction. At $a/L_{T\rm e}=3$, the well-defined negative frequency band takes over for mid-range k_y .

between linear growth rates and nonlinear heat flux. The frequency shift changes in Figure 3.19 suggests a qualitative change in the turbulence as the density gradient is increased. When $a/L_n \leq a/L_{Te}$, a distinct negative frequency band exists up to $k_y \rho_s \approx 1.5$, which covers the range of wavenumbers responsible for most transport. In Reference 3, this band was associated with the TEM. However, as the density gradient is increased, this band of negative frequencies recedes to small k_y , and is replaced by a positive frequency band. For $a/L_n > a/L_{Te}$, frequencies in the nonlinear simulation are broadly positive for all k_y . This is coincident with a shift of the flux spectra peak to higher k_y in Figure 3.17. Within the 64 most unstable subdominant modes in Figure 3.12, no modes are found with a positive frequency. This strengthens the interpretation that a nonlinear effect must be responsible for key dynamics. In comparison to Figure 3.8, increasing a/L_n has a similar effect on the nonlinear frequencies as decreasing T_i/T_e .

In simulations scanning a/L_{Te} , shown in Figure 3.20, the frequency change with increasing gradient is inverse to that in Figure 3.19. At $a/L_{Te} = 1$, a broad band of frequencies

in the ion direction (positive ω) dominate the turbulence for all k_y . This is similar to the situation when $a/L_n > a/L_{Te}$ in Figure 3.19. When the temperature gradient is increased, the negative frequency band becomes important for mid-range k_y , but coexists with the positive frequencies when $a/L_{Te} = a/L_n$. In the QHS configuration, where transport increases for $a/L_{Te} = 3$, the positive frequencies are still apparent at $k_y \rho_s = 1$. In the Mirror configuration, negative frequencies dominate for $k_y \rho_s < 1.7$, covering the range of k_y values most responsible for transport. Heuristically, scaling with driving gradients is sensitive to whether the negative frequency or positive frequency turbulence is responsible for transport. The transition between modes is not surprising, as the experimental gradients lie at the transition between a/L_n and a/L_{Te} drive. However, the sensitivity of transport to the gradient ratio implies that only gross comparisons can be made to the experimental measurements in Chapter 2. The uncertainty in profile gradients in Figure 2.2 is large enough that the dominant gradient drive cannot be determined with certainty in most cases.

However, the different scaling of the heat flux in these two regimes may be important for profile shapes in HSX. While the temperature gradient is larger than the density gradient, the scaling of thermal transport may be reduced as compared to the ∇n -driven regime, and it is possible that the thermal diffusivity could be a function of L_{Te}/L_n . In that case, if a large temperature gradient can be maintained, turbulence may be in the ∇T_e -driven regime with reduced thermal transport so that an even larger gradient may result. However, if the temperature gradient drops below the density gradient, TEM turbulence is in the ∇n -driven regime, and increased thermal transport may further flatten the gradient. The radial variation in the density and temperature profile in HSX offers an intriguing opportunity to investigate the dependence of turbulent transport on the ∇n -driven versus the ∇T_e -driven regimes.

3.5 Comparison to experimental measurements

In this section, nonlinear simulations at HSX experimental parameters are compared to the experimental measurements presented in Chapter 2. While not a full validation study, comparison to measurements can identify the necessary steps to make such a study possible, such as more precise measurements or simulations more accurately matched to experimental conditions. In this chapter, TEM simulations have used an x and y local flux-tube domain from the r/a = 0.7 surface, while measurements are from r/a = 0.5. While the low global shear in HSX means that the geometry does not change too much between surfaces, it is not clear how strongly geometry needs to be modified before nonlinear dynamics are altered. Also, the flux-tube simulation domain is a reduced geometry representation. As it does not include a full flux surface, no radial electric field can be included in simulation. Ambipolar radial electric fields may drive flows that shift turbulence on the flux surface to a different geometry, and may interact with the amplitude of zonal flows. As a radially-local representation, the flux tube may not account for profile effects on the order of the width of zonal flows, which could be important for turbulence saturation. Additionally, it is unlikely that the normalized ion temperature gradient is zero, as is used for simulations in this chapter, and an ion temperature gradient could affect the linear physics of the TEM.

Heat flux compared to experimental power balance

In Section 2.2, it was found that the energy transport is larger in Mirror than in QHS at the mid-radius when the gradient drive is matched between configurations. This is demonstrated by the larger heat flux in Figure 2.6, the larger thermal diffusivity in Figure 2.7, and the matched heat flux at smaller a/L_n in Figure 2.9. This difference in transport is not reproduced in simulations at the experimental temperature ratio T_i/T_e . However, fluxes are sensitive to whether turbulence is in the ∇n -driven or ∇T_e -driven regime. Small

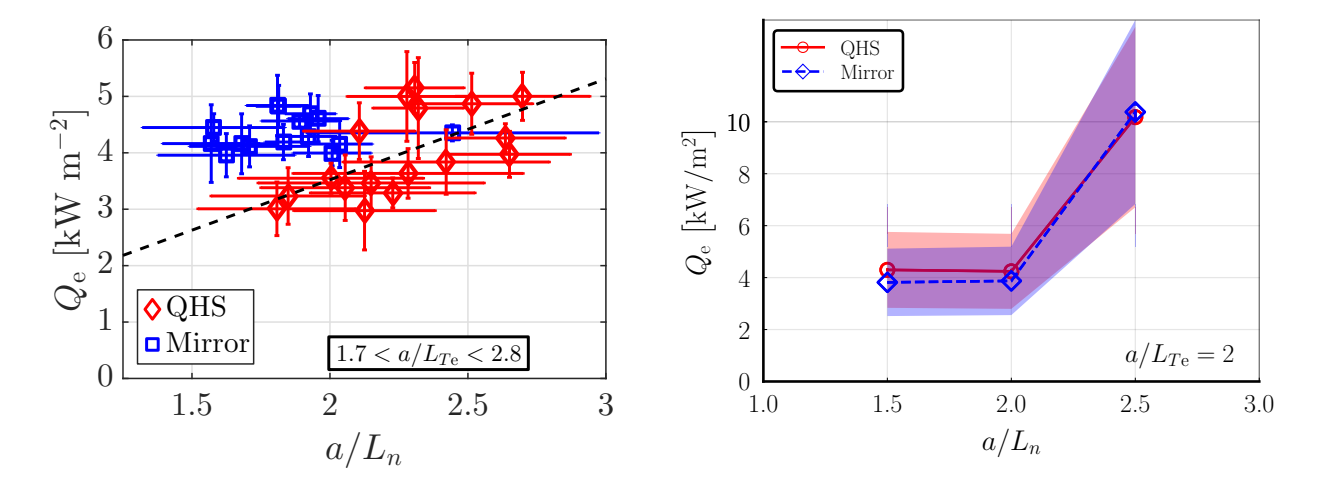


Figure 3.21: The heat flux increases with increasing density gradient a/L_n in both experimental measurements (left) and Gene simulations (right). The heat flux in simulation matches that from experiment at about $4\,\mathrm{kW}\,\mathrm{m}^{-2}$. The shaded uncertainty comes from the distribution of electron temperatures and densities for the experimental profiles represented in the experimental data on the left. The statistical uncertainty of individual nonlinear simulations is comparatively small.

changes in gradient may change the dominant drive and cause significant changes in flux. In Section 3.3, simulations with temperature ratio $T_{\rm i}/T_{\rm e}=1$ do produce a larger hear flux in the Mirror configuration, and frequency spectra show a similar change to scanning gradients between the ∇n -driven and $\nabla T_{\rm e}$ -driven regimes. More precise gradient measurements would be required for full validation of the configurational dependence of the TEM.

However, nonlinear simulations do reproduce the general dependence of the TEM in HSX. In both simulation and experiment, the heat flux increases more strongly with the density gradient than the temperature gradient. The normalizations used in the Gene code must be accounted for to directly compare the heat flux from simulation and experiment. In particular, this normalization depends on the background density and electron temperature. However, the experimental data represents a number of different discharges with a range of plasma profiles. The distribution of densities and temperatures in the selection of experimental profiles is accounted for as uncertainty of the normalization parameters.

As seen in Figure 3.21, the heat flux from simulation of TEM turbulence does account for the heat flux in experimental discharges, being about $4\,\mathrm{kW\,m^{-2}}$ in both cases. These comparisons confirm that ∇n -driven TEM turbulence is the dominant driver of anomalous transport in HSX. The heat flux increases sharply for the simulation with a larger density gradient, up to $10\,\mathrm{kW\,m^{-2}}$. It is possible that this strong boost of the TEM turbulence may be responsible for limiting the achievable gradients in the experiment, and may explain the lack of profiles with $a/L_n > 2.5$ in Figure 2.2. Identification of the specific gradients at which this transition happens in the QHS and Mirror configurations may explain the typically larger density gradient in the QHS configuration. In addition, the weaker dependence on the temperature gradient may explain the broader range $0 \lesssim a/L_{Te} \lesssim 4$ of that gradient in experimental data.

Density fluctuation amplitude compared to reflectometry

Density fluctuations are a local quantity, and comparison between simulation and experiment is sensitive to the precise location of measurement. In a perfectly axisymmetric tokamak, each flux tube on a given surface is identical, and a single $n_{\rm pol}=1$ flux tube can represent any point on the flux surface. In a stellarator, each flux tube on a surface is unique, and there is no guarantee that a given observation volume will overlap with the computational domain. This consideration was important in the choice of reflectometry for comparison to simulation. The HSX reflectometer is positioned on the outboard mid-plane of the "bean"-shaped cross section, which is precisely the midpoint of the flux tube used in simulation. For a probe beam perpendicular to the surface and small-amplitude density fluctuations, most of the reflected power comes from the vicinity of the probe beam axis. As a first-order comparison to experiment, the reflectometer measurement volume is taken to be only the z=0 midpoint of the flux tube.

The reflectometer measures fluctuations in the range $0.2 \lesssim k_{\perp} \rho_{\rm s} \lesssim 1$. In reality, the

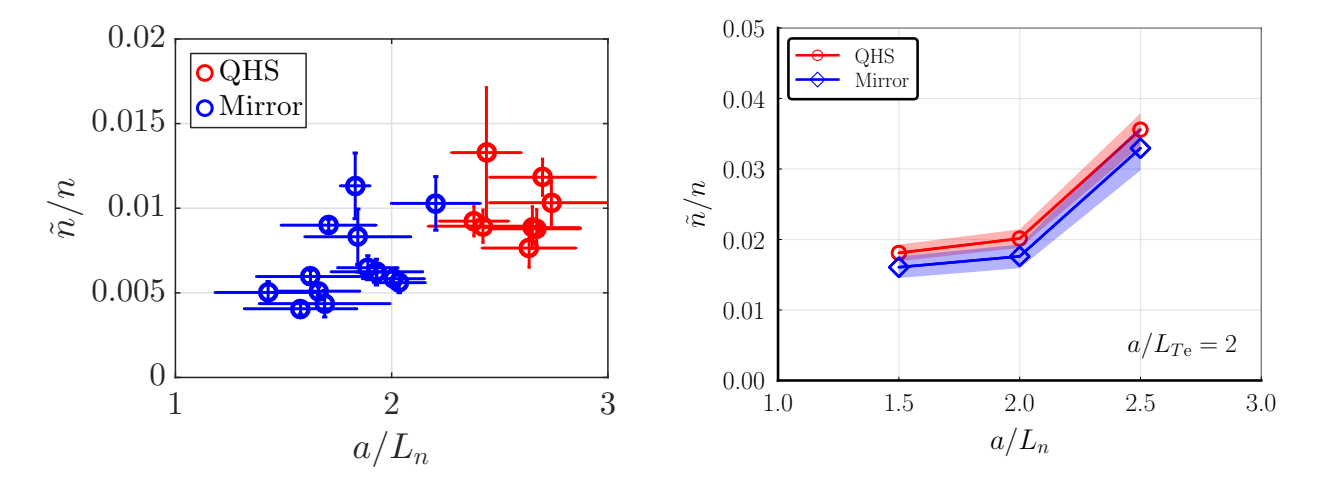


Figure 3.22: The density fluctuation amplitude increases with increasing density gradient a/L_n in both reflectometer measurements (left) and Gene simulations (right). Fluctuations in simulation are larger than measurements by a factor of ≈ 3 . The shaded uncertainty for simulated fluctuations comes from the distribution of electron temperatures for the experimental profiles represented in the reflectometer data.

diagnostic has some instrument function that determines the response to fluctuations at a given wavenumber. However, for the analysis here, the density fluctuation spectrum is integrated across the given k_{\perp} range. The conversion to Gene wavenumbers²² depends on geometric coefficients as $k_{\perp}/k_y = \sqrt{g^{xx}g^{yy} - (g^{xy})^2/g^{xx}}$. At the midpoint of the flux tube, where the reflectometer measurement is located, the right side is unity and $k_{\perp} = k_y$. This approximation of an instrument function is a crude synthetic diagnostic, but application to simulation data is fast and straightforward.

The results of this analysis are shown on the right of Figure 3.22, with fluctuations from reflectometry shown on the left. In Gene, fluctuating quantities include a normalization factor of ρ_s/a . The reflectometer measurements on the left of Figure 3.22 come from plasma profiles with a distribution of electron temperatures. The uncertainty on simulated fluctuation amplitudes comes from this distribution through the temperature dependence of $\rho_s = \sqrt{T_e m_i c/(eB_0)}$, where c is the speed of light, e is the elementary charge, and B_0 is the magnetic field on axis. In both simulation and experiment, density fluctuations

increase with increasing density gradient. There is not enough experimental data to differentiate between the QHS and Mirror configurations, but no difference is expected from Gene simulations. This mirrors the scaling of the heat flux, and indicates that density fluctuations are a good indicator of the amplitude of ∇n -driven TEM turbulence. However, density fluctuations from simulation are about three times as large as fluctuations measured by reflectometry. It is conceivable that this factor of three could come from the synthetic diagnostic described in this section. Future work will need to model the full electromagnetic wave propagation and reflection from a fluctuating cutoff layer. The IPF-FD3D code 23 has been developed for this purpose and has been used to model reflection from fluctuations in Gene simulations. 24

3.6 Chapter Summary

This Chapter has described Gene simulations of TEM turbulence in the QHS and Mirror configurations. In Section 3.2, it was shown that linear growth rates are smaller in the Mirror configuration as expected from the reduced overlap of trapped particle and bad curvature regions. However, the heat flux in nonlinear simulations is significantly larger in the Mirror configuration for $T_{\rm i}/T_{\rm e}=1$. Simulations with experimental temperature gradients and temperature ratio $T_{\rm i}/T_{\rm e}=0.2$ are required to compare to experimental measurements, and including these temperature effects in Section 3.3 eliminates the difference in heat flux between QHS and Mirror. Section 3.4 presented nonlinear simulations scanning the range of experimental gradients from Chapter 2. The transition between $\nabla T_{\rm e}$ and ∇n drive is associated with a change from negative to positive frequencies in nonlinear simulations. HSX profiles straddle this mode boundary, and uncertainties in experimental gradients make it much more difficult for simulations to match a specific experimental discharge. Comparisons between the simulations in Section 3.4 and experimental measurements in

Chapter 2 were presented in Section 3.5. It is shown that the heat flux from simulated TEM turbulence can account for the anomalous transport in HSX at r/a = 0.5. In both simulation and experiment, heat flux and density fluctuations increase with a/L_n , but show little dependence on a/L_{Te} .

References

- [1] T. Dannert and F. Jenko, *Gyrokinetic simulation of collisionless trapped-electron mode turbulence*, Physics of Plasmas **12**, 072309 (2005).
- [2] M. J. Pueschel, B. J. Faber, J. Citrin, C. C. Hegna, P. W. Terry, and D. R. Hatch, *Stellarator turbulence: Subdominant eigenmodes and quasilinear modeling*, Physical Review Letters **116**, 085001 (2016).
- [3] B. J. Faber, M. J. Pueschel, J. H. E. Proll, P. Xanthopoulos, P. W. Terry, C. C. Hegna, G. M. Weir, K. M. Likin, and J. N. Talmadge, *Gyrokinetic studies of trapped electron mode turbulence in the Helically Symmetric eXperiment stellarator*, Physics of Plasmas 22, 072305 (2015).
- [4] F. Jenko, W. Dorland, M. Kotschenreuther, and B. N. Rogers, *Electron temperature gradient driven turbulence*, Physics of Plasmas 7, 1904 (2000).
- [5] P. Xanthopoulos, W. A. Cooper, F. Jenko, Y. Turkin, A. Runov, and J. Geiger, *A geometry interface for gyrokinetic microturbulence investigations in toroidal configurations*, Physics of Plasmas **16**, 082303 (2009).
- [6] S. P. Hirshman and J. C. Whitson, *Steepest-descent moment method for three-dimensional magnetohydrodynamic equilibria*, Physics of Fluids **26**, 3553 (1983).
- [7] M. A. Beer, *Gyrofluid Models of Turbulent Transport in Tokamaks*, Ph.D. thesis, Princeton University (1995).
- [8] R. C. Grimm, J. M. Greene, and J. L. Johnson, in *Methods in Computational Physics: Advances in Research and Applications*, Controlled Fusion, Vol. 16, edited by J. Killeen (Elsevier, 1976) pp. 253–280.
- [9] A. R. Briesemeister, Measurement and Modeling of the Flows and Radial Electric Field in the HSX Stellarator, Ph.D. thesis, The University of Wisconsin-Madison (2013).
- [10] A. Briesemeister, K. Zhai, D. T. Anderson, F. S. B. Anderson, and J. N. Talmadge, *Comparison of the flows and radial electric field in the HSX stellarator to neoclassical calculations*, Plasma Physics and Controlled Fusion **55**, 014002 (2013).
- [11] S. T. A. Kumar, J. N. Talmadge, T. J. Dobbins, F. S. B. Anderson, K. M. Likin, and D. T. Anderson, *Determination of radial electric field from Pfirsch–Schlüter flows in the HSX stellarator*, Nuclear Fusion **57**, 036030 (2017).
- [12] S. T. A. Kumar, T. J. Dobbins, J. N. Talmadge, R. S. Wilcox, and D. T. Anderson, *Radial electric field and ion parallel flow in the quasi-symmetric and Mirror configurations of HSX*, Plasma Physics and Controlled Fusion **60**, 054012 (2018).

- [13] B. J. Faber, M. J. Pueschel, P. W. Terry, C. C. Hegna, and J. E. Roman, *Stellarator microinstabilities and turbulence at low magnetic shear*, Journal of Plasma Physics **84**, 905840503 (2018).
- [14] J. Smoniewski, E. Sánchez, I. Calvo, M. J. Pueschel, and J. N. Talmadge, *Comparison of local and global gyrokinetic calculations of collisionless zonal flow damping in quasi-symmetric stellarators*, Physics of Plasmas **28**, 042503 (2021).
- [15] P. Xanthopoulos, H. E. Mynick, P. Helander, Y. Turkin, G. G. Plunk, F. Jenko, T. Görler, D. Told, T. Bird, and J. H. E. Proll, *Controlling turbulence in present and future stellarators*, Physical Review Letters **113**, 155001 (2014).
- [16] C. B. Deng, D. L. Brower, D. T. Anderson, F. S. B. Anderson, A. Briesemeister, and K. M. Likin, *Core density turbulence in the HSX Stellarator*, Nuclear Fusion **55**, 123003 (2015).
- [17] W. Guttenfelder, D. T. Anderson, F. S. B. Anderson, J. M. Canik, K. M. Likin, and J. N. Talmadge, *Edge turbulence measurements in electron-heated Helically Symmetric Experiment plasmas*, Physics of Plasmas **16**, 082508 (2009).
- [18] G. M. Weir, B. J. Faber, K. M. Likin, J. N. Talmadge, D. T. Anderson, and F. S. B. Anderson, *Profile stiffness measurements in the Helically Symmetric experiment and comparison to nonlinear gyrokinetic calculations*, Physics of Plasmas **22**, 056107 (2015).
- [19] A. Casati, C. Bourdelle, X. Garbet, F. Imbeaux, J. Candy, F. Clairet, G. Dif-Pradalier, G. Falchetto, T. Gerbaud, V. Grandgirard, Ö. D. Gürcan, P. Hennequin, J. Kinsey, M. Ottaviani, R. Sabot, Y. Sarazin, L. Vermare, and R. E. Waltz, *Validating a quasi-linear transport model versus nonlinear simulations*, Nuclear Fusion **49**, 085012 (2009).
- [20] G. D. Conway, *Turbulence measurements in fusion plasmas*, Plasma Physics and Controlled Fusion **50**, 124026 (2008).
- [21] T. Hein, C. Angioni, E. Fable, and J. Candy, *Gyrokinetic study of the role of* β *on electron particle transport in tokamaks*, Physics of Plasmas **17**, 102309 (2010).
- [22] D. Told, *Gyrokinetic Microturbulence in Transport Barriers*, Ph.D. thesis, Universität Ulm (2012).
- [23] C. Lechte, *Investigation of the scattering efficiency in Doppler reflectometry by two-dimensional full-wave simulations*, IEEE Transactions on Plasma Science **37**, 1099 (2009).
- [24] C. Lechte, G. D. Conway, T. Görler, C. Tröster-Schmid, and the ASDEX Upgrade Team, *X mode Doppler reflectometry k-spectral measurements in ASDEX Upgrade: Experiments and simulations*, Plasma Physics and Controlled Fusion **59**, 075006 (2017).

Zonal flow collisionless damping and the residual in HSX

A zonal flow is a toroidally and poloidally symmetric $E \times B$ flow that can be driven by electric fields that develop from fluctuations of the plasma potential, such as is the case for most drift wave turbulence. The zonal flow does not drive transport itself, but by facilitating transfer of energy between radial wavenumbers it can regulate the linear instability and affect turbulence saturation. Strong zonal flows have been found to be important in configurations such as tokamaks or the reversed-field pinch, and they can affect turbulence saturation in stellarators as well. Sall Zonal flows are present in all nonlinear simulations in Chapter 3, and may be measured in the experiment under specific conditions. Experiments at TJ-II have demonstrated that zonal flow oscillations can be measured in the experiment and compared to linear gyrokinetic calculations, opening up a new aspect of experiment-simulation comparisons. A similar measurement at HSX could demonstrate validation of an important difference between the QHS and Mirror configurations. This chapter examines the collisionless decay of the zonal flow in quasisymmetry and has been published as Reference 13.

Linear zonal flow damping is often examined as a proxy for the full zonal flow evolution ¹⁴ and is used in models to predict turbulent transport. ^{15,16} The Rosenbluth-Hinton model ¹⁷ provides a zonal flow residual that describes the undamped part of the poloidal flow in a large-aspect-ratio tokamak. This undamped flow acts to saturate drift wave

turbulence, and the residual is used as a measure of the amplitude that zonal flows achieve in nonlinear simulations. In axisymmetric systems, this is commonly the case, and the residual is sometimes used as a proxy for the resulting turbulence saturation. ¹⁸ However, this is unlikely to be true if the collisionless damping to the residual is slow compared to the rate at which turbulence injects energy into the zonal flow. In non-axisymmetric devices, the radial drift of trapped particles can drive long-time damping and oscillations of the zonal flow, ^{14,19–22} as will be discussed in Section 4.1. These features can disassociate the zonal flow residual from saturated turbulence. Calculations in this chapter are linear and do not address the transfer of energy between modes, but can examine changes in the collisionless damping of the zonal flow.

Zonal flow damping and the driving turbulence both depend on aspects of the magnetic geometry, such as the rotational transform and trapped particle regions. Due to the large number of parameters that can describe the plasma boundary, the 3D shaping of stellarators offers a large parameter space to search for configurations that can benefit specific turbulence or zonal flow properties. Particularly in helical systems optimized to reduce neoclassical transport, stronger zonal flows may reduce turbulent transport. ²³ However, nonlinear simulations are expensive to include in an iterative optimization loop, and an efficient, general, linear proxy for turbulent transport would be a powerful tool. In order to obtain such a proxy, a thorough understanding of zonal flow dynamics in stellarators is required.

Zonal flows have been studied numerically in flux-tube geometry for the Large Helical Device²⁴ and Wendelstein 7-X,¹⁴ and in full-volume geometry for TJ-II,^{21,25} the Large Helical Device,²² and Wendelstein 7-X.^{22,26} As part of benchmarking gyrokinetic codes, full-volume linear calculations of zonal flow damping have been compared to local analytic theory.^{22,26–28} However, quasi-symmetric configurations are absent from previous studies, despite the expectation that a perfectly quasi-symmetric configuration will support an

undamped zonal flow similar to a tokamak.

In this chapter, the zonal flow damping is numerically calculated in flux-tube, flux-surface, and full-volume geometry representations for configurations of the Helically Symmetric eXperiment (HSX) and National Compact Stellarator eXperiment (NCSX). We look to understand how much geometry information is required for an accurate determination of the zonal flow time evolution. Although neoclassical transport and flow damping in quasi-symmetric stellarators is more similar to tokamaks than to classical stellarators, we show that the linear zonal flow response for a realistic but almost quasi-symmetric geometry still resembles a classical stellarator. Section 4.1 reviews collisionless zonal flow damping in non-axisymmetric equilibria and introduces the geometries and numerical tools used in this work. Section 4.2 identifies the differences in calculations of zonal flow damping in flux-surface, and flux-tube frameworks. In Section 4.3, calculations of zonal flow damping in flux tubes are shown to reproduce the zonal flow residual from full-volume calculations, but only for sufficiently long flux tubes. Section 4.4 presents results from the quasi-symmetric and broken-symmetry configurations of HSX and compares them to the NCSX zonal flow evolution.

4.1 Collisionless zonal flow damping

The Rosenbluth-Hinton model ¹⁷ quantifies the long-time linear response of the zonal flow to a large-radial-scale potential perturbation in a collisionless, axisymmetric system. The initial amplitude of the perturbation is reduced by plasma polarization and undergoes geodesic acoustic mode (GAM) oscillations before relaxing to a steady-state residual. The long-time residual zonal flow is defined as the ratio of the zonal potential in the long-time limit to the initial zonal potential. In a large-aspect-ratio tokamak, the residual amplitude

depends on the geometry as 17

$$\frac{\varphi_{t\to\infty}}{\varphi_0} = \frac{1}{1 + 1.6q^2/\epsilon_t^{1/2}} \,, \tag{4.1}$$

and can be interpreted as a measure of how strongly collisionless processes modify the zonal flow. Here, φ is the zonal potential, φ_0 is its initial amplitude, q is the safety factor, and $\epsilon_{\rm t}$ is the inverse aspect ratio of the flux surface of interest. The term $1.6q^2/\epsilon_{\rm t}^{1/2}$ results from the neoclassical polarization due to toroidally trapped ions. When the Rosenbluth-Hinton residual is high, the reduction of the zonal flow by polarization is small and the system can support strong zonal flows. When the residual is small, the zonal flow is significantly reduced by polarization, and the existence of strong zonal flows will depend on strong pumping from the turbulence.

Following Reference 29, HSX can often be treated as an equivalent tokamak with $q o q_{ ext{eff}}$ and $\epsilon \to \epsilon_{\rm h}$, the magnitude of the (4,1) field variation. For HSX, $q_{\rm eff} \approx 1/3$ and $\epsilon_{\rm h} \approx 0.14 r/a$, and the residual is predicted to be $\varphi/\varphi_0 \approx 0.6$. However, the zonal flow response in non-axisymmetric systems is significantly modified by neoclassical effects. The zonal flow amplitude after the polarization decay is no longer the Rosenbluth-Hinton residual. Instead, helical systems exhibit decay described by a timescale $\tau_c \sim 1/|k_x \bar{v}_{dr}|$ to reach a residual in a long-time limit. 30,31 Here, k_x is a radial wavenumber, and \bar{v}_{dr} is the bounce-averaged radial drift velocity. In an unoptimized device, \bar{v}_{dr} is large and the zonal flow will decay quickly to a residual, whereas a well-optimized device will have very long decay times. In a perfectly symmetric device, no long-time decay is observed, corresponding to the limit of infinitely long decay times. In this case, any geometry with finite radial particle drifts will decay to zero residual as $k_x \to 0$. Defining the residual as the zonal potential at some time shorter than $t \to \infty$ necessarily involves neoclassical effects, as discussed in Section 4.4. The long-time decay in helical systems could prevent any connection between the zonal flow residual and saturated turbulence. If a system takes a long time to decay, nonlinear energy transfer will become important before the decay has dissipated energy in the zonal

mode, and the residual no longer relates to the zonal flow amplitude in the quasi-stationary state.

Furthermore, an oscillation in the zonal flow is caused by neoclassical effects. ^{19,20} This oscillation is characterized by the radial drift of trapped particles, as opposed to the passing particle dependence of the GAM. Drifting trapped particles cause a radial current that interacts with the zonal potential perturbation to cause zonal flow oscillations. This oscillation is damped by Landau damping on trapped particles. The oscillation damping and frequency both increase with the radial particle drift, or equivalently, neoclassical transport. For an unoptimized device, the zonal flow oscillation is of higher frequency but damped more quickly. In a well-optimized device, the zonal flow oscillation is prominent due to the small damping, but the oscillation frequency is small compared to characteristic inverse time scales in fully developed turbulence. In a perfectly symmetric device, the zonal flow oscillation vanishes.

For both stellarators and tokamaks, the zonal flow residual depends on the radial wavenumber of the zonal perturbation, but this dependency is stronger in stellarators than in tokamaks. $^{26,32-34}$ In this chapter, radial wavenumbers are normalized as $k_x\rho_s$, where ρ_s is the ion sound gyroradius. The numerical calculation of the zonal flow residual in a tokamak matches the Rosenbluth-Hinton residual as k_x approaches zero. However, any geometry with finite radial particle drifts causes the zonal flow residual to vanish as $k_x \to 0$, although the long-time decay to that residual can be very slow in a well-optimized device.

Zonal flow oscillations, zonal flow damping, and even the zonal flow residual are further modified by the inclusion of a radial electric field. ^{35–37} The radial electric field drives coupling across field lines in the poloidal direction, and it is likely this would be visible in the difference between flux-tube and flux-surface calculations. Radial electric fields are not included here, and their effect on calculations in quasi-symmetric devices, or in local and global geometry representations, is left for future work.

Simulations in local and global geometry representations

A zonal flow is a toroidally and poloidally symmetric potential perturbation, and the local geometry anywhere on the surface can potentially be important to determine its response. In an axisymmetric geometry, a field line followed for one poloidal transit samples all unique magnetic geometry on a surface, as would any other field line on the same surface. However, different field lines in a stellarator do not generally sample the same geometry. Local geometry variations that may be important for the zonal flow may not be sampled by a given flux tube. In order to investigate the representativeness of a flux tube in stellarators, we examine flux-surface calculations along with multiple flux tubes on a surface, and extend flux tubes for multiple poloidal turns. Extended flux tubes follow a single field line, but are terminated after some integer number of 2π transits of the poloidal angle, and are identified by $n_{\rm pol}$ for a flux tube of $\theta = [-n_{\rm pol}\pi, n_{\rm pol}\pi]$. The effect of reduced sampling by flux tubes is seen by comparison between different flux tubes on a surface and to fluxsurface and full-volume calculations. The zonal flow also has a finite radial width, and these reduced frameworks are compared to full-volume calculations to highlight where local representations are insufficient with respect to zonal flow dynamics. Simulations here use a single ion species with adiabatic electrons for computational economy. The zonal flow oscillation frequency for multi-species plasmas with kinetic electrons can be inferred from a straightforward relation, see Reference 25. All time units are normalized in units of $a/c_{\rm s}$, where a is the minor radius, and $c_{\rm s}$ is the ion sound speed.

Full-volume geometry

Full-volume calculations of zonal flow damping provide the most complete representation of geometry effects on the zonal flow. In this work, these calculations are carried out with the δf gyrokinetic particle-in-cell code EUTERPE. ^{38,39} The details of the zonal flow calculation are discussed in References 22 and 26. The full-volume geometry of the fields

is represented in real space using the PEST magnetic coordinates, 40 where ϕ is the toroidal angle, s is the toroidal normalized flux, and θ^* is the poloidal angle defined such that field lines are straight. The real rotational transform profile of each device, shown in Figure 4.3, is used in the simulation. Flat density and temperature profiles are specified across the minor radius with $n=10^{19}~{\rm m}^{-3}$ and $T_{\rm i}=T_{\rm e}$. We perform several simulations with different values of $T_{\rm i}=T_{\rm e}$ in the range 50, 100, 400, 1600, 6400 eV. For these temperatures the inverse normalized Larmor radius $a/\rho_{\rm s}$ is in the range (63-710) for NCSX and (30-169) for HSX configurations. The radial resolution of the simulations and the number of markers are increased as to properly resolve the zonal flow structure while keeping the ratio of modes to number of markers constant. The plasma potential is computed from the charge density of particles in a set of flux surfaces using B-splines. The potential is Fourier-transformed at each flux surface and can be filtered in Fourier space. From the Fourier spectrum, only the (0,0) component is of interest for zonal flow calculations and is extracted at individual flux surfaces.

The linear properties of the zonal flow are extracted from the time trace of the zonal component. These linear zonal flow relaxation simulations are initialized with a flux-surface-symmetric perturbation to the ion distribution function. The initial condition has a Maxwellian velocity distribution and a radial structure such that a perturbation to the potential containing a single radial mode, $\phi \propto \cos(k_s s)$, is produced after solving the quasi-neutrality equation. The simulation is linearly and collisionlessly evolved, and the time evolution of the zonal potential at fixed radial positions is recorded. A long-wavelength approximation valid for $k_x \rho_s < 1$ is used to simplify the quasi-neutrality equation. The function $\Gamma_0(\mathbf{x}) = e^{-\mathbf{x}}I_0(\mathbf{x})$ is approximated as $\Gamma_0(\mathbf{x}) \sim 1 - \mathbf{x}$, where $\mathbf{x} = k_x^2 \rho_s^2$ and I_0 is the modified Bessel function. Then the quasi-neutrality equation for adiabatic electrons reads

$$q_{\rm i}\langle n_{\rm i}\rangle - \frac{en_0(\varphi - \{\varphi\}_s)}{T_{\rm e}} = -\nabla \frac{m_{\rm i}n_0}{B^2} \nabla_\perp \varphi$$
, (4.2)

where n_0 is the equilibrium density, B is the magnetic field, $\langle n_i \rangle$ is the gyroaveraged ion density, $T_{\rm e}$ is the electron temperature, and e and $m_{\rm i}$ are the electron charge and the ion mass, respectively. The $\{\}_s$ brackets represent a flux surface average.

Linear zonal flow relaxation simulations are less numerically intensive than turbulence simulations, 41 where many modes are allowed to evolve and interact in a nonlinear simulation, and time steps are shorter to account for fast phenomena. Fewer Fourier modes are required for zonal flow calculations, where there are no temperature and density gradients to drive turbulence and only a single mode is examined, as opposed to the mode spectrum of a nonlinear simulation. For a zonal flow calculation, a larger number of modes would only increase the numerical noise and require more computational resources. However, a long simulation time is required to extract the long-time properties of the zonal flow evolution, which prohibits the use of full-volume calculations in an optimization loop. Simulations presented in this work are carried out retaining 6 poloidal and toroidal modes, with radial resolutions ranging from 24 to 64 points to account for the radial structure of the mode, and from 50×10^6 to 200×10^6 markers. These resolutions are similar to those in previous EUTERPE zonal flow calculations. 22,26

Flux-tube and flux-surface geometry

The gyrokinetic δf continuum code Gene, ³⁴ introduced in Section 3.1, is used for calculations of the zonal flow decay in flux-tube and flux-surface representations. All flux-tube and flux-surface calculations in this work use the s=0.5 flux surface, and are compared to results from full-volume calculations about this surface. Gene uses non-orthogonal coordinates x in the radial direction, y in the flux surface, and z along the field line. In a Gene flux tube, a spectral representation is used for the x and y directions, while the z direction is in real space. When the flux tube is centered on the outboard midplane, the PEST⁴⁰ coordinate α is also a toroidal coordinate of the center point of the flux tube. For

 $k_y=0$ zonal modes, boundary conditions in x,y, and z are periodic. In axisymmetric systems, a flux tube of one poloidal turn samples all unique geometry on the flux surface. In a non-axisymmetric system, a flux tube does not necessarily close upon itself. The standard approach to using flux tubes in stellarators does not require true geometric periodicity of the flux tube. A stellarator-symmetric flux tube, or one that is symmetric about the midpoint z=0, provides continuous, but not necessarily smooth, geometry at the flux tube endpoints. However, $k_z=0$ modes, such as zonal flows, may be sensitive to the geometry at this boundary. True geometric periodicity requires that $qn_{\rm pol}N$ is an integer, where N is the toroidal periodicity of the geometry. We treat the flux tube length $n_{\rm pol}$ as a parameter subject to convergence, and show in Section 4.3 that the choice of a truly periodic or a standard stellarator symmetric flux tube does not affect the outcome of the studies conducted in this work.

A flux-surface representation discretizes the y direction in real space instead of Fourier space. The z-direction is aligned to the magnetic field, and field lines are followed for one poloidal turn. Calculations here use 64 y points equally spaced in α . A flux-tube calculation only includes the local magnetic geometry coefficients along the field line, while a flux-surface calculation captures the variation in geometry with α . The radial computational domain is set by the magnetic shear of the configuration. The configurations considered here have a small magnetic shear, setting the minimum radial wavenumber for flux-surface calculations to $k_{x,\min} = 0.009$ in HSX and $k_{x,\min} = 0.158$ in NCSX. Calculations at an appropriate k_x to compare to flux-tube and full-volume calculations proved unfeasible in HSX due to the very small $k_{x,\min}$. Therefore, flux-surface calculations are only presented in NCSX.

The zonal flow damping, and resulting residual and oscillations, is calculated by initializing a flux-surface-symmetric impulse to the distribution function at a single radial mode and allowing the amplitude to collisionlessly decay due to classical and neoclassical

polarization without further energy input. In Gene, the zonal perturbation is implemented by initializing only one $k_x \neq 0$, $k_y = 0$ mode. In a Fourier representation, the wavenumber is explicit, and a long-wavelength approximation is not used. The perturbation is introduced in the density with Maxwellian velocity space, which produces an equivalent potential perturbation to that used in EUTERPE. Note that for the present case of adiabatic electrons, the two initial conditions discussed in Reference ⁴³ are identical.

Numerical calculations for linearly stable systems without dissipation may have to contend with numerical recurrence phenomena. Such recurrence, which results from a reestablishment of phases from the initial condition and concomitant unphysical temporary increase in amplitudes, can be eliminated by including numerical spatial or velocity hyperdiffusion. However, numerical diffusion is not an appropriate solution in nearly quasisymmetric stellarators, as calculation times are very long and even a small amount of diffusion will cause significant damping of the zonal flow residual. To solve the problem, the parallel velocity space grid spacing Δv_{\parallel} can be decreased sufficiently that the recurrence time, $\tau_{\rm rec} = 2\pi/(k_z\Delta v_{\parallel})$, exceeds the duration of the simulation. In the present work, most flux-tube calculations use $N_{v\parallel} > 256$ to discretize the velocity space spanning $v_{\parallel} = [-3v_{Ti}, 3v_{Ti}]$, leading to $\Delta v_{\parallel} = 0.015 \ v_{Ti}$. Here, $v_{Ti} = (2T_i/m_i)^{1/2}$ is the ion thermal velocity. We take k_z to be the wavenumber of the periodicity of the magnetic structure, as seen in Figure 4.2, which leads to $k_z \approx 0.4 \ a^{-1}$ in HSX and $k_z \approx 0.34 \ a^{-1}$ in NCSX. For $N_{v\parallel} = 256$, $\tau_{\rm rec} \approx 670 \ a/c_{\rm s}$ in HSX and $\tau_{\rm rec} \approx 790 \ a/c_{\rm s}$ in NCSX. This effect is seen in Figure 4.13. For $N_{v\parallel} = 384$, $\tau_{\rm rec} > 1000 \ a/c_{\rm s}$ in both configurations.

The HSX and NCSX geometries

The zonal flow response is studied by means of flux-tube, flux-surface, and full-volume gyrokinetic simulations in the Helically Symmetric eXperiment (HSX)⁴⁶ and the National Compact Stellarator eXperiment (NCSX).⁴⁷ VMEC⁴⁸ is used to calculate the HSX and NCSX

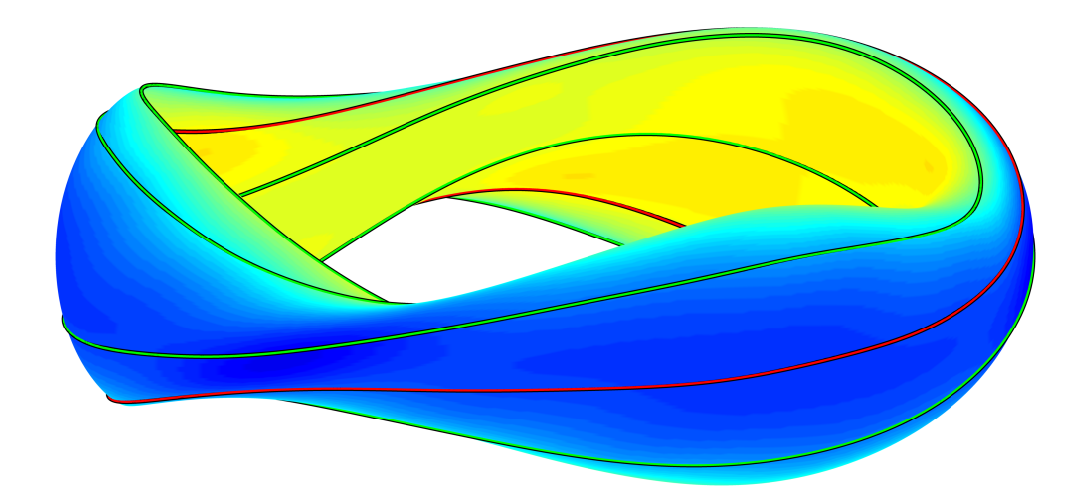


Figure 4.1: A flux surface and $\alpha=0$ flux tube for the s=0.5 surface of the NCSX configuration. Colors correspond to |B|, where blue is the minimum field strength. A flux tube of one poloidal turn is shown in red, and one of 4 poloidal turns in green.

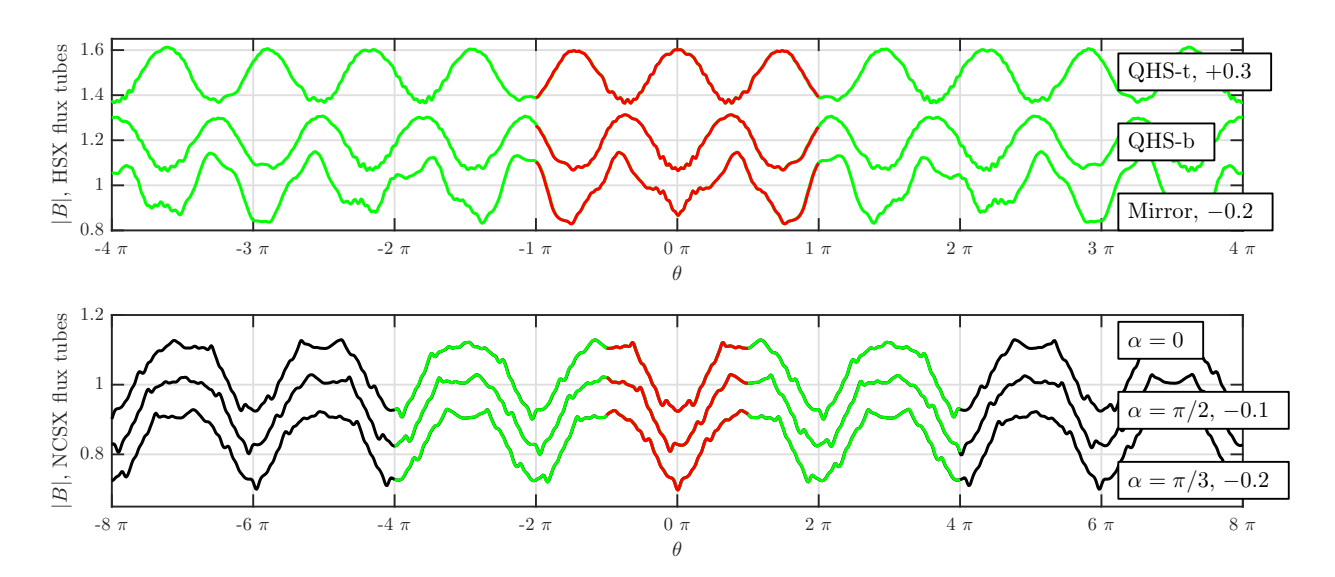


Figure 4.2: Comparison of |B| in the various flux tubes from HSX and NCSX. A flux tube of length $n_{\rm pol}=1$ is plotted in red, $n_{\rm pol}=4$ in green, and $n_{\rm pol}=8$ in black. Curves are shifted to avoid overlap.

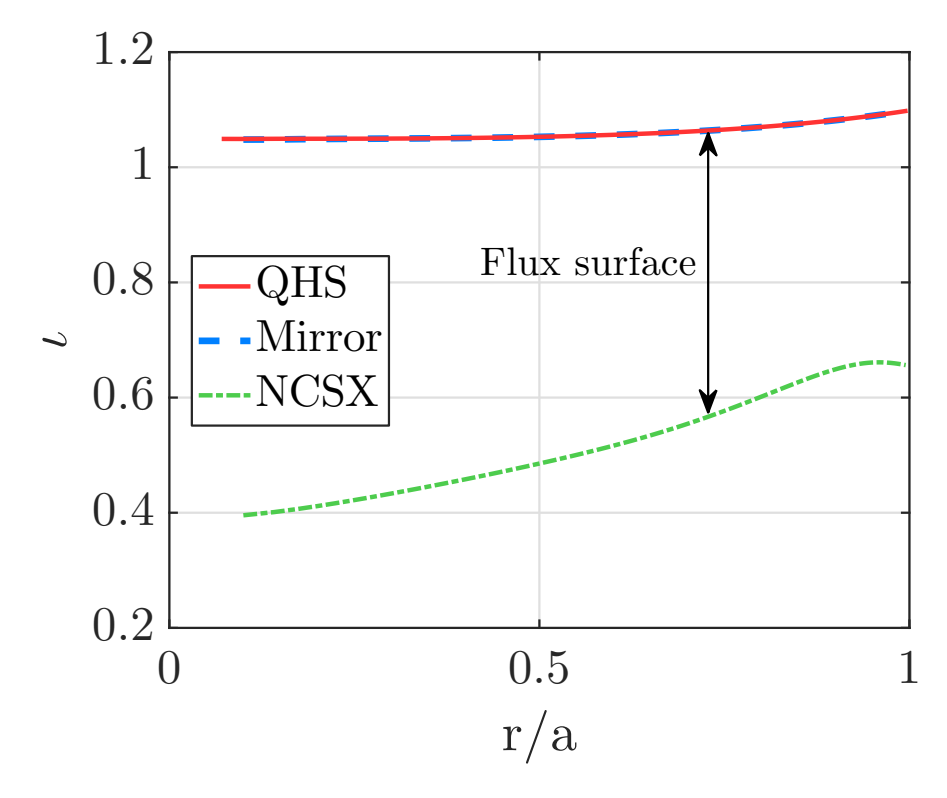


Figure 4.3: The iota profile in the three configurations studied. The radial location of flux-tube and flux-surface calculations is marked with the arrow. The iota profile in the HSX QHS and Mirror configurations shows a negligible difference.

equilibria. The QHS and Mirror configurations of HSX are introduced in Section 1.2. There are two unique flux tubes centered on the outboard midplane that are symmetric about the midpoint z=0. The QHS-b "bean" flux tube ($\alpha=0$) is centered on the outboard midplane of the bean-shaped cross section, where it is the low-field and bad-curvature side. The QHS-t "triangle" flux tube ($\alpha=\pi/N$, with N=4 for HSX) is centered on the outboard midplane in the triangle cross section, where it is the high-field and good-curvature side in HSX.

The NCSX configuration was also optimized for neoclassical transport, but is a three-period device designed for quasi-axial symmetry. The equilibrium used here has total normalized plasma pressure $\beta \approx 4\%$. In the NCSX configuration, we use the flux tubes symmetric about the midpoint z=0 ($\alpha=0$ and $\alpha=\pi/N$, with N=3 for NCSX), as well

as one non-symmetric flux tube ($\alpha=\pi/2$). The radial particle drift for the surface at s=0.5 is between that of the QHS and Mirror configurations of HSX. The rotational transform in NCSX is roughly half that in HSX, as seen in Figure 4.3. The difference in rotational transform means that the part of the surface sampled by a flux tube is very different. In Figure 1.2, the multiple turns of a flux tube in HSX cluster together in a band around the device. In Figure 4.1, the multiple turns of a flux tube in NCSX spread out across the surface, potentially sampling larger variation in a shorter flux-tube length. However, the flux tube does not allow poloidal communication between turns, and poloidally neighboring geometry can only affect the zonal flow damping in a flux-tube calculation through parallel physics.

Fitting zonal flow oscillations and residuals

The zonal flow decay in a stellarator includes additional long-time damping and zonal flow oscillations as compared to the tokamak case. Previous studies have commonly focused on the zonal flow residual or oscillation frequency, but there is also the short-time damping due to the polarization drift, additional long-time damping due to the polarization of trapped particles, the GAM oscillation, and the zonal flow oscillation amplitude and damping. Following Monreal, ²² curve fitting is used to extract the residual and parameters of the zonal flow oscillation. The time evolution during the post-GAM phase is described by,

$$\frac{\varphi_k(t)}{\varphi_k(0)} = A_{\rm ZF} \cos(\Omega_{\rm ZF} t) e^{-\gamma_{\rm ZF} t} + R_{\rm ZF} + C e^{-\gamma} . \tag{4.3}$$

The zonal flow oscillation is parameterized by an amplitude $A_{\rm ZF}$, oscillation frequency $\Omega_{\rm ZF}$, and damping rate $\gamma_{\rm ZF}$. The long-time decay follows an algebraic decay according to Reference²⁰, but is well approximated by an exponential decay $C{\rm e}^{-\gamma}$ to avoid an abundance of fitting parameters. The zonal flow residual is $R_{\rm ZF}$. The evolution of normalized zonal potential and normalized zonal electric field are equivalent for a zonal potential with only

a single k_x^{22} . However, in practice, the zonal electric field is preferred in global EUTERPE simulations to simplify the fitting.

We are primarily interested in the zonal flow oscillation here, not the GAM. The damping of the GAM increases with decreasing rotational transform. 31 In HSX, the rotational transform is about one and the GAM is damped on time scales of the order $10~a/c_s$. GAM oscillations are more apparent in NCSX calculations, as the rotational transform is about twice that in HSX, but are still damped quickly compared to the zonal flow oscillations. Fitting starts after the GAM oscillations have damped away to avoid further complexity in curve fitting. The zonal flow oscillation is Landau-damped by trapped particles, and depends on the radial drift off of the flux surface. 20 Neoclassically optimized devices can have long-lived zonal flow oscillations as neoclassical transport is reduced, which also reduces the oscillation frequency to well below the GAM frequency. In the configurations examined here, fitting the zonal flow oscillations is important to accurately fit the zonal flow residual.

4.2 Comparison of local and global calculations

The NCSX configuration is quasi-axisymmetric, which, among three-dimensional geometries, most closely resembles a tokamak. As discussed in Section 4.1, the zonal flow residual as $k_x \to 0$ is a key difference between symmetric and non-symmetric systems. The time traces for full-volume, flux-surface, and flux-tube simulations are fitted to extract the zonal flow residual plotted in Figure 4.4. A discussion of different flux tubes in the NCSX configuration is provided in Section 4.3. In NCSX, the zonal flow residual goes to zero for small k_x , just as it does for classical stellarators. The limit as $k_x \to 0$, as well as a peak residual around $k_x \rho_s \approx 0.5$, is reproduced in all three geometry representations. However the amplitude of the residual differs between the local and global representations

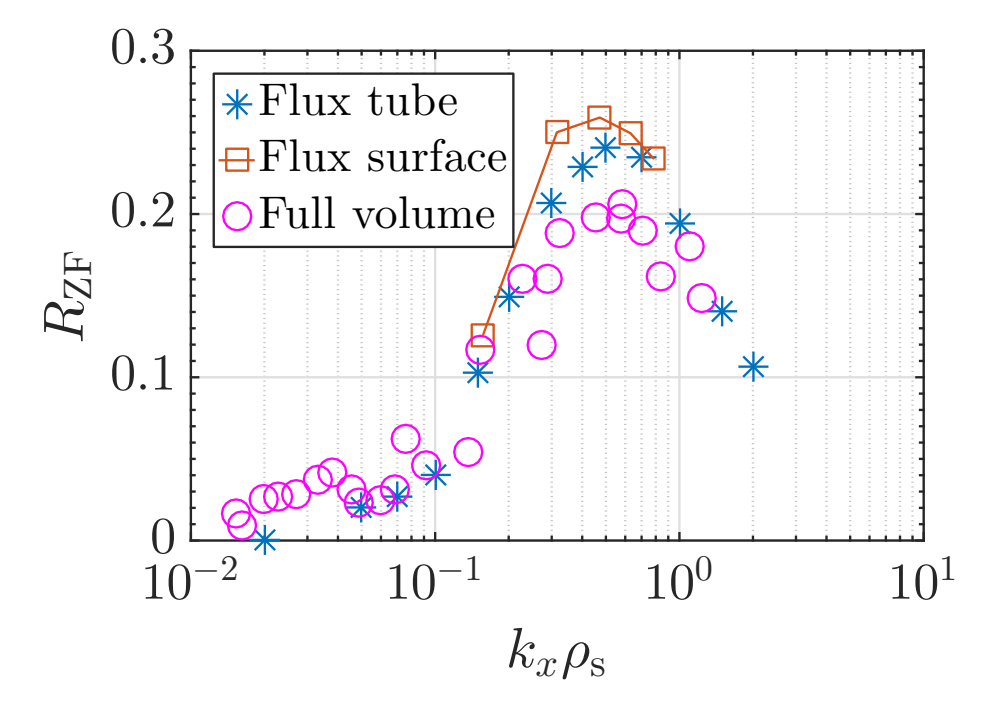


Figure 4.4: The zonal flow residual in the NCSX configuration from flux-tube, flux-surface, and full-volume calculations. Local and global representations largely show good agreement on the k_x dependence of the residual, with moderate deviations observed at very small $k_x \rho_s$ and near the peak residual, as expected from model limitations.

particularly for very small k_x . In the full-volume calculations, the peak of the residual is slightly lower, while the smallest k_x support a larger residual than the flux-tube calculations. A long-wavelength approximation valid for $k_x\rho_s<1$ is used in the global simulations, which may be approaching its limit of validity towards the peak. Without flux surface calculations at small k_x , we cannot constrain the physical cause for differences between full-volume and flux-tube results. Coupling between surfaces may be occurring, but the same disagreement is not seen for HSX configurations in Figure 4.16. More importantly, the flux-surface approximation will break down when scales are large enough to involve profile effects, and the smallest k_x values examined approach the machine size. Thus the observed discrepancies are to be expected given the limitations of the frameworks.

The short-time evolution of the zonal flow is arguably more important than the long-

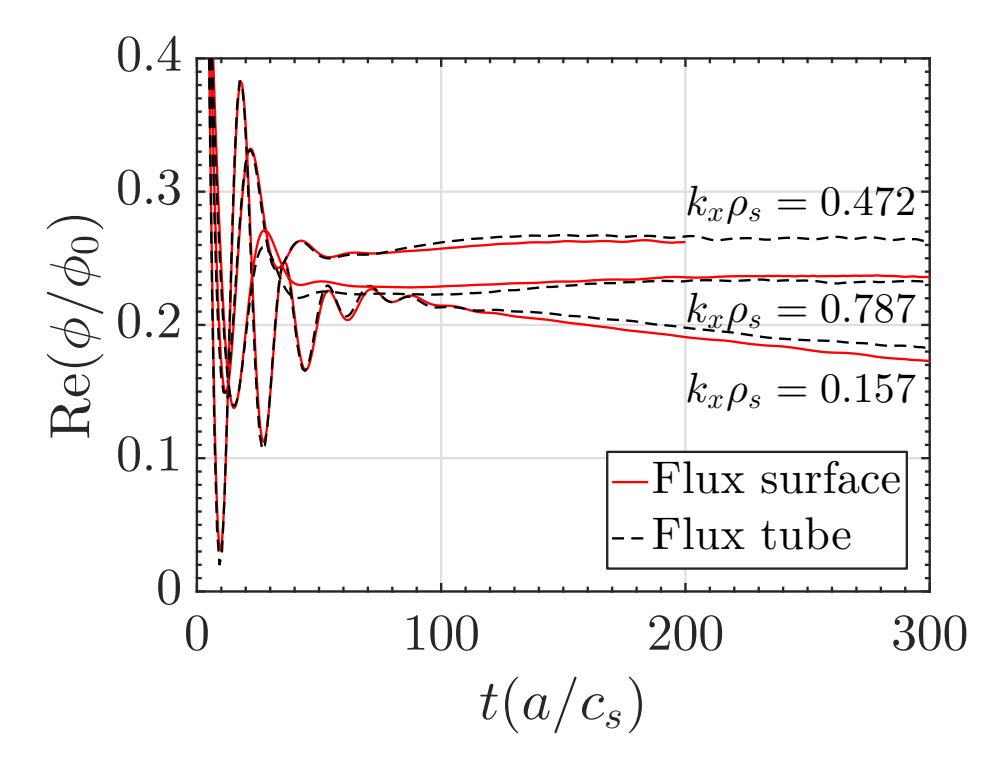


Figure 4.5: Comparison of zonal flow evolution in NCSX for flux-surface and flux-tube calculations. Good agreement is found for the initial polarization drift, the GAM oscillations and damping, and the long-time decay. Flux-tube calculations here use $n_{\rm pol}=4$.

time zonal flow residual for turbulence saturation, as turbulent correlation times are on the order of $\tau \sim 10a/c_{\rm s}$. The time traces for several k_x are compared in Figure 4.5 for the flux-surface and flux-tube calculations, and in Figure 4.6 for the full-volume and flux-tube calculations.

Figure 4.5 shows that there is little difference between flux-tube and flux-surface calculations. This only holds true for long enough flux tubes as measured by convergence in $n_{\rm pol}$, as will be discussed in Section 4.3. Evidently, the $k_y=0$ mode in the flux tube samples sufficient geometry through the parallel domain that the same physics is retained as for the true flux-surface average.

In Figure 4.6, zonal flow oscillations can be identified for the smallest k_x , and there is significant long-time decay of the zonal flow for mid- k_x . The zonal flow decay in realistic

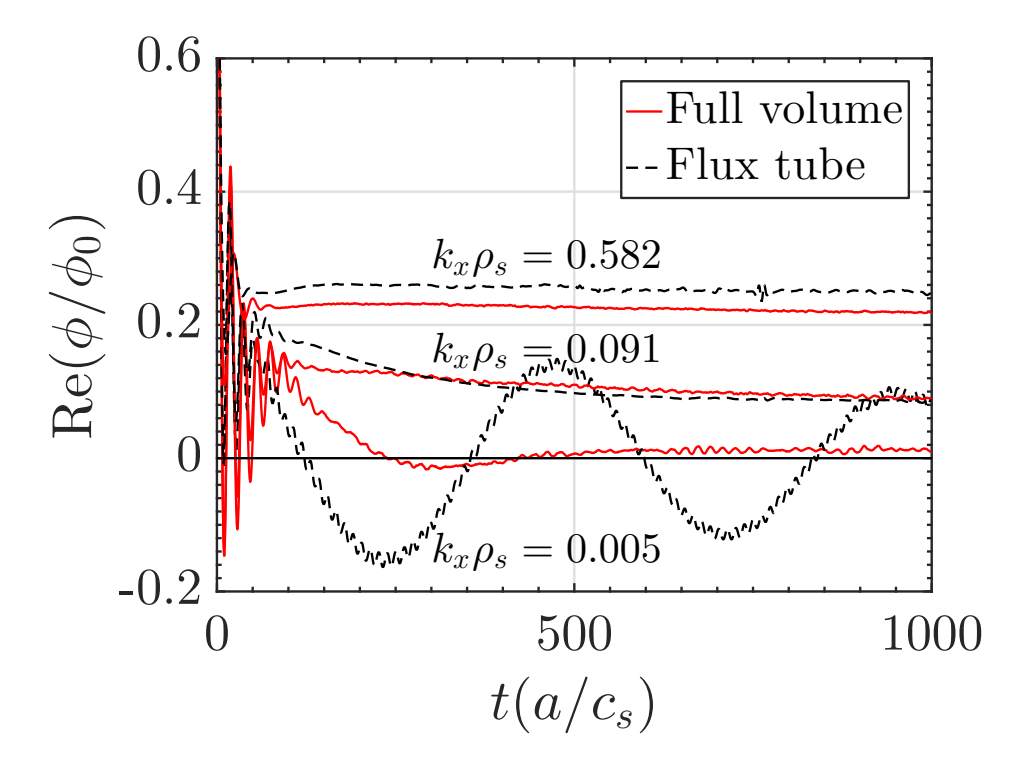


Figure 4.6: Comparison of zonal flow evolution in NCSX for full-volume and flux-tube calculations. Three different k_x demonstrate differences in the residual, long-time decay rate, and zonal flow oscillation damping. Calculations agree on the GAM frequency, and residuals match at $k_x \rho_s = 0.091$. Flux-tube calculations here use $n_{\rm pol} = 4$.

NCSX geometry is characteristic of that in a un-optimized stellarator. The difference between flux-tube and full-volume calculations is much more significant than that between flux-tube and flux-surface calculations. At high $k_x \rho_s \gtrsim 0.5$, the short-time decay due to the polarization drift reduces the zonal flow to a smaller value in the full-volume calculation. There is no difference in the long-time decay, and so the zonal flow residual is smaller in the full-volume calculation at high k_x . The zonal flow residual converges during the long-time evolution for moderate $k_x \rho_s \approx 0.1$, but with slightly different decay properties in the two calculations. Again, the zonal flow initially decays to a smaller amplitude in the full-volume calculation, but the long-time decay is larger in the flux-tube calculations such that the residual zonal flow is the same. The GAM frequency is consistent between full-volume and flux-tube calculations but the amplitude is slightly smaller, or, alternatively,

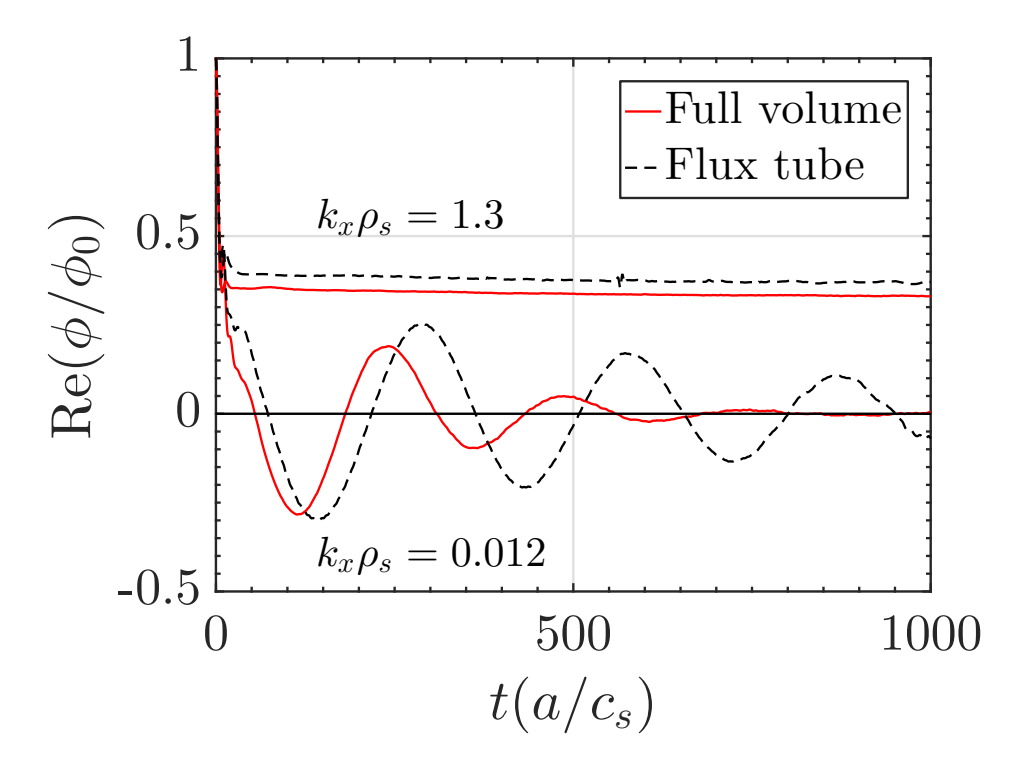


Figure 4.7: Comparison of zonal flow evolution in HSX Mirror configuration for full-volume and flux-tube calculations. Two different k_x demonstrate differences in the residual and the zonal flow oscillation frequency and damping, but similar time evolution at corresponding k_x . Flux-tube calculations here use $n_{\rm pol}=4$.

the GAM oscillation damping is slightly stronger in the flux-tube calculation. In Figure 4.6, zonal flow oscillations are visible only for very small $k_x \rho_s << 0.1$. Zonal flow oscillations that are sustained in the smallest- k_x flux-tube calculations are quickly damped out in the full-volume calculation. We include flux-tube and full-volume calculations in the HSX Mirror configuration in Figure 4.7, where the zonal flow oscillations are not damped as quickly and can be more easily compared. At higher k_x , there again exists only a small displacement of the residual, whereas on very large scales the full-volume calculation shows significantly larger damping of the zonal flow oscillations, but also a slight increase in the oscillation frequency.

Overall, good agreement is observed between flux-tube and flux-surface calculations in the NCSX geometry. Full-volume calculations differ at system-size scales where global

effects become important but otherwise show fair agreement with radially local frameworks. This agreement only holds for sufficiently long flux tubes, as is discussed in the next section.

4.3 Zonal flow response in different flux tubes

The calculation of the zonal flow response in a flux tube is computationally cheaper compared with flux-surface or full-volume calculations, but is limited to the geometry information from a single field line. As the zonal flow is toroidally and poloidally symmetric and its dynamics depend on both bounce averages of the trapped particle radial drift and flux-surface averages over the quasineutrality equation,²⁶ a measurement of the zonal flow must be the same for any point on the flux surface. In a general stellarator flux tube, each $\theta^* = [-\pi, \pi]$ flux tube is unique and contains different geometry information. True

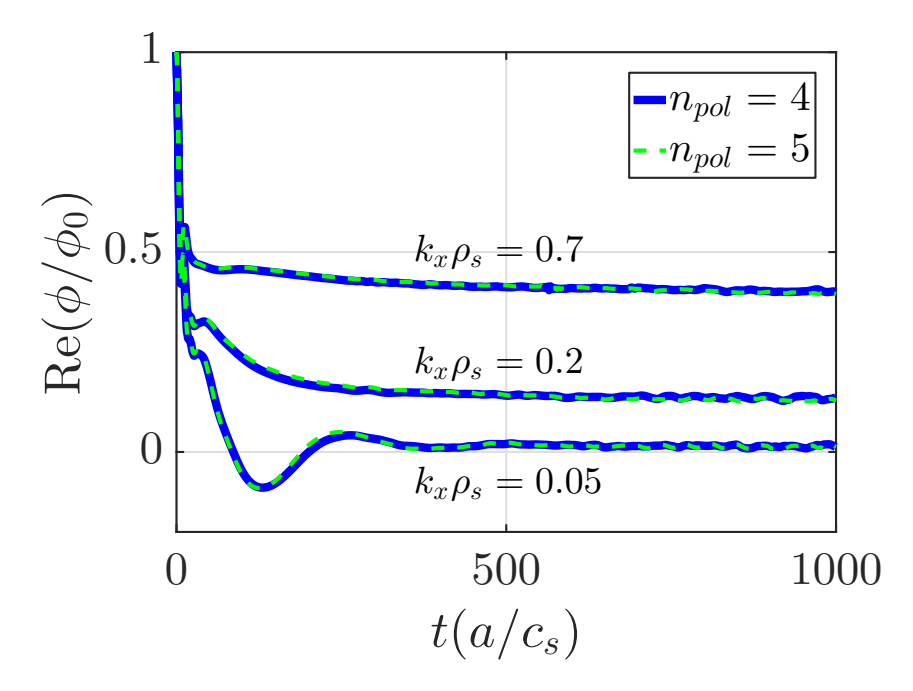


Figure 4.8: Zonal flow evolution for $k_x \rho_s = [0.05, 0.2, 0.7]$ with $n_{\rm pol} = [4, 5]$ in the HSX Mirror configuration. The value of $q n_{\rm pol} N$ is 14.96 for $n_{\rm pol} = 4$ and 18.7 for $n_{\rm pol} = 5$. Convergence is seen in $n_{\rm pol}$ despite the non-integer value of $q n_{\rm pol} N$.

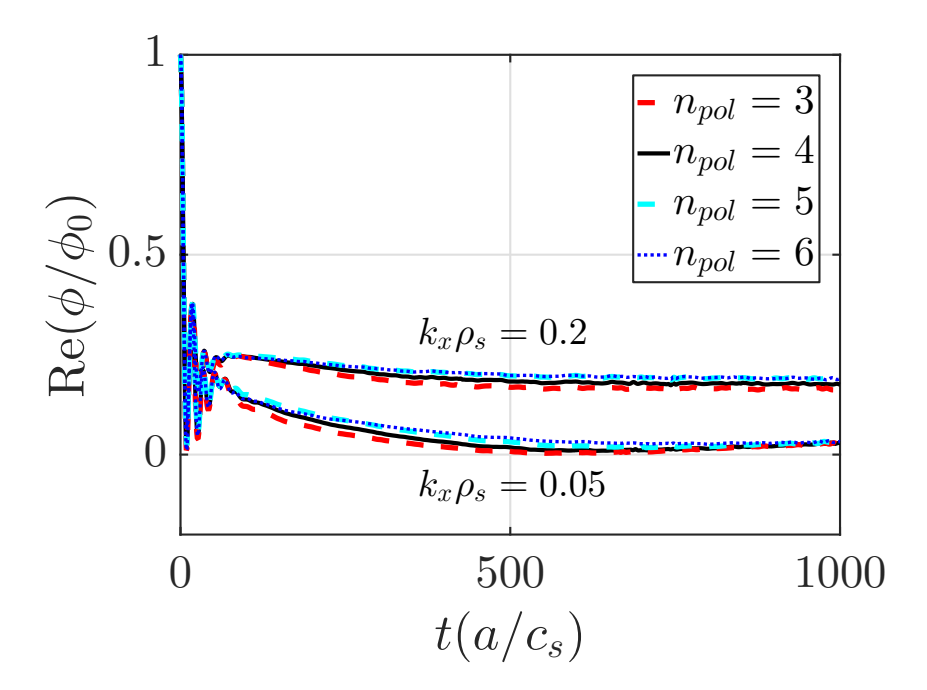


Figure 4.9: Zonal flow evolution from flux tubes at s=0.54 in NCSX, where $q=0.5714\approx 7/4$. The condition $qn_{\rm pol}N=21$ for $n_{\rm pol}=4$. However, convergence is achieved for $n_{\rm pol}=[3,5,6]$, where $qn_{\rm pol}N=[15.75,26.25,31.5]$.

geometric periodicity requires that $qn_{\rm pol}N={\rm integer}$, as discussed in Section 4.1. With q=0.9413 in QHS and q=0.9349 in Mirror, the HSX flux tubes at $n_{\rm pol}=4$ closely approach the integer condition with $qn_{\rm pol}N=15.06$ in the QHS configuration and $qn_{\rm pol}N=14.96$ in the Mirror configuration. The $n_{\rm pol}=8$ flux tube in NCSX is also close to an integer, with $qn_{\rm pol}N=42.93$. For the HSX Mirror case shown in Figure 4.8, the same results are obtained within the usual convergence thresholds for $n_{\rm pol}=4$ and $n_{\rm pol}=5$, where $qn_{\rm pol}N=18.7$. Similarly, the condition is matched much more closely in Figure 4.9 by minimally changing the radial position for an NCSX flux tube to s=0.54, such that $q=0.5714\approx 7/4$ and $qn_{\rm pol}N=21$ for $n_{\rm pol}=4$. Calculations at $n_{\rm pol}=3,5,6$ again converge to the $n_{\rm pol}=4$ flux tube despite the non-integer value of $qn_{\rm pol}N$. This is consistent with Reference 42 which showed that zonal flow residuals converged for a long enough flux tube, regardless of the boundary condition.

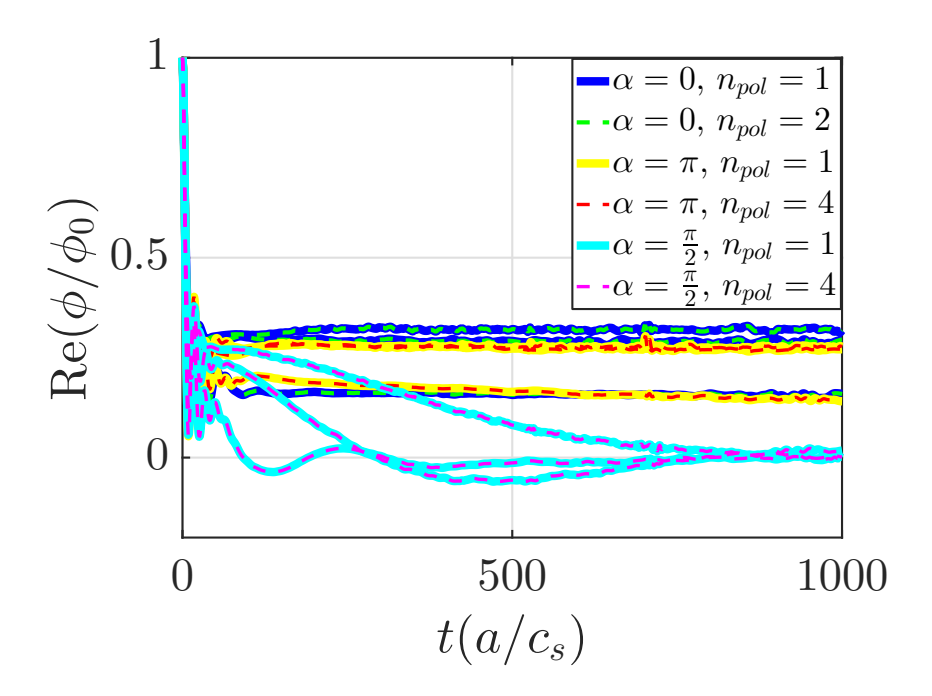


Figure 4.10: Zonal flow evolution from flux tubes at s=0.63 in NCSX, where q=1.66=5/3. The condition $qn_{\rm pol}N$ is an integer for any value of $n_{\rm pol}$. However, the zonal flow decay in different flux tubes does not converge.

Finally, the integer condition is exactly satisfied at certain rational surfaces, such as s=0.63 in the NCSX configuration. Here, $\iota=0.6$ and q=5/3, and the condition $qn_{\rm pol}N=5n_{\rm pol}$ is an integer for any $n_{\rm pol}$. In these flux tubes, the zonal flow evolution in a single flux tube does not change as $n_{\rm pol}$ is increased, as shown in Figure 4.10. Because the integer condition is met at $n_{\rm pol}=1$, all available geometry on that field line is included, and extended flux tubes do not add information to the calculation. While convergence is reached in a single flux tube, the zonal flow evolution does not converge between flux tubes. These field lines do not sample enough of the surface to approximate a flux-surface average. This makes it clear that, in this situation, convergence in a flux tube is specific to the configuration and local geometry of the calculation. However, if the time dependence of the zonal flow is similar in different flux tubes, it is likely that full-surface effects are limited. In this section, we compare calculations in different flux tubes on the same surface,

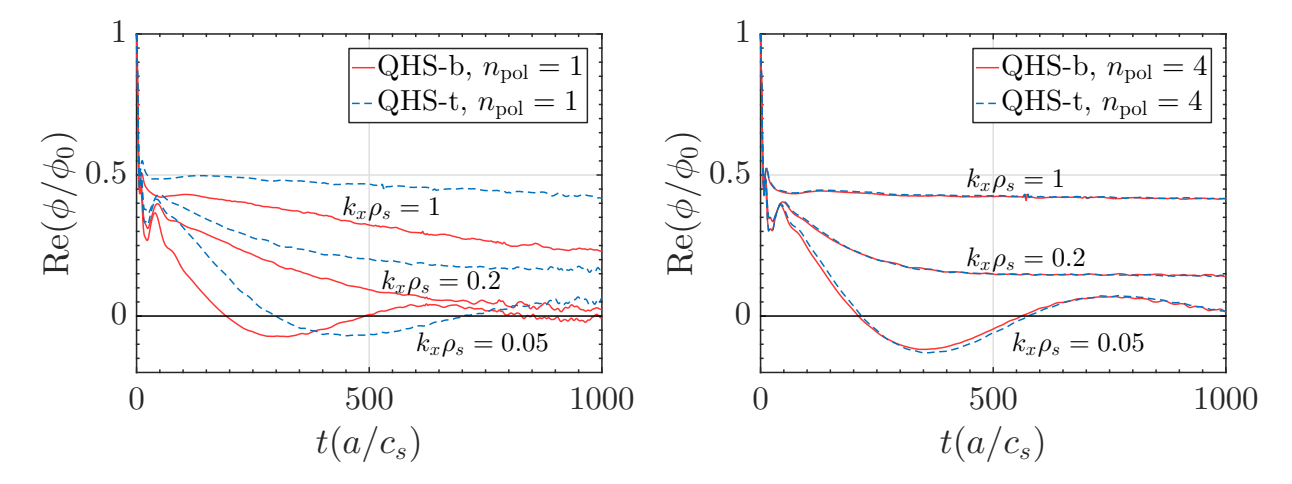


Figure 4.11: Zonal flow timetrace from two flux tubes with length of one poloidal turn (left) and four poloidal turns (right). Decay times, zonal flow oscillations, and residual agree when flux tubes are extended.

and extend those flux tubes to see convergence on the surface and capture all relevant zonal flow effects.

Comparison of response in two flux tubes in QHS

Unlike a tokamak, two flux tubes on the same surface in a stellarator do not share the same geometry information. Here, we examine the zonal flow response in two different flux tubes of the QHS configuration of HSX. The QHS-b "bean" flux tube is centered at $\alpha=0$, while the QHS-t "triangle" flux tube is centered at $\alpha=\pi/4$. On the left in Figure 4.11, calculations of zonal flow damping with a flux-tube length of one poloidal turn show large differences between the two flux tubes. The zonal flow amplitude and decay rate are different, and at small k_x , the zonal flow oscillation frequency is larger in the QHS-b flux tube. Neither individual $n_{\rm pol}=1$ flux tube matches the zonal flow damping in a full-volume calculation.

Geometry information can be added by extending the flux tube to multiple poloidal turns along the field line. The time traces from both flux tubes match when the flux tube

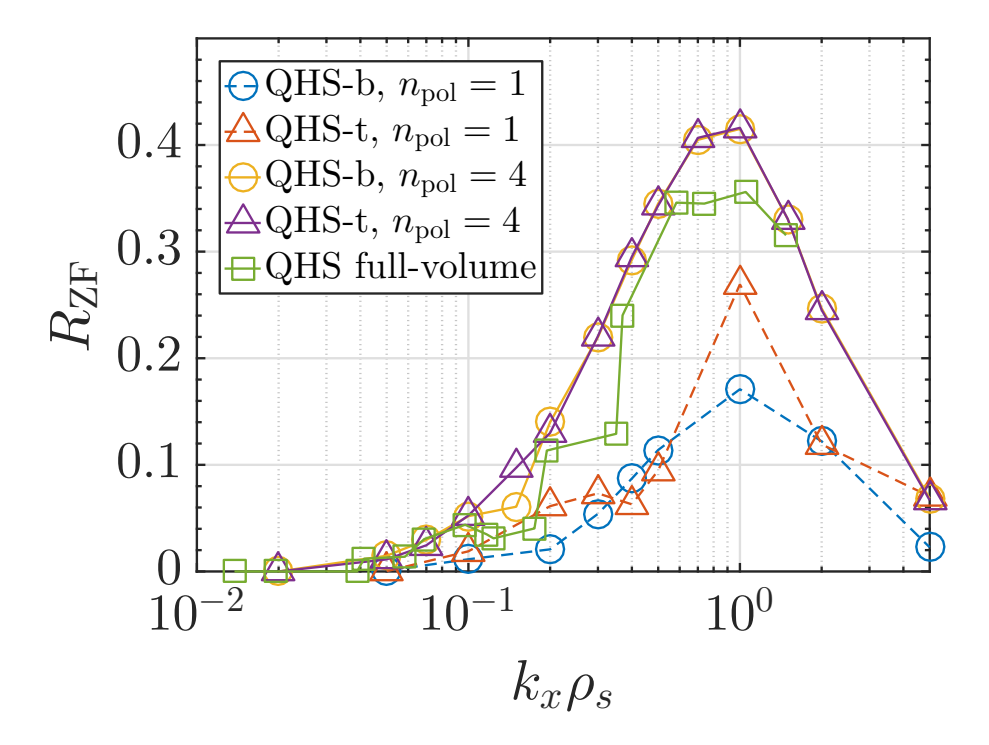


Figure 4.12: Zonal flow residuals for the QHS-b and QHS-t flux tubes. Shown are results for full-volume geometry and for flux tubes of two different lengths. Only the residuals from the extended flux tubes show agreement.

is extended to 4 poloidal turns on the right of Figure 4.11. Furthermore, the same holds true for the zonal flow residual across the k_x spectrum in Figure 4.12. At $n_{\rm pol}=1$, both the "bean" and the "triangle" flux tubes demonstrate much more decay of the zonal flow residual than the full-volume calculation. As results from both flux tubes change as the flux tube is extended, neither flux tube has enough information to calculate the zonal flow damping correctly at one poloidal turn. However, the flux tube recovers the flux-surface average at four poloidal turns, and both flux tubes produce the same zonal flow residual. All other HSX flux-tube calculations in this chapter use the $n_{\rm pol}=4$ "bean" flux tube.

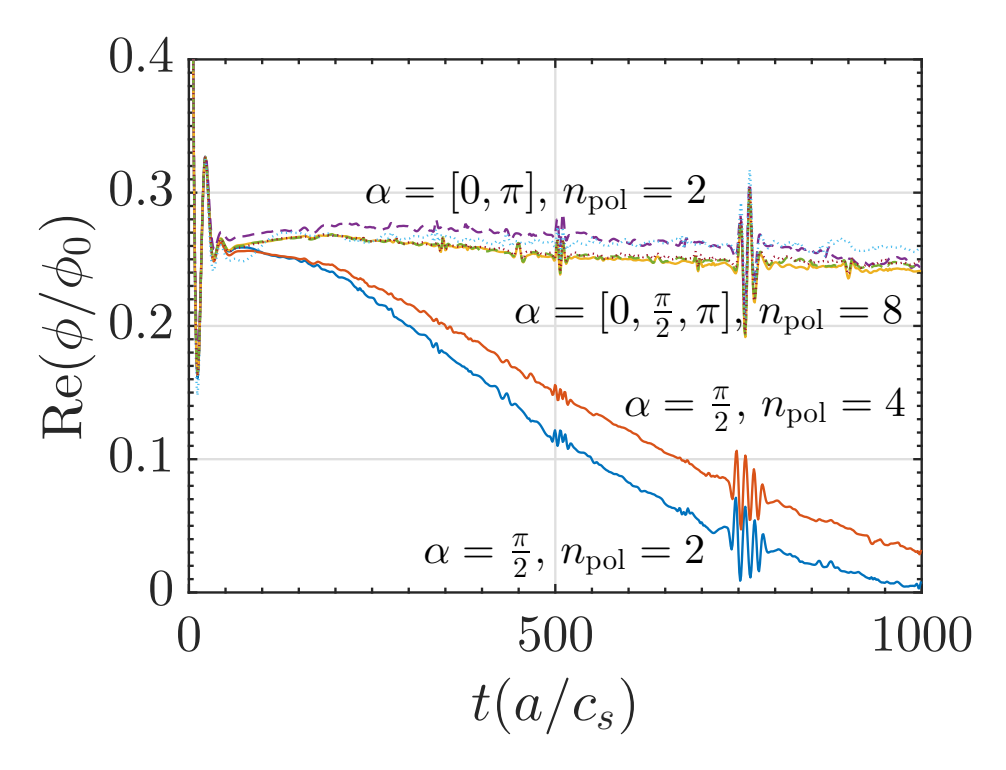


Figure 4.13: Zonal flow damping in NCSX flux tubes for $k_x \rho_s = 0.5$, where $\alpha = 0$ is dashed, $\alpha = \pi/2$ is solid, and $\alpha = \pi$ is dotted. At $n_{\rm pol} = 2$, the $\alpha = [0,\pi]$ flux tubes agree, but the $\alpha = \pi/2$ flux tube decays to zero residual. All three flux tubes produce the same result at $n_{\rm pol} = 8$. The spike at t = 700 is a numerical recurrence effect dependent on the velocity space resolution, and does not affect the interpretation.

Comparison of response in three flux tubes in NCSX

Three flux tubes are examined in the NCSX configuration. The $\alpha=0$ and $\alpha=\pi$ flux tubes are symmetric about the midpoint z=0, while the $\alpha=\pi/2$ flux tube is not. As seen in Figure 4.13, the zonal flow damping is very different in the $\alpha=\pi/2$ flux tube. No zonal flow residual is supported when the flux tube is fewer than eight poloidal turns long. The symmetric flux tubes capture the zonal flow damping at just two poloidal turns. The poloidal distance between turns is larger in NCSX than in HSX due to the difference in rotational transform. This larger poloidal step size samples broad variation on the flux surface, but could under-sample geometry variations that are smaller scale than the poloidal space between turns. Note that with a rotational transform of about one half of

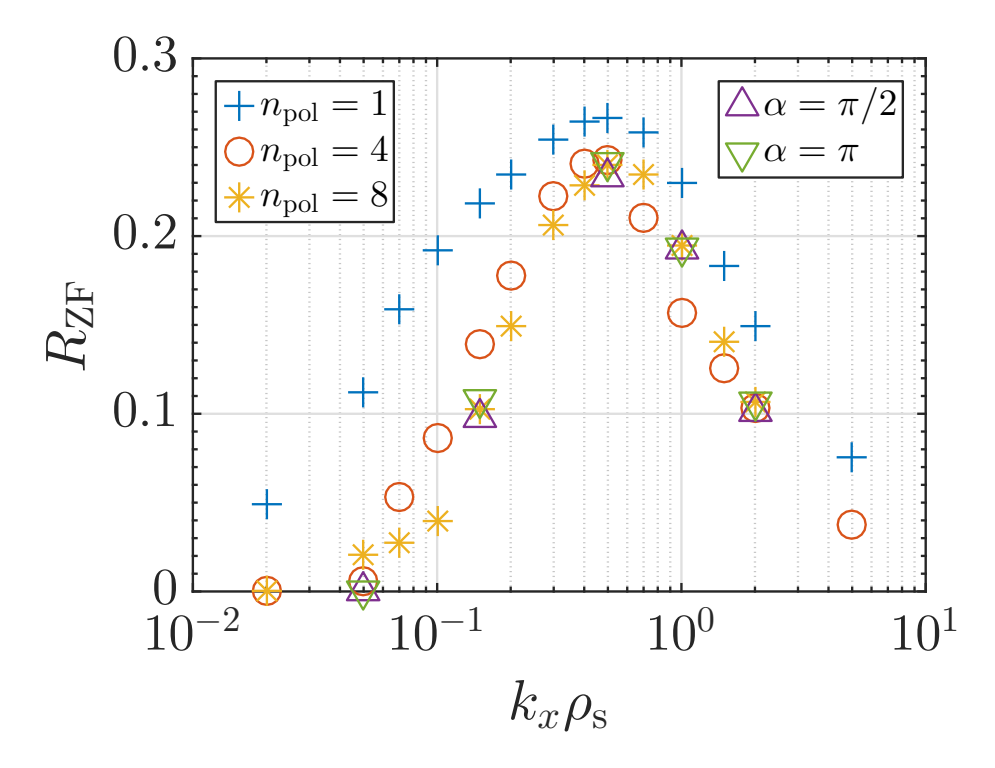


Figure 4.14: k_x spectra of the zonal flow residual $R_{\rm ZF}$ in the $\alpha=0$ flux tube of NCSX. At low k_x , $R_{\rm ZF}$ depends strongly on $n_{\rm pol}$. Points for the $\alpha=\pi/2,\pi$ flux tubes are plotted for $n_{\rm pol}=8$, where all flux tubes converge to the same $R_{\rm ZF}$.

that in HSX, the toroidal length of a two-poloidal-turn flux tube in NCSX is roughly the same as a four-poloidal-turn flux tube in HSX. However, convergence of the zonal flow residual for low $k_x \rho_s < 0.2$ imposes an even more restrictive requirement on flux-tube length, as seen in Figure 4.14. Only at eight poloidal turns do all flux tubes produce the same zonal flow residual for all k_x .

4.4 Comparison of configurations: QHS, Mirror, and NCSX

The QHS and Mirror configurations of HSX have been designed specifically to study differences in neoclassical transport and flow damping. As discussed in Section 4.1, the

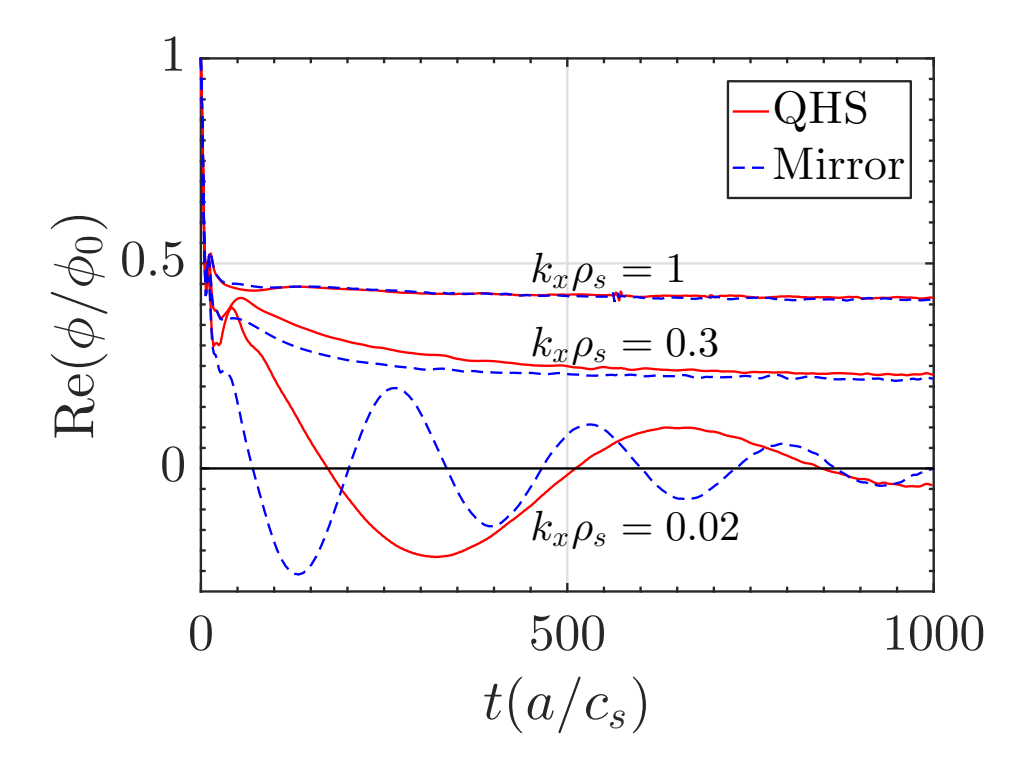


Figure 4.15: The time evolution of the zonal flow in the two HSX configurations, with $n_{\rm pol}=4$ flux tubes. The Mirror configuration has higher frequency zonal flow oscillations and faster long-time damping, as expected based on its reduced quasi-symmetry.

zonal flow long-time decay and oscillation frequency are related to neoclassical transport. According to theory, 20,31 the more optimized QHS configuration should exhibit lower-frequency zonal flow oscillations as well as slower long-time decay to the residual level. These expectations are verified in Figure 4.15. The zonal flow oscillation frequency is higher by a factor of 2.5 in Mirror than QHS at $k_x \rho_s = 0.02$, and the long-time decay is significantly faster at $k_x \rho_s = 0.3$.

As observed in Figure 4.16, the zonal flow residual does not differ between QHS and Mirror. The Rosenbluth-Hinton residual in Equation (4.1) depends primarily on the safety factor q, a consequence of the ratio of the banana-induced polarization relative to the gyro-orbit-induced polarization.³¹ In a non-axisymmetric system, additional trapped particles further modify the zonal flow evolution through their polarization and radial

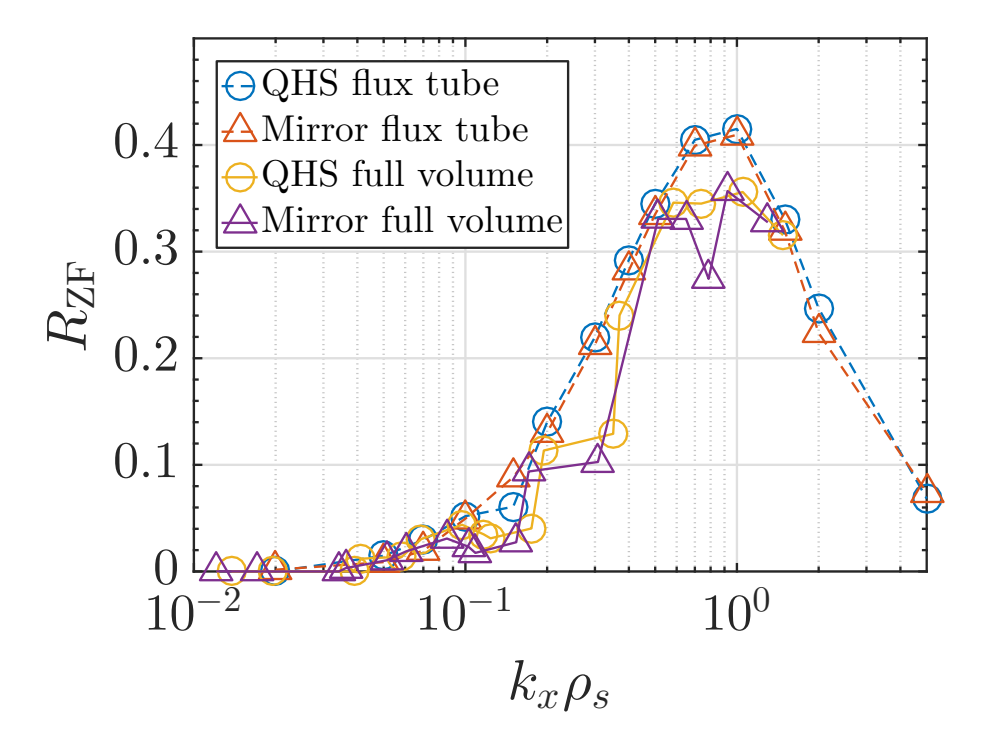


Figure 4.16: Zonal flow residual k_x spectra for QHS and Mirror. The flux tubes for Gene calculations are 4 poloidal turns long, and show good agreement with full-volume calculations. In both flux-tube and full-volume calculations, there is no significant difference between QHS and Mirror.

drift. While the radial drift is important for the time evolution, the zonal flow residual primarily depends upon the polarization effects provided by the trapped particles. ¹⁴ The broken symmetry of the mirror configuration increases the trapped particle radial drift, as demonstrated by the zonal flow oscillation frequency and damping, but does not change the zonal flow residual. We conclude that the helically trapped particles dominate the polarization drift and set the zonal flow residual in both systems.

As compared to NCSX, the QHS configuration produces less trapped-particle radial drift and has a lower zonal flow oscillation frequency, while the Mirror configuration produces more and has a higher oscillation frequency. GAMs are damped more slowly in the NCSX configurations, due to the larger safety factor q, and GAM oscillations can be seen in Figures 4.5 and 4.6 but are barely identifiable in any HSX timetraces. In comparing the zonal

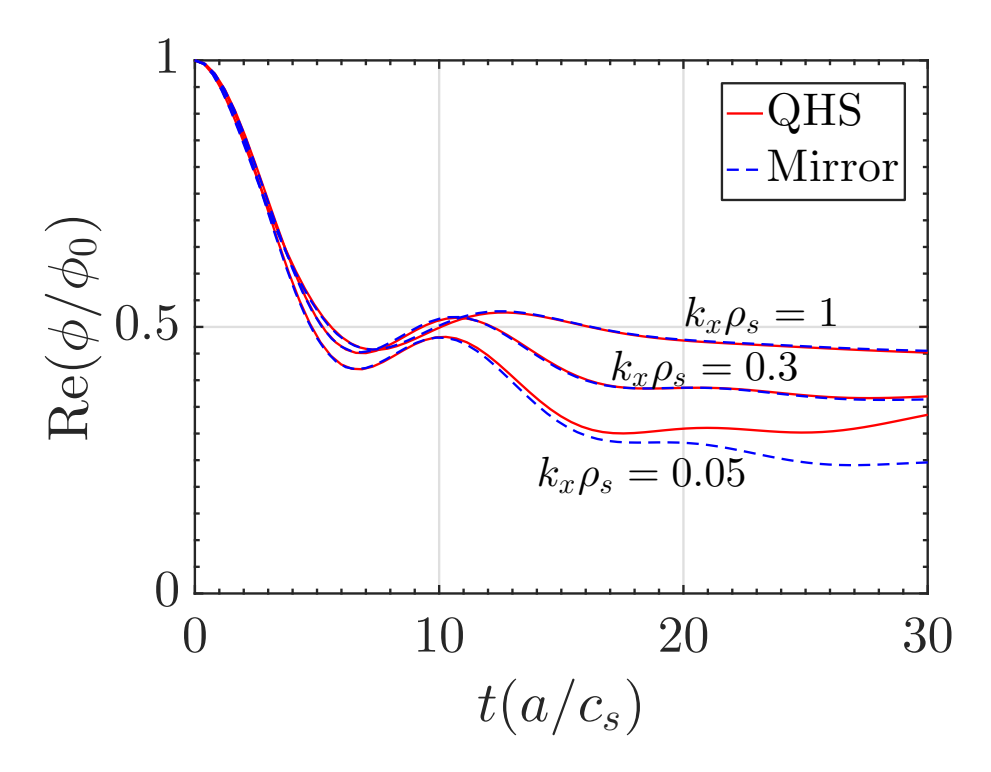


Figure 4.17: The time evolution of the zonal flow for very short times, comparable to the turbulent correlation time. Effectively, there is no difference between QHS and Mirror except at the smallest k_x , and only after about 20 $a/c_{\rm s}$.

flow residual in Figures 4.14 and 4.16, the peak residual is smaller in the NCSX configuration, but the peak location is found at a different k_x . The residual in HSX configurations peaks at $k_x \rho_s \approx 1$, similar to Wendelstein 7-X, while the NCSX configuration peaks at $k_x \rho_s \approx 0.5$, similar to the tokamak in Reference 26.

Calculation of the zonal flow decay in HSX captures the expected neoclassical effects on decay rate and oscillation frequency. However, the saturation of drift wave turbulence is a strong motivation for the study of zonal flows. Turbulence will transfer energy and reorganize the system within a correlation time, effectively resetting the zonal flow time evolution. In nonlinear simulations of trapped electron mode (TEM) turbulence in HSX, the correlation time is on the order of $10\,a/c_{\rm s}$. In Figure 4.17, the short-time damping of the zonal flow is plotted, but again, there is no difference between the QHS and Mirror configurations.

Depending on driving gradients, the heat flux from nonlinear TEM turbulence simulations differs between these configurations, and is not explained by the linear growth of the most unstable mode. If a difference in heat fluxes between configurations is due to the linear collisionless zonal flow dynamics, it is not a simple relation to either the very short-time dynamics or the long-time residual. Instead, it could be hypothesized that, if such a relation exists, it would stem from a shift in characteristic k_x of linear drive physics, which would affect which zonal flow acts to saturate the turbulence. We do not address the question of the effect of an external radial electric field on the zonal flow, and a difference of the ambipolar radial electric field between QHS and Mirror could lead to important differences in the zonal flow decay.

Having demonstrated that simulations confirm the link between broken symmetry and a faster erosion of the zonal flow residual, a link can be established to a similar effect in axisymmetric systems. There, resonant magnetic perturbations, whether created by external coils, ⁴⁹ by magneto-hydrodynamic activity, ⁷ or by microturbulence itself, ⁵⁰ erode the zonal flow residual and lead to increased turbulent transport. ^{43,51} However, erosion time scales in these scenarios were on the order of the turbulent correlation time, giving further credence to the idea that the long-time decay present in the systems investigated here is unlikely to affect transport directly.

4.5 Chapter Summary

We have presented calculations of linear zonal flow damping in quasi-symmetric stellarators. In the geometries of NCSX and HSX, the time evolution is dictated by the typical characteristics of non-axisymmetric devices. The zonal flow residual vanishes for small k_x , the zonal flow undergoes long-time decay to the residual, and zonal flow oscillations occur. Calculations are performed in full-volume, flux-surface, and flux-tube geometries.

A sufficiently long flux tube reproduces the full-volume residual and flux-surface time-dependence, suggesting that parallel dynamics in an appropriate flux tube can approximate the flux-surface average. While $n_{\rm pol}=4$ and $n_{\rm pol}=8$ is sufficient to recover flux-surface results in these two configurations, the required flux-tube length is configuration-dependent and cannot be taken as a general rule. It should be noted that both flux-tube and flux-surface calculations exhibit slightly less decay during the short-time polarization drift than a full-volume calculation. On the other hand, the damping of the zonal flow oscillation is greater in the full-volume calculation. The zonal flow oscillation is only visible at small k_x , where the full-volume calculation supports a larger residual than local representations. This is likely due to the breakdown of the radially-local approximation as k_x approaches the system size.

The collisionless zonal flow decay examined here cannot be correlated to the nonlinear turbulent transport without further information. Nonlinear simulations of TEM in the QHS and Mirror configurations produce different heat fluxes, but the zonal flow residual at finite k_x shows no difference between QHS and Mirror. Given the short timescale of a turbulent correlation time, the short-time damping of the zonal flow may be more relevant to the saturation of turbulence. The polarization drift dominates the short-time zonal flow damping, and there is no difference in the time evolution of the QHS and Mirror configurations until the zonal flow oscillation becomes significant. The HSX QHS and Mirror configurations clearly demonstrate a difference in zonal flow oscillations and long-time decay, but these differences follow the expected dependence on the neoclassical radial drift. Configurations with a larger radial drift have a higher oscillation frequency and slower long-time decay. These quantities cannot be related to the full zonal flow evolution without also directly relating to the neoclassical optimization. In addition, any extrapolation from linear zonal flow damping to nonlinear heat flux requires an understanding of which k_x are important for energy transfer in the specific system under study.

The zonal flow oscillations provide another opportunity to compare simulation and experiment. Corresponding oscillations have been measured at TJ-II through perturbative experiments. ^{25,52} Measurements of the zonal flow at HSX are related to externally imposed electric fields. ¹² A pulse on this external field could excite zonal flow oscillations. The frequency of measured oscillations should depend on the magnetic configuration, and would greatly increase confidence in measurements of the zonal flow.

Future work should include external radial electric fields, which can strongly modify the zonal flow decay and residual. The radial electric field in a stellarator is usually determined by an ambipolarity constraint on neoclassical transport, which can differ between configurations but requires knowledge of density and temperature profiles.

References

- [1] P. H. Diamond, S.-I. Itoh, K. Itoh, and T. S. Hahm, *Zonal flows in plasma—a review*, Plasma Physics and Controlled Fusion **47**, R35 (2005).
- [2] K. D. Makwana, P. W. Terry, and J.-H. Kim, *Role of stable modes in zonal flow regulated turbulence*, Physics of Plasmas **19**, 062310 (2012).
- [3] K. D. Makwana, P. W. Terry, M. J. Pueschel, and D. R. Hatch, *Subdominant modes in zonal-flow-regulated turbulence*, Physical Review Letters **112**, 095002 (2014).
- [4] Z. Lin, T. S. Hahm, W. W. Lee, W. M. Tang, and R. B. White, *Turbulent transport reduction by zonal flows: Massively parallel simulations*, Science **281**, 1835 (1998).
- [5] D. Carmody, M. J. Pueschel, J. K. Anderson, and P. W. Terry, *Microturbulence studies of pulsed poloidal current drive discharges in the reversed field pinch*, Physics of Plasmas **22**, 012504 (2015).
- [6] I. Predebon and P. Xanthopoulos, *Ion temperature gradient turbulence in helical and axisymmetric RFP plasmas*, Physics of Plasmas **22**, 052308 (2015).
- [7] Z. R. Williams, M. J. Pueschel, P. W. Terry, and T. Hauff, *Turbulence, transport, and zonal flows in the Madison symmetric torus reversed-field pinch*, Physics of Plasmas **24**, 122309 (2017).
- [8] T.-H. Watanabe, H. Sugama, and S. Ferrando-Margalet, *Gyrokinetic simulation of zonal flows and ion temperature gradient turbulence in helical systems*, Nuclear Fusion **47**, 1383 (2007).
- [9] B. J. Faber, M. J. Pueschel, J. H. E. Proll, P. Xanthopoulos, P. W. Terry, C. C. Hegna, G. M. Weir, K. M. Likin, and J. N. Talmadge, *Gyrokinetic studies of trapped electron mode turbulence in the Helically Symmetric eXperiment stellarator*, Physics of Plasmas 22, 072305 (2015).
- [10] P. Xanthopoulos, F. Merz, T. Görler, and F. Jenko, *Nonlinear gyrokinetic simulations of ion-temperature-gradient turbulence for the optimized Wendelstein 7-X stellarator*, Physical Review Letters **99**, 035002 (2007).
- [11] G. G. Plunk, P. Xanthopoulos, and P. Helander, *Distinct turbulence saturation regimes in stellarators*, Physical Review Letters **118**, 105002 (2017).
- [12] R. S. Wilcox, B. P. van Milligen, C. Hidalgo, D. T. Anderson, J. N. Talmadge, F. S. B. Anderson, and M. Ramisch, *Measurements of bicoherence and long-range correlations during biasing in the HSX stellarator*, Nuclear Fusion **51**, 083048 (2011).

- [13] J. Smoniewski, E. Sánchez, I. Calvo, M. J. Pueschel, and J. N. Talmadge, *Comparison of local and global gyrokinetic calculations of collisionless zonal flow damping in quasi-symmetric stellarators*, Physics of Plasmas **28**, 042503 (2021).
- [14] P. Xanthopoulos, A. Mischchenko, P. Helander, H. Sugama, and T.-H. Watanabe, *Zonal flow dynamics and control of turbulent transport in stellarators*, Physical Review Letters **107**, 245002 (2011).
- [15] S. Toda, M. Nunami, and H. Sugama, *Reduced models of turbulent transport in helical plasmas including effects of zonal flows and trapped electrons*, Journal of Plasma Physics **86**, 815860304 (2020).
- [16] M. Nunami, T.-H. Watanabe, and H. Sugama, *A reduced model for ion temperature gradient turbulent transport in helical plasmas*, Physics of Plasmas **20**, 092307 (2013).
- [17] M. N. Rosenbluth and F. L. Hinton, *Poloidal flow driven by ion-temperature-gradient turbulence in tokamaks*, Physical Review Letters **80**, 724 (1998).
- [18] A. M. Dimits, G. Bateman, M. A. Beer, B. I. Cohen, W. Dorland, G. W. Hammett, C. Kim, J. E. Kinsey, M. Kotschenreuther, A. H. Kritz, L. L. Lao, J. Mandrekas, W. M. Nevins, S. E. Parker, A. J. Redd, D. E. Shumaker, R. Sydora, and J. Weiland, *Comparisons and physics basis of tokamak transport models and turbulence simulations*, Physics of Plasmas 7, 969 (2000).
- [19] A. Mishchenko, P. Helander, and A. Könies, *Collisionless dynamics of zonal flows in stellarator geometry*, Physics of Plasmas **15**, 072309 (2008).
- [20] P. Helander, A. Mishchenko, R. Kleiber, and P. Xanthopoulos, *Oscillations of zonal flows in stellarators*, Plasma Physics and Controlled Fusion **53**, 054006 (2011).
- [21] E. Sánchez, R. Kleiber, R. Hatzky, M. Borchardt, P. Monreal, F. Castejón, A. López-Fraguas, X. Sáez, J. L. Velasco, I. Calvo, A. Alonso, and D. López-Bruna, *Collisionless damping of flows in the TJ-II stellarator*, Plasma Physics and Controlled Fusion **55**, 014015 (2013).
- [22] P. Monreal, E. Sánchez, I. Calvo, A. Bustos, F. I. Parra, A. Mishchenko, A. Könies, and R. Kleiber, *Semianalytical calculation of the zonal-flow oscillation frequency in stellarators*, Plasma Physics and Controlled Fusion **59**, 065005 (2017).
- [23] T.-H. Watanabe, H. Sugama, and S. Ferrando-Margalet, *Reduction of turbulent transport with zonal flows enhanced in helical systems*, Physical Review Letters **100**, 195002 (2008).
- [24] S. Ferrando-Margalet, H. Sugama, and T.-H. Watanabe, *Zonal flows and ion temperature gradient instabilities in multiple-helicity magnetic fields*, Physics of Plasmas **14**, 122505 (2007).

- [25] E. Sánchez, I. Calvo, J. L. Velasco, F. Medina, A. Alonso, P. Monreal, and R. Kleiber, *Oscillatory relaxation of zonal flows in a multi-species stellarator plasma*, Plasma Physics and Controlled Fusion **60**, 094003 (2018).
- [26] P. Monreal, I. Calvo, E. Sánchez, F. I. Parra, A. Bustos, A. Könies, R. Kleiber, and T. Görler, *Residual zonal flows in tokamaks and stellarators at arbitrary wavelengths*, Plasma Physics and Controlled Fusion **58**, 045018 (2016).
- [27] S. Matsuoka, Y. Idomura, and S. Satake, *Neoclassical transport benchmark of global full-f gyrokinetic simulation in stellarator configurations*, Physics of Plasmas **25**, 022510 (2018).
- [28] T. Moritaka, R. Hager, M. Cole, S. Lazerson, C.-S. Chang, S.-H. Ku, S. Matsuoka, S. Satake, and S. Ishiguro, *Development of a gyrokinetic particle-in-cell code for whole-volume modeling of stellarators*, Plasma **2**, 179 (2019).
- [29] W. A. Guttenfelder, Measurements and Modeling of Turbulent Transport in the HSX Stellarator, Ph.D. thesis, The University of Wisconsin-Madison (2008).
- [30] H. Sugama and T.-H. Watanabe, *Dynamics of zonal flows in helical systems*, Physical Review Letters **94**, 115001 (2005).
- [31] H. Sugama and T.-H. Watanabe, *Collisionless damping of zonal flows in helical systems*, Physics of Plasmas **13**, 012501 (2006).
- [32] O. Yamagishi, Non-isomorphic radial wavenumber dependencies of residual zonal flows in ion and electron Larmor radius scales, and effects of initial parallel flow and electromagnetic potentials in a circular tokamak, Plasma Physics and Controlled Fusion **60**, 045009 (2018).
- [33] Y. Xiao and P. J. Catto, *Short wavelength effects on the collisionless neoclassical polarization and residual zonal flow level*, Physics of Plasmas **13**, 102311 (2006).
- [34] F. Jenko, W. Dorland, M. Kotschenreuther, and B. N. Rogers, *Electron temperature gradient driven turbulence*, Physics of Plasmas 7, 1904 (2000).
- [35] A. Mishchenko and R. Kleiber, *Zonal flows in stellarators in an ambient radial electric field*, Physics of Plasmas **19**, 072316 (2012).
- [36] H. Sugama and T.-H. Watanabe, *Turbulence-driven zonal flows in helical systems with radial electric fields*, Physics of Plasmas **16**, 056101 (2009).
- [37] H. Sugama and T.-H. Watanabe, *Enhancement of residual zonal flows in helical systems with equilibrium radial electric fields*, Contributions to Plasma Physics **50**, 571 (2010).
- [38] G. Jost, T. M. Tran, W. A. Cooper, L. Villard, and K. Appert, *Global linear gyrokinetic simulations in quasi-symmetric configurations*, Physics of Plasmas **8**, 3321 (2001).
- [39] V. Kornilov, R. Kleiber, R. Hatzky, L. Villard, and G. Jost, *Gyrokinetic global three-dimensional simulations of linear ion-temperature-gradient modes in Wendelstein 7-X*, Physics of Plasmas **11**, 3196 (2004).

- [40] R. C. Grimm, J. M. Greene, and J. L. Johnson, in *Methods in Computational Physics: Advances in Research and Applications*, Controlled Fusion, Vol. 16, edited by J. Killeen (Elsevier, 1976) pp. 253–280.
- [41] E. Sánchez, A. Mishchenko, J. M. García-Regaña, R. Kleiber, A. Bottino, L. Villard, and the W7-X Team, *Nonlinear gyrokinetic PIC simulations in stellarators with the code EUTERPE*, Journal of Plasma Physics **86**, 855860501 (2020).
- [42] M. F. Martin, M. Landreman, P. Xanthopoulos, N. R. Mandell, and W. Dorland, *The parallel boundary condition for turbulence simulations in low magnetic shear devices*, Plasma Physics and Controlled Fusion **60**, 095008 (2018).
- [43] M. J. Pueschel, D. R. Hatch, T. Görler, W. M. Nevins, F. Jenko, P. W. Terry, and D. Told, *Properties of high-\beta microturbulence and the non-zonal transition*, Physics of Plasmas **20**, 102301 (2013).
- [44] M. J. Pueschel, T. Dannert, and F. Jenko, *On the role of numerical dissipation in gyrokinetic Vlasov simulations of plasma microturbulence*, Computer Physics Communications **181**, 1428 (2010).
- [45] T. Dannert and F. Jenko, *Vlasov simulation of kinetic shear Alfvén waves*, Computer Physics Communications **163**, 67 (2004).
- [46] F. S. B. Anderson, A. F. Almagri, D. T. Anderson, P. G. Matthews, J. N. Talmadge, and J. L. Shohet, *The Helically Symmetric Experiment*, (HSX) Goals, design and status, Fusion Technology **27**, 273 (1995).
- [47] M. C. Zarnstorff, L. A. Berry, A. Brooks, E. Fredrickson, G.-Y. Fu, S. Hirshman, S. Hudson, L.-P. Ku, E. Lazarus, D. Mikkelsen, D. Monticello, G. H. Neilson, N. Pomphrey, A. Reiman, D. Spong, D. Strickler, A. Boozer, W. A. Cooper, R. Goldston, R. Hatcher, M. Isaev, C. Kessel, J. Lewandowski, J. F. Lyon, P. Merkel, H. Mynick, B. E. Nelson, C. Nuehrenberg, M. Redi, W. Reiersen, P. Rutherford, R. Sanchez, J. Schmidt, and R. B. White, *Physics of the compact advanced stellarator NCSX*, Plasma Physics and Controlled Fusion 43, A237 (2001).
- [48] S. P. Hirshman and J. C. Whitson, *Steepest-descent moment method for three-dimensional magnetohydrodynamic equilibria*, Physics of Fluids **26**, 3553 (1983).
- [49] Z. R. Williams, M. J. Pueschel, P. W. Terry, T. Nishizawa, D. M. Kriete, M. D. Nornberg, J. S. Sarff, G. R. McKee, D. M. Orlov, and S. H. Nogami, *Impact of resonant magnetic perturbations on zonal flows and microturbulence*, Nuclear Fusion **60**, 096004 (2020).
- [50] M. J. Pueschel, P. W. Terry, F. Jenko, D. R. Hatch, W. M. Nevins, T. Görler, and D. Told, *Extreme heat fluxes in gyrokinetic simulations: A new critical* β , Physical Review Letters **110**, 155005 (2013).

- [51] P. W. Terry, M. J. Pueschel, D. Carmody, and W. M. Nevins, *The effect of magnetic flutter on residual flow*, Physics of Plasmas **20**, 112502 (2013).
- [52] J. A. Alonso, I. Calvo, J. L. Velasco, K. J. McCarthy, A. Chmyga, L. G. Eliseev, T. Estrada, R. Kleiber, L. I. Krupnik, A. V. Melnikov, P. Monreal, F. I. Parra, S. Perfilov, and A. I. Zhezhera, *Observation of oscillatory radial electric field relaxation in a helical plasma*, Physical Review Letters **118**, 185002 (2017).

Conclusions and Suggestions for Future Investigations

Optimization of stellarator configurations for reduced turbulent transport is a major opportunity on the path to the peaceful application of fusion power. However, such optimization relies on the ability of simulations to accurately predict turbulence in real devices. Very few validation studies exist for the three-dimensional geometry of a stellarator, and this work has started the process of validating gyrokinetic simulations in the only existing quasi-symmetric stellarator. The magnetic configuration flexibility of the Helically Symmetric eXperiment has been used to investigate trapped electron mode turbulence in quasi-helically symmetric and degraded-symmetry configurations. This dissertation contains the first detailed comparison of experimental measurements in a stellarator to nonlinear gyrokinetic simulations of trapped-electron-mode turbulence at experimental parameters. While the linear growth rate of the most unstable mode is not predictive of overall turbulence, it was shown that key experimental trends are captured in nonlinear simulations.

Chapter 2 presented experimental measurements of the heat flux and density fluctuation amplitude for comparison to simulation. A database of archived plasma profiles has enabled experimental discharges to be matched for any standard measurement at HSX. Specifically, discharges in the QHS and Mirror magnetic geometries were matched for density and temperature profiles more closely than previously achievable. A reduced power balance analysis of these profiles at $r/a \approx 0.5$ shows that the heat flux and thermal

diffusivity are larger in the Mirror configuration for matched profiles. An experimental a/L_n scan is achieved by filtering the profile database for an approximately constant temperature gradient a/L_T . It was shown that the heat flux increases with increasing density gradient a/L_n . In addition, the heat flux is only matched between QHS and Mirror when the normalized density gradient is smaller in the Mirror configuration. A similar scan of a/L_T e shows that the heat flux does not depend on the temperature gradient. Reflectometry measurements are available for a subset of profiles in the database. It was shown that fluctuations are small enough to use a linear model to relate the reflectometer phase to density fluctuations. The density fluctuation amplitude increases with increasing density gradient, but there is insufficient data to identify a difference between QHS and Mirror.

The first-ever comparison of nonlinear gyrokinetic simulations in the QHS and Mirror configurations was presented in Chapter 3. Linear growth rates are smaller in Mirror than in QHS, as expected due to the reduced overlap of particle trapping regions and unfavorable curvature. However, the heat flux in nonlinear simulations is larger in the Mirror configuration at nominal profiles. Comparison to experiments requires using experimental parameters, and Section 3.3 explored the effect of $T_{\rm i}/T_{\rm e} \neq 1$ and $a/L_{T\rm e}>0$ on the TEM in linear and nonlinear simulations. The difference in heat flux between QHS and Mirror is eliminated with the experimentally relevant temperature ratio $T_{\rm i}/T_{\rm e}=0.2$. Simulations at experimental parameters were presented in Section 3.4 and compared to the experimental measurements in Section 3.5. The results of the comparison between simulation and experiment are summarized in Table 5.1. While simulations at experimental parameters do not predict the difference in heat flux between configurations, the heat flux is sensitive to whether turbulence is in the ∇n -driven or $\nabla T_{\rm e}$ -driven regime, and more precise profile gradient measurements would be required for full validation.

However, the simulated heat flux matches measurements within experimental uncertainties for both configurations, and general trends are captured by nonlinear simulations.

In Experiment:	In Nonlinear Simulation:	
Heat flux in Mirror is larger than in QHS	No difference between QHS and Mirror at $T_{\rm i}/T_{\rm e}=0.2$, but flux is sensitive to $\Delta(a/L_n)$, $\Delta(a/L_{T\rm e})$ smaller than measured uncertainty	
Heat flux magnitude $Q_{\rm e} pprox 4{\rm kWm^{-2}}$		
Heat flux depends more strongly on a/L_n than $a/L_{\rm Te}$		
Density fluctuations $\tilde{n}/n \approx 0.007$	Density fluctuations $\tilde{n}/n \approx 0.02$	
Density fluctuation amplitude increases with increasing a/L_n		

Table 5.1: Summary of the comparison between experimental measurements and nonlinear simulations at experimental parameters. Single column rows indicate agreement, while any difference are listed in two-column rows.

The density and temperature gradients were varied in simulation in Section 3.4 to compare to experimental gradient scalings, and the heat flux scales more strongly with the density gradient than the temperature gradient in both simulation and experiment. The matched heat flux and gradient drive between simulation and experiment confirms that ∇n -driven TEM turbulence is the dominant driver of anomalous transport at the mid-radius in HSX. While the nonlinear heat flux increases more strongly with a/L_n , growth rates increase more strongly with a/L_{Te} . Frequencies in nonlinear simulations transition from the electron diamagnetic direction when $a/L_{Te} > a/L_n$ to the ion direction when $a/L_n > a/L_{Te}$, despite the absence of any unstable linear modes with a positive frequency. These findings suggest that the dynamics of the TEM are determined by nonlinear effects. As this change occurs around $a/L_n = a/L_{Te}$, the density and temperature gradient drives are potentially associated with different saturation and nonlinear dynamics in the quasi-stationary state. This transition differs between the QHS and Mirror configurations, with positive frequencies persisting in the QHS configuration to higher a/L_{Te} than in Mirror.

A comparison of density fluctuations finds that fluctuations from simulation are smaller than experimental measurements by a factor of ≈ 3 . This is likely due to the combined effect

of the linear fluctuation analysis of reflectometry measurements and the crude synthetic diagnostic applied to the simulation data. However, simulated density fluctuations increase with density gradient but are independent of the temperature gradient, in agreement with measurements.

Finally, the collisionless damping of the zonal flow was investigated in Chapter 4. This is the first calculation of zonal flow damping in quasi-symmetric geometries, and the QHS and Mirror configurations of HSX are compared with the quasi-axial symmetry of the National Compact Stellarator eXperiment. Despite quasi-symmetry, the collisionless dynamics of the zonal flow in all three configurations are more similar to what would be expected in a conventional stellarator than a tokamak: Zonal flow oscillations and long-time damping affect the zonal flow evolution, and the zonal flow residual goes to zero for small radial wavenumber.

Calculations were performed in flux-tube, flux-surface, and full-volume geometry. While each flux tube on a flux surface is unique, several different flux tubes in HSX or NCSX can reproduce the zonal flow damping from a flux-surface calculation given an adequate parallel extent. However, the oscillation and damping time scales in local representations are longer than in full-volume geometry at small radial wavenumbers. The oscillation frequency and damping rate depend on the bounce-averaged radial particle drift in accordance with theory, and provides another opportunity to compare future possible experimental measurements to Gene calculations. This research has been published in Reference 1.

5.1 Suggestions for Future Investigations

This dissertation is the first comparison of experimental measurements at HSX to nonlinear gyrokinetic simulations at experimental parameters. While the gradient scaling and the

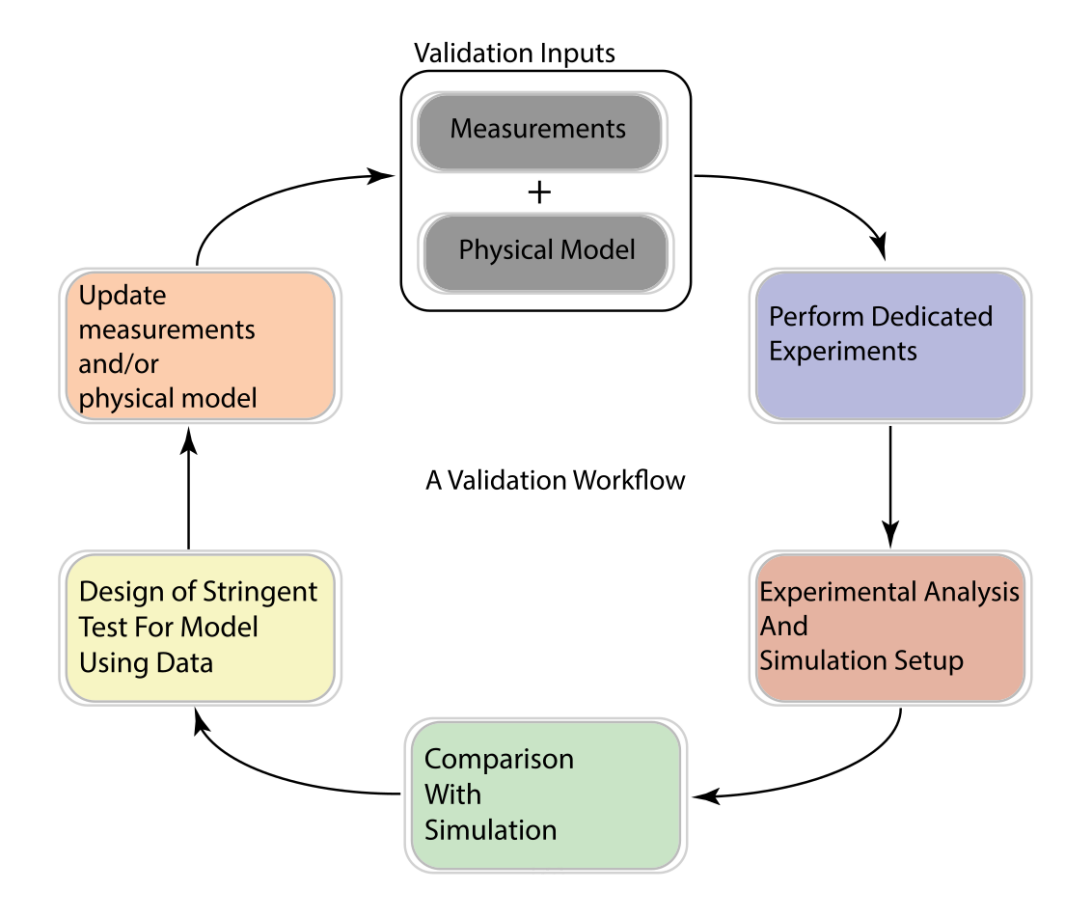


Figure 5.1: A diagram of the validation process, reproduced from Reference 2. The comparison of measurements and simulations identifies gaps in current data or understanding, which can then be addressed with further measurements and simulations.

heat flux agree, precise agreement of the density fluctuation amplitude and configurational differences is indeterminate. This study should be considered as only one cycle of the validation loop² depicted in Figure 5.1. The uncertainty in measured density and temperature profiles and their gradients is the most significant barrier to the comparison of HSX measurements to simulations. Updated experimental measurements and a deeper understanding of the different ∇n -driven and $\nabla T_{\rm e}$ -driven TEM dynamics will start the next cycle of the validation loop. Several possible investigations to advance validation studies at HSX are proposed in this section.

Improved profile fitting and reduced gradient uncertainty

Measurements in this work were hampered by the large uncertainty of experimental profile gradients. This uncertainty blurs any trends that depend on gradient scans and introduces large uncertainty to calculations of the thermal diffusivity, and is large enough that it is unclear if L_n/L_{Te} is larger or smaller than unity for most profiles. Reduced uncertainties would clarify scalings with driving gradients and could identify which gradient is larger in experimental profiles. These studies are needed for comparison to saturation in the ∇n -driven versus the ∇T_e -driven TEM regimes. As discussed below, more precise profile measurements would enable flux-matching studies in Gene simulations, which in turn could be developed into a full validation study.

The Gaussian process regression fits to Thomson scattering profiles in Chapter 2 did not improve on the linear fit for the mid-radius, but the applicability of the linear fit is reduced for any other radial location. Particularly for studies of the $\nabla T_{\rm e}$ -driven regime, the experimental gradients for $r/a\approx 0.3$ are needed. Gaussian process regression can reliably infer profiles with systematic uncertainty estimation for the entire plasma. This has been used in a Bayesian framework to integrate measurements from multiple diagnostics with pre-existing physics knowledge, resulting in much improved profile estimates. HSX is well equipped with diagnostics for such analysis. Currently, separate electron density information is provided by Thomson scattering and microwave interferometry diagnostics. Separate electron temperature information is provided by Thomson scattering and Electron Cyclotron Emission (ECE) diagnostics. Integration of these three diagnostics to infer a single consistent plasma description could greatly reduce the uncertainty in temperature and density profiles. Additionally, the CHarge Exchange Recombination Spectroscopy (CHERS) diagnostic could be integrated to improve ion temperature profiles.

A hardware solution to profile uncertainties could be the development of gradientspecific experimental measurements. At DIII-D, a profile reflectometer has played a key role in reducing gradient uncertainties,⁴ and can even be used for real-time control of the density gradient.⁵ A fast-sweep reflectometer could provide both precise gradient measurements as well as density fluctuation information.

Extension of gyrokinetic simulations

Due to the large computational cost of nonlinear TEM simulations, simplifications were made in Chapter 3 that should be addressed in future work. A flux tube from r/a = 0.7 was used because the small global shear at r/a = 0.5 greatly increased the cost of simulations. Recent work has found that the turbulence in HSX may be accurately reproduced with a shearless flux tube if the extended structure of modes in low-shear geometry is properly resolved. Future TEM simulations may confirm the validity of a shearless flux tube and use the real geometry of the exact radial location. Additionally, it is unlikely that the normalized ion temperature gradient is zero, and its effect on the TEM should be investigated. Ideally, the flux tube results should be compared to simulations in global geometry representations to capture profile and radial electric field effects, but the numerical cost for such a study is presently too large. This dissertation focused on simulations for comparison to experimental measurements, but the saturation and nonlinear dynamics of TEM turbulence in HSX still needs to be understood. Previous studies have used a quasilinear model to match TEM transport in HSX, while linear growth rates were not predictive of nonlinear transport in this dissertation. Further study should assess how well the quasilinear model reproduces nonlinear simulations for HSX configurations.

Investigation of the ∇n -driven and $\nabla T_{\rm e}$ -driven turbulence regimes

Analysis of experimental density fluctuations suggests that the ∇n -driven TEM dominates turbulence in HSX. However, profile measurements show that gradients in the experiment span both $a/L_n > a/L_{Te}$ and $a/L_{Te} > a/L_n$. Nonlinear simulations in Chapter 3 show

that nonlinear dynamics and saturation can be strongly affected by which gradient is the primary turbulence drive. The dependence of fluxes on driving gradients differs significantly between turbulence in ∇n -driven and $\nabla T_{\rm e}$ -driven regimes, and does not correspond to the linear growth rates of the most unstable mode. This may be related to a change in nonlinear frequencies that is not reflected in the linear mode spectrum.

The radial variation of the density and temperature profile in HSX offers an opportunity to investigate the dependence of turbulent transport on the ∇n -driven versus the $\nabla T_{\rm e}$ -driven regimes in both simulation and experiment. The heat flux and density fluctuations could be compared between experiment and simulation for a different radial location where $a/L_{\rm Te}>a/L_n$, such as $r/a\approx 0.3$, where the zero-shear approximation may be a useful approach. Frequency spectra of fluctuations may be a key indicator to determine the dominant gradient drive, but this needs to be confirmed in further simulation. A higher resolution scan of a/L_n in nonlinear simulations is needed to understand if the transition between gradient drives is different in the QHS and Mirror configurations. Such a threshold behavior would be an important point of comparison to experimental measurements.

Further analysis of fluctuations from reflectometry

The derivation of density fluctuation amplitudes from reflectometry measurements is an active research question, and it is not clear that the model in Section 2.3 will be an adequate basis for corresponding validation. However, analysis of nonlinear simulations showed that fluctuation frequencies may be a more valuable indicator of turbulence regime. In Chapter 3, it was shown that frequencies shift from the electron diamagnetic direction to the ion direction as turbulence shifts from a $\nabla T_{\rm e}$ -driven to a ∇n -driven regime. While the HSX reflectometer cannot measure the phase velocity in the ion or electron direction, the positive frequencies are associated with a broader spectrum. A normal-incidence reflectometer may be able to identify if turbulence is in a ∇n or $\nabla T_{\rm e}$ regime from the

measured frequency spectrum. This may potentially even alleviate the gradient uncertainty in experimental profiles. Density fluctuation frequencies are not included in this work, and further analysis is required to understand if this could be measured in experiment. However, previous analysis of reflectometry shows that frequency spectra are much more broad in the Mirror configuration, and that a coherent mode is detected in QHS.⁸ It would be worthwhile to understand if this comparison changes with driving gradients, and if it can be explained by TEM turbulence simulation. Such an investigation may need to model the full electromagnetic wave propagation and reflection in a synthetic diagnostic. The IPF-FD3D code⁹ has been developed for this purpose and has been used to model reflection from fluctuations in Gene simulations.¹⁰

Transport in the Hill-Well configuration spectrum

The analysis in this dissertation depended on the large number of experimental profiles available in archived data, and the QHS and Mirror configurations are the most studied in the magnetic configuration space of HSX. These configurations have different levels of neoclassical transport, even though the volume, rotational transform, and magnetic well depth are broadly similar, as discussed in Section 1.2. The matched volume and unshifted magnetic axis at the boxport are important to facilitate comparable experimental operations between configurations. Any new configuration will face operational challenges before reliable profiles can be collected.

However, a few other configurations are represented in a relevant number of discharges of archived data, although still far fewer discharges than in QHS or Mirror. The Hill and Well spectrum of configurations primarily differ in the value of the rotational transform and magnetic well depth, both of which are known to affect anomalous transport. ¹¹ The change in global magnetic shear and magnetic ripple is small for most of the minor radius. Experiments at HSX have demonstrated that much higher plasma performance is achievable

in the Well configuration than in Hill, although a detailed study has not been completed. A similar trend has been noted during Wendelstein 7-X operations. A comparison of gyrokinetic simulations to experimental measurements in the Hill-Well configurations is a natural complementary study to the work in this dissertation.

Zonal flow oscillations in the QHS and Mirror configurations

Calculation of the collisionless zonal flow damping in Chapter 4 showed that the zonal flow oscillation frequency is significantly different in the QHS and Mirror configurations in agreement with theoretical predictions. Such oscillations have been measured at TJ-II through perturbative experiments. ¹² Measurements of the zonal flow in HSX are related to externally imposed electric fields, ¹³ and a pulse on this external field could excite zonal flow oscillations, similar to the experiment in TJ-II. The frequency and damping of measured oscillations is expected to depend on the magnetic configuration. Such a measurement would greatly increase confidence in measurements of the zonal flow.

Zonal flow oscillation experiments are an opportunity to make a comparison between experiment and linear gyrokinetic calculations. Comparisons to the TJ-II measurements are sensitive to the density and temperature of impurity ion species. ¹⁴ Calculations in Chapter 4 also ignore the ambipolar electric field, which is known to affect zonal flow oscillations. ¹⁵ The ambipolar radial electric field may differ between QHS and Mirror, potentially affecting the comparison of configurations. Numerical investigations of these effects in the HSX geometry will be important if zonal flow oscillation measurements are to be compared directly to calculations.

The isotope effect

Experiments have long identified global differences in confinement between Hydrogendominated and Deuterium-dominated plasmas, known as the "isotope effect", that is not consistent with gyro-Bohm predictions. Numerical studies for other experiments show that increasing isotope mass stabilizes TEM turbulence and increases the impact of the zonal flow. ¹⁶ A similar study for HSX would be straightforward with the current simulation framework using Gene. At TJ-II, plasmas with similar parameters to those in HSX found that radial correlation lengths increased with increasing deuterium/hydrogen ratio, and that long-range correlations associated with the zonal flow decreased. ¹⁷ This is the opposite effect as observed in tokamak plasmas. ¹⁸ As the only quasi-symmetric stellarator, measurements and accompanying gyrokinetic turbulence simulations on HSX would be important to understanding the different role of isotope mass in symmetric and non-symmetric devices.

References

- [1] J. Smoniewski, E. Sánchez, I. Calvo, M. J. Pueschel, and J. N. Talmadge, *Comparison of local and global gyrokinetic calculations of collisionless zonal flow damping in quasi-symmetric stellarators*, Physics of Plasmas **28**, 042503 (2021).
- [2] A. E. White, *Validation of nonlinear gyrokinetic transport models using turbulence measure- ments*, Journal of Plasma Physics **85**, 745850101 (2019).
- [3] T. Nishizawa, M. Cavedon, R. Dux, F. Reimold, and U. von Toussaint, *Plasma parameter profile inference from limited data utilizing second-order derivative priors and physic-based constraints*, Physics of Plasmas **28**, 032504 (2021).
- [4] L. Zeng, W. A. Peebles, E. J. Doyle, T. L. Rhodes, N. Crocker, X. Nguyen, C. W. Wannberg, and G. Wang, *Performance and data analysis aspects of the new DIII-D monostatic profile reflectometer system*, Review of Scientific Instruments **85**, 11D843 (2014).
- [5] L. Zeng, E. J. Doyle, T. L. Rhodes, G. Wang, C. Sung, W. A. Peebles, and M. Bobrek, *A novel technique for real-time estimation of edge pedestal density gradients via reflectometer time delay data*, Review of Scientific Instruments **87**, 11E719 (2016).
- [6] B. J. Faber, M. J. Pueschel, P. W. Terry, C. C. Hegna, and J. E. Roman, *Stellarator microinstabilities and turbulence at low magnetic shear*, Journal of Plasma Physics **84**, 905840503 (2018).
- [7] W. Guttenfelder, J. Lore, D. T. Anderson, F. S. B. Anderson, J. M. Canik, W. Dorland, K. M. Likin, and J. N. Talmadge, *Effect of quasihelical symmetry on trapped-electron mode transport in the HSX stellarator*, Physical Review Letters **101**, 215002 (2008).
- [8] K. M. Likin, C. Lechte, H. Lu, and F. S. B. Anderson, *ECE and reflectometry on the Helically Symmetric Experiment*, in *Proceedings of ITC/ISHW2007* (2007).
- [9] C. Lechte, *Investigation of the scattering efficiency in Doppler reflectometry by two-dimensional full-wave simulations*, IEEE Transactions on Plasma Science **37**, 1099 (2009).
- [10] C. Lechte, G. D. Conway, T. Görler, C. Tröster-Schmid, and the ASDEX Upgrade Team, *X mode Doppler reflectometry k-spectral measurements in ASDEX Upgrade: Experiments and simulations*, Plasma Physics and Controlled Fusion **59**, 075006 (2017).
- [11] U. Stroth, M. Murakami, R. A. Dory, H. Yamada, S. Okamura, F. Sano, and T. Obiki, *Energy confinement scaling from the international stellarator database*, Nuclear Fusion **36**, 1063 (1996).
- [12] J. A. Alonso, I. Calvo, J. L. Velasco, K. J. McCarthy, A. Chmyga, L. G. Eliseev, T. Estrada, R. Kleiber, L. I. Krupnik, A. V. Melnikov, P. Monreal, F. I. Parra, S. Perfilov, and A. I. Zhezhera, *Observation of oscillatory radial electric field relaxation in a helical plasma*, Physical Review Letters **118**, 185002 (2017).

- [13] R. S. Wilcox, B. P. van Milligen, C. Hidalgo, D. T. Anderson, J. N. Talmadge, F. S. B. Anderson, and M. Ramisch, *Measurements of bicoherence and long-range correlations during biasing in the HSX stellarator*, Nuclear Fusion **51**, 083048 (2011).
- [14] E. Sánchez, I. Calvo, J. L. Velasco, F. Medina, A. Alonso, P. Monreal, and R. Kleiber, *Oscillatory relaxation of zonal flows in a multi-species stellarator plasma*, Plasma Physics and Controlled Fusion **60**, 094003 (2018).
- [15] A. Mishchenko and R. Kleiber, *Zonal flows in stellarators in an ambient radial electric field*, Physics of Plasmas **19**, 072316 (2012).
- [16] M. Nakata, M. Nunami, H. Sugama, and T.-H. Watanabe, *Isotope effects on trapped-electron-mode driven turbulence and zonal flows in helical and tokamak plasmas*, Physical Review Letters **118**, 165002 (2017).
- [17] B. Liu, M. Pedrosa, B. van Milligen, C. Hidalgo, C. Silva, F. Tabarés, B. Zurro, K. Mc-Carthy, A. Cappa, M. Liniers, and the TJ-II Team, *Isotope effect physics, turbulence and long-range correlation studies in the TJ-II stellarator*, Nuclear Fusion **55**, 112002 (2015).
- [18] Y. Xu, C. Hidalgo, I. Shesterikov, A. Krämer-Flecken, S. Zoletnik, M. Van Schoor, M. Vergote, and the TEXTOR Team, *Isotope effect and multiscale physics in fusion plasmas*, Physical Review Letters **110**, 265005 (2013).

A PROXY VALUES FOR TEM TRANSPORT IN HSX

in Reference 1, a proxy was developed to predict the transport driven by TEM turbulence based only on geometric information. J.H.E Proll has kindly provided values of the proxy for the specific geometry used in this work.

	$n_{\rm pol} = 1$	$n_{\rm pol} = 4$
QHS	-0.0128873	-0.00935465
Mirror	-0.0121582	-0.00858471
Well	-0.00787522	-0.00494316

Table A.1: Proxy values for TEM turbulence in flux tubes from HSX configurations. courtesy of J.H.E. Proll. More negative values predict larger turbulent flux.

The proxy primarily depends on the amount of overlap of particle trapping and bad curvature regions. This overlap is reduced in the Mirror configuration as compared to QHS, and the proxy predicts less transport in Mirror. The Well configuration is predicted to have further improved transport, but comparison to simulation or experiment is left to future work. When flux tubes are extended to four poloidal turns, the proxy value is improved due to de-phasing of trapped particle regions and bad curvature at the extremities of the flux tube. However, most unstable modes are not extended along the field line this far, and this is not expected to be a physical effect.

References

[1] J. H. E. Proll, H. E. Mynick, P. Xanthopoulos, S. A. Lazerson, and B. J. Faber, *TEM turbulence optimisation in stellarators*, Plasma Physics and Controlled Fusion **58**, 014006 (2016).

The profile database used in this work is built upon work started by Gavin Weir. He started recording groups of shots for profiles during 2009-2014, and the format of the database entries is largely defined by that work. In the course of the research for this dissertation, changes were made to the formatting of the database to enable efficient analysis of a large number of profiles at once. In addition, the gradient scans in Chapter 2 required many more profiles to be added to the database. The vast majority of HSX data is only analyzed by the Run Coordinator of the experiment day, and the groups of reproducible shots are only sometimes recorded in the Run Log. Often, recording profiles required replaying the experiment day shot-by-shot. Future Run Coordinators are encouraged to record profiles immediately after an experiment day.

The HSX profile database and associated tools can be found on the shared network drive known as the "Y Drive" at Y_DRIVE/HSX_profile_database. This directory is version controlled with GIT. The database itself is the file profile_database.m, which is a MATLAB function. This function returns a structure array where each element represents a profile. The first field of the structure array is a runID, and the fields date and shots define the actual plasma discharges. The other fields contain various metadata related to that profile. The actual density and temperature profiles must be generated by calling db_TS_profiles. The file log_profile_database.m is a MATLAB "cell mode" or "code section" script containing examples of how to use the database and various helper functions. Profiles are added to profile_database.m by manually increasing the construction iterator and entering data to the structure fields. There is an opportunity to automate significant parts of this process in the future.